Federal University of Santa Catarina (UFSC)

Graduate Program in Materials Science and Engineering
(PGMAT)

Fabrication and characterization of porous ceramic filters with impregnated silver nanoparticles for water purification

Tatiane de Mattos Amadio

Scientific Advisors:

Prof. Dr. João Batista Rodrigues Neto/UFSC

Prof. Dr. Dachamir Hotza/UFSC

Prof. Michele Dondi/ISTEC

Florianópolis, December 2017.

Federal University of Santa Catarina (UFSC)

Graduate Program in Materials Science and Engineering
(PGMAT)

Fabrication and characterization of porous ceramic filters with impregnated silver nanoparticles for water purification

Thesis presented to the Graduate Program in Materials Science and Engineering, from the Technological Center of the Federal University of Santa Catarina, to obtain a PhD in Materials Science and Engineering.

Tatiane de Mattos Amadio

Florianópolis, December 2017.

Cataloguing data

AMADIO, Tatiane de Mattos, 1986-
Fabrication and characterization of porous ceramic filters with impregnated silver nanoparticles for water purification
Tatiane de Mattos Amadio – 2017.
185 p.
Advisors: João Batista Rodrigues Neto, Dachamir Hotza and Michele Dondi.
Thesis (PhD) – Graduate Program in Materials Science and Engineering, 2017.
1. Ceramic filters. 2. Pressing. 3. Freeze-casting. 4. Nanoparticles. 5. Silver.
I. Rodrigues Neto, João Batista, II. Federal University of Santa Catarina.
Postgraduate Program in Materials Science and Engineering.
III. PhD.

Fabrication and characterization of porous ceramic filters with impregnated silver nanoparticles for water purification

Tatiane de Mattos Amadio

This thesis was judged to obtain the PhD, and approved in its final form by the Postgraduate Program in Materials Science and Engineering.

_____

Prof. Dr. Guilherme Mariz de Oliveira Barra – PGMAT Coordinator

Prof. Dr. João Batista Rodrigues Neto Advisor (UFSC)	Prof. Dr. Dachamir Hotza Co-advisor (UFSC)

Examination Board:

Prof. Dr. Jorge Frade (University of Aveiro)	Prof. Dr. Murilo Innocentini (UNAERP)
Prof. Dr. Jeane do Rosário (UDESC)	

To God who gave me strength and always led me to the best way no matter the difficulties...

To my parents for support, patience, safe harbor, values and mainly for love in good and bad hours...

To my family who always believed in me...

To my boyfriend for understanding, love, support and strength...

To my friends for the dedication, company, friendship, attention and help, from far or near, always present...

To all who were present at this stage of my journey, each one contributing in a special way to make this achievement possible.

Acknowledgements

First and foremost, I want to thank God for allowing me to do this PhD with mental and physic health and with a lot of strength.

I want to thank my parents so much for giving me all the love, support, effort and patience, making me always trust in myself and never give up, always encouraging me.

I would like to thank Filipe Silva Vargas for giving me support and to stay always by my side understanding all the times I had to stay studying and working instead of making many other things.

This work was not easy to me and I had many barriers to overcome, but I always had my advisors to help and support me, so I would like to acknowledge Prof. Dr. João Batista Rodrigues Neto and Prof. Dr. Dachamir Hotza. It was an honor to work with you, thank you very much.

I would like to acknowledge the Conselho Nacional de Desenvolvimento Científico e Tecnológico (CNPq) for giving me all the financial support and grant of PhD scholarship.

I want to thank the Universidade Federal de Santa Catarina (UFSC) for making possible my PhD work and for giving me many wonderful experiences.

I would like to acknowledge the Graduate Program in Materials Science and Engineering (PGMAT) coordinators, professors and collaborators.

I want to thank CERMAT a lot, for giving me all the tools I needed and for being the best work environment of all, and the other laboratories at UFSC and outside that made my work possible, like Vitrocer, Lamate, Labmassa, Lapoa, LCP, Intelab, Nanotec-Lab.

I would like to acknowledge Prof. Dr. Murilo Innocentini of the Universidade de Ribeirão Preto (UNAERP), and his coworkers for performing the permeability analysis.

I want to thank Michele Dondi, Anna Costa and Magda Blosi for being my advisors in ISTEC-CNR during my period in Faenza, Italy. Thank Istituto di Scienza e Tecnologia

dei Materiali Ceramici (ISTEC-CNR) for giving me support to do my work and to give me friends of many parts of the world that made me feel at home even so far from there. It was an amazing life experience.

I would like to thank T-cota Eng. e Minerais Industriais for giving me the opportunity to make an internship there and learn many things during my PhD work.

I want to thank T-cota (bentonite), Laviosa (bentonite), Colorminas (kaolinite), Almatis (alumina) and TNS (silver nanoparticles) for providing the respective raw materials.

I would like to thank Rafael Matias Veit, which worked with me in his internship, for helping me during all the work, for his friendship and partnership.

My friends, mainly friends of CERMAT, were very important to me during all my Ph.D. period inside and outside the laboratory. I would like to thank all of them very much for help, friendship, support, partnership, meetings and every special moment I could stay with them.

Last but not least, I want to thank everyone that helped me directly or indirectly in my PhD, inside or outside the laboratory, everyone, every moment and every gesture was very important to me.

Thank you very much.

“There are only two days in the year that nothing can be done. One is called Yesterday and the other is called Tomorrow. Today is the right day to Love, Believe, Do and mostly Live.”

Dalai Lama

Abstract

The first part of this work aimed at characterizing bentonites of different features and origins (Brazil, Argentina, Italy and United States) that were submitted to functionalization with Ag, TiO_2, Pd and Au nanoparticles. Either commercial (TiO_2) or synthesized (Ag, Pd and Au) nanoparticles (NP) were used and characterized by DLS and XRD. Subsequently, the dispersed NP were impregnated on bentonite by two alternative methods, imbibition or dipping. The efficiency of impregnation of bentonite by metallic nanoparticles was tested by ICP-OES, which was over 90% in all cases. Particularly, Ag nanoparticles showed an impregnation efficiency above 99%, as confirmed by SEM-FEG. To improve impregnation, a thermal pretreatment for the bentonites was necessary at 700 °C. Both impregnation methods resulted in a suitable distribution and stability of Ag nanoparticles. The second part of this work aimed to obtain porous ceramic filters for water filtration with kaolinite and/or alumina, by pressing using rice husk like a sacrifice agent, and by freeze-casting with water. The powders were characterized by average particle size and distribution, zeta potential, XRD, XRF, density by picnometry, specific surface area (BET), and SEM. Parameters like viscosity, solidification rate, compression strength, porosity and permeability were analyzed. In the pressing method, samples with only kaolinite presented low porosity and low densification, while samples with only alumina have a high densification and very low porosity. The higher porosities occurred in samples with 35 to 60 wt% water and 20 to 30 wt% rice husk (<70 mesh). All the samples with kaolinite and alumina presented a good strength after contact with water, with flow rate less than 0.01 l/h. In the freeze-casting method, firstly two alumina powders (coarse and fine) were tested with mean particle sizes of 2.5 and 0.5 μm, respectively. As the particle size decreases, the solidification rate also decreases, so the solidification rate is higher for coarse alumina. At around 50 wt% solids, the porosity of coarse alumina is slightly higher than that of fine alumina,

around 73 and 68%, respectively. Permeability parameters k1 and k2 show that the pellets achieved the desired values for the application of ceramic filters for drinking water. Furthermore, coarse alumina was chosen and samples with alumina and kaolinite were produced and analyzed. Their filtration efficiency was evaluated using Colilert and Quanti-Tray/2000. Samples with coarse alumina and kaolinite reached best results of compression strength with the higher values of k_1 and k_2, with pores with sizes distributed homogeneously between 1.04 and 2.73 μm. The filtrated water presented a total number of coliforms and E. coli reaching less than a half of the minimum value allowed for animal consumption and less than one eighth of the value allowed for recreation, with a turbidity around 0.56 NTU. The final filter pellets were impregnated with silver nanoparticles and the efficiency of impregnation and bactericidal effects were tested. Silver nanoparticles were characterized by average particle size, zeta potential and TEM. After impregnation, the leached water was analyzed by GFAAS that shows an efficiency of more than 99% in silver impregnation. From SEM/EDS, it was possible to observe that the pellets have a homogeneous distribution of silver nanoparticles. A halo of inhibition detected by the disc diffusion test shows a strong bactericidal effect of the filters.

Keywords: Ceramic filters, pressing, freeze casting, nanoparticles, silver.

Resumo

A primeira parte deste trabalho teve como objetivo caracterizar bentonitas de diferentes propriedades e origens (Brasil, Argentina, Itália e Estados Unidos), que foram submetidas à funcionalização com nanopartículas de Ag, TiO_2, Pd e Au. Nanopartículas comerciais (TiO_2) e sintetizadas (Ag, Pd e Au) (NP) foram utilizadas e caracterizadas por DLS e DRX. Posteriormente, as NP dispersas foram impregnadas em bentonitas por dois métodos alternativos, imbibição ou imersão. A eficiência da impregnação das bentonitas por nanopartículas metálicas foi testada por ICP-OES, cujo resultado foi de mais de 90% em todos os casos. Particularmente, as nanopartículas de Ag mostraram uma eficiência de impregnação superior a 99%, conforme confirmado por MEV-FEG. Para melhorar a impregnação, foi necessário um pré-tratamento térmico para as bentonitas a 700 °C. Ambos os métodos de impregnação resultaram em uma distribuição e estabilidade adequadas das nanopartículas de Ag. A segunda parte deste trabalho teve como objetivo obter filtros cerâmicos porosos para filtração de água, utilizando caulinita e/ou alumina, através de prensagen, com o uso de casca de arroz como agente de sacrifício e freeze-casting, utilizando água. Os pós foram caracterizados por distribuição e tamanho médio de partículas, potencial zeta, DRX, FRX, densidade por picnometria, área de superfície específica (BET) e MEV. Foram analisados parâmetros como viscosidade, taxa de solidificação, resistência à compressão, porosidade e permeabilidade. No método de prensagem, amostras com apenas caulinita apresentaram baixa porosidade e baixa densificação, enquanto as amostras com apenas alumina possuem alta densidade e muito baixa porosidade. As porosidades mais altas ocorreram em amostras com 35 a 60% em peso de água e 20 a 30% em peso de casca de arroz (<70 mesh). Todas as amostras com caulinita e alumina apresentaram boa resistência mecânica após contato com água, com taxa de fluxo inferior a 0,01 l/h. No método de freeze-casting, primeiramente, dois pós de alumina, com

tamanhos médios de partículas de 2,5 e 0,5 μm, respectivamente, foram testados. À medida que o tamanho de partícula diminui, a taxa de solidificação também diminui, de modo que a taxa de solidificação é maior para alumina de 2,5 μm. Em cerca de 50% em peso de sólidos, a porosidade dessa alumina é ligeiramente superior à da alumina mais fina, aproximadamente 73 e 68%, respectivamente. Os parâmetros de permeabilidade k1 e k2 mostram que as pastilhas atingiram os valores desejados para a aplicação de filtros de cerâmica para água potável. Além disso, a alumina com 2,5 μm foi escolhida, e amostras com alumina e caulinita foram produzidas e analisadas. Sua eficiência de filtração foi avaliada usando Colilert e Quanti-Tray/2000. As amostras com alumina e caulinita atingiram os melhores resultados de resistência à compressão com valores maiores de k1 e k2, com poros de tamanhos entre 1,04 e 2,73 μm, distribuídos de forma homogênea. A água filtrada apresentou um número total de coliformes e E. coli que atingiu menos da metade do valor mínimo permitido para consumo animal e menos de um oitavo do valor permitido para recreação, com uma turbidez de cerca de 0,56 NTU. As pastilhas de filtro finais foram impregnadas com nanopartículas de prata e a eficiência de impregnação e efeitos bactericidas foram testados. As nanopartículas de prata foram caracterizadas pelo tamanho médio de partícula, potencial zeta e MET. Após a impregnação, a água lixiviada foi analisada por GFAAS que mostra uma eficiência superior a 99% na impregnação de prata. A partir de MEV/EDS, foi possível observar que as pastilhas têm uma distribuição homogênea de nanopartículas de prata. Um halo de inibição detectado pelo teste de difusão de disco mostra um forte efeito bactericida dos filtros.

Palavras-chave: Filtros cerâmicos, prensagem, freeze-casting, nanopartículas, prata.

List of Figures

List of Tables

Table of Contents

1 Introduction

The treatment of water is always a subject of interest due to the immense importance in human health. According to the World Health Organization (WHO), 80% of the diseases existent are caused by the intake of contaminated water. The risk of microbiological contamination of water for human consumption is the subject of many studies. The origin of contamination is related to water collection, transfer and/or storage (Clasen and Bastable, 2003; Lv et al., 2009; Simonis and Basson, 2011; WHO, 2006).

One of the most efficient technologies, for water purification, is the use of ceramic filters. In this work, two raw materials, alumina and/or kaolinite, and two shaping techniques, respectively, pressing (with or without porogenic agents) or freeze casting were considered for manufacturing ceramic filters. Pressing was chosen due to simplicity, low cost, velocity and low energy, and freeze casting was selected because it is a versatile fabrication technique of porous structures, and generally offers a wider range of pore characteristics.

Freezing casting has aroused great interest in the industry, due to its peculiar properties that it generates. In this technique, many factors influence the microstructure and properties of porous ceramics, like porosity and mechanical strength, such as composition and initial solids loading, cooling rate, sintering temperature, and additive content (Deville, 2008; Hu et al., 2010; Liu and Button, 2013). The particle size of the powders has an important effect on the final sample properties, but it has attracted little attention. Thus, in this work, two alumina powders, with particle size 2.5 and 0.5 μm respectively, were tested to observe the influence of the particle size on freeze-cast porous bodies.

To increase the efficiency in the water filtration, an innovative approach for impregnation of porous ceramic pellets was tested with silver nanoparticles in order to optimize reactive surface area and to enhance bactericidal effects. Silver is often used as an antibacterial agent, in order to provide a sanitary environment for wound healing. The multiplicity of silver's bactericidal mechanisms gives it a wide range of effective applications in the inhibition of bacterial growth. (Alexander, 2009; Nam et al., 2015; Bal et al., 2015; Dong et al., 2016; Mckevica et al., 2016; Amadio et al., 2017).

2 Aims

2.1 General aim

This work is aimed to obtain porous ceramic bodies with clay minerals and/or alumina, to reach a suitable porosity and permeability with an acceptable compression strength, and impregnate them efficiently with silver nanoparticles for bactericidal effect.

2.2 Specific aims

The specific aims follow:

- To functionalize bentonites with Ag, TiO_2, Pd and Au nanoparticles by two alternative methods, imbibition or dipping;
- To manufacture pressed filters with kaolinite and/or alumina, with and without rice husks and water, with different process parameters;
- To manufacture freeze-cast filters, optimizing all the compositions and parameters;
- To evaluate the effect of particle size of alumina on process and product related to freeze casting;
- To test the freeze-cast filter efficiency and the characteristics of the filtrated water;
- To test the efficiency of silver-nanoparticle impregnated filters in terms of their bactericidal effect.

3 Literature review

3.1 Water treatment

The access to clean and safe water is of paramount importance for human health. It is estimated that in the 21st century more than one billion people will not have access to safe drinking water. Much of this population is concentrated in underdeveloped countries, especially in rural areas. Small communities have the most difficulty in receiving water in sufficient quantity and quality, the lack of maintenance and expansion of reservoirs coupled with the lack of supply and non-compliance with standards that define the water quality standard are some of the reasons why the population is exposed to diseases transmitted through the water (Mwabi et al., 2011).

It is estimated that 4% of all deaths worldwide results from diarrhea caused by pathogenic bacteria present in waters considered unfit for human consumption. In South Africa, for example, diarrhea is responsible for 11% of the deaths of children under 5 years of age, in developing countries this number is even more significant increasing to 21%. According to the World Health Organization (WHO), 80% of the diseases existents are caused by the intake of contaminated water, the recommendation is that the water for human consumption contains a quantity of total coliforms corresponding to 0 in a 100 ml sample. The risk of microbiological contamination of water for human consumption is the subject of many studies. There is constant contamination during water collection, transfer and storage (Clasen and Bastable, 2003; Lv et al., 2009; Simonis and Basson, 2011; WHO, 2006).

There are many technologies for home water treatment and some of them are the subject of research in laboratories to evaluate the effectiveness in reducing pathogens and diseases such as diarrhea. One of the most efficient technologies is the manufacture of ceramic filters, which act efficiently as a barrier against pathogenic organisms. Disk filters produced by the organization Potters for Peace achieved expressive results as the reduction of 97.8% of Escherichia coli (Brown and Sobsey, 2010).

Studies with 37 different water treatments indicate that ceramic water filters are among the five most effective treatments for turbidity reduction and a 99% reduction of bacteria in the laboratory, but this value becomes lower in field conditions. In developing countries household-scale ceramic filters are being used as a better treatment option for both unpurified and insufficiently disinfected water in households (Lantagne, 2001; Clasen and Boisson, 2006; Simonis and Basson, 2011).

In a report of the WHO Commission on Health and Environment (undated), three mechanisms of transmittal for waterborne diseases are described (Lantagne, 2001):

- Waterborne diseases

These arise from the contamination of water by human or animal feces or urine infected by pathogenic viruses or bacteria, which are directly transmitted when the water is drunk or used in the preparation of food.

- Water-washed diseases

Scarcity and inaccessibility of water make washing and personal cleanliness difficult and infrequent. Where this is so some diarrheal diseases and contagious skin and eye infections are prevalent. All waterborne diseases can also be

water-washed diseases. Water-washed diseases diminish whenever an adequate supply of water is available and used.

- Water-based diseases

Water provides the habitat for intermediate host organisms in which some parasites pass part of their life cycle.

In addition, the WHO detailed the public health impact worldwide of waterborne diseases (Table 1). A number of diseases have not yet had morbidity, mortality, and population at risk statistics developed, however, the statistics that have been enumerated show that a significant fraction of the world population is both at risk for, and contracts, waterborne diseases (Lantagne, 2001).

Table 1. Worldwide public health impact of waterborne disease (WHO, undated; Lantagne, 2001).

Disease	Morbidity (per year)	Mortality (deaths / year)	Population at risk
Waterborne & water-washed			
Cholera			
Diarrheal disease	1,500 million episodes in children under 5	4 million in children under 5	Over 2,000 million
Enteric fevers	500,000 cases	25,000	
Poliomyelitis	204,000	25,000	
Ascariasis (roundworm)	1,000,000	20,000	
Leptospirosis			
Trichuriasis			
Water-washed			
Trachoma	6 – 9 million blind		500 million
Leishmaniasis	400,000 new infections / year		350 million
Relapsing fever			
Typhus fever			
Water-based			
Schistosomiasis	200 million	200,000	500 – 600 million
Dracunculiasis	Over 10 million		Over 100 million

Thus, a number of different organisms of varying size and pathology contribute to waterborne disease throughout the world. Two mechanisms in the Potters for Peace (PFP) filter contribute to reduction of these organisms (Lantagne, 2001):

- The first mechanism is filtration. The PFP filter will trap any particle or organism that is larger than the pore size of the filter. The pore size in the filter ranges are from 0.6 to 3.0 μm, PFP aims to have a pore size of 1 μm to remove E. coli without the need for a disinfectant. This would trap a significant portion of bacteria, and all protozoa and helminthes. However, viruses are smaller than 1 μm, and thus would not be trapped. The variation in pore size is due to the location of sawdust during burning. If the pore size is maintained at a maximum of three microns, it is expected that the PFP filter will remove a significant percentage of these protozoa (Lantagne, 2001).
- The second mechanism is inactivation, in which colloidal silver is used in the PFP filter against organisms contributing to waterborne disease (Lantagne, 2001).

3.2 Ceramic filters

In recent years, ceramic filters have been widely used for microbiological treatment of water due to its low cost. Porous ceramics are manufactured from refractory oxides such as alumina, titania, zirconia. Briefly, the advantages of porous ceramics over other filtration techniques and materials are their chemical, thermal and pH stability, allied to the previous features there is also the longevity and strength to pressure, temperature and corrosion, bringing an excellent cost benefit (Lv et al, 2009; Bielefeldt et al, 2009).

Ceramic water filters (CWFs) are manufactured, for example, by mixing clay with a pore forming agent such as sawdust or rice husk and a liquid, usually water. The filters

are molded in mechanical hydraulic presses or through the potter's wheel, then they pass into the sintering process, where the pore forming agent is eliminated as gas, leaving in the structure small interconnected pores (Yakub and Soboyejo, 2012).

Two primary mechanisms, physical removal and inactivation, are considered important in the microorganism disinfection by CWFs. First, in physical removal mechanism, filtration by size exclusion removes larger microorganisms such as protozoans and some bacteria and may be attributed to the initial filter pore sizes, as well as the solids filter cake that accumulates inside the filter. Surface association and the subsequent filter cake may also remove smaller bacteria and viruses (Bielefeldt et al, 2009).

In the physical removal filtering mechanism, properties such as geometry and pore surface are of fundamental importance for the efficiency in the removal of microorganisms to levels indicated by the WHO. Porosity is the most used property to describe the pores of a material, being defined as a fraction of the total volume occupied by pores. (Yakub and Soboyejo, 2012; WHO, 2014; Youmoue et al., 2017).

Additionally, in inactivation mechanism, ionic and nanoscale silver has been shown to inactivate pathogens, including bacteria and to a lesser extent viruses. The silver may inactivate pathogens that pass through the filter pores, may limit bacterial growth in the filter itself (bacteriostatic), or exert other effects of benefit to disinfection. Several studies have quantified the CWF removal of bacteria, such as fecal coliform or Escherichia coli, which serve as indicators of pathogenic microorganism disinfection. Laboratory studies have reported high pathogen disinfection efficiency for the new filters, with fresh silver coating (Brady et al., 2003; Cho et al., 2005; Huang et al., 2008; Zeng et al., 2007; Bielefeldt et al, 2009).

The ceramic matrix composition is fundamental in the resulting porosity of the material, since filters constructed with particle sizes ranging from 0.02 to 4 μm can result in 34 to 46% porosity. Pore size and geometry have great influence on porosity, interconnected pores with a size of 3 to 4 μm tend to maximize hydraulic conductivity (Simonis and Basson et al., 2012; Youmoue et al., 2017).

According to Yakub et al., the porosity of the filters increases with the increase in the percentage of organic material in the composition. In contrast, the mechanical strength to compression and bending decreases with increasing porosity; with the porosity increasing from 36 to 46%, the compression strength decreases respectively from approximately 9 to 5 MPa. This decrease in compression strength value is due to the increase in sawdust content of 25-50% in volume (Yakub and Soboyejo, 2012).

Figure 1 illustrates low cost options that are being practiced in developing countries, namely the pot and disk filter elements respectively used by Potters for Peace and Filtron systems (Simonis and Basson, 2011).

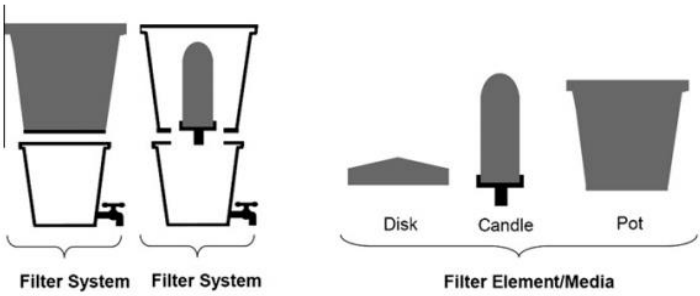

Figure 1. Filter elements and filter system (Simonis and Basson, 2011).

Porous ceramics are widely used in various versatile applications, such as liquid gas filters, catalysis supports, gas distributors, insulators, preforms for metal-impregnated ceramic metal composites, and implantable bone scaffolds (Scheffler and Colombo, 2005; Studart et al., 2006).

Porous ceramics are advantageous in such application areas due to their high melting point, tailored electronic properties, and high corrosion and wear strength, which combine favorably with the features gained by the introduction of voids into the solid material (Kingery et al., 1975; Princen and Kiss, 1989; Colombo and Hellmann, 2002; Guzman, 2003).

These features include low thermal conductivity, controlled permeability, high surface area, low density, high specific strength, and low dielectric constant. These properties can be tailored for each specific application by controlling the composition and microstructure of the porous ceramic. Changes in open and closed porosity, pores size distribution, and pores morphology can greatly affect materials properties. These microstructural features are highly influenced by the processing route used to produce the porous material (Binks, 2002; Colombo, 2006; Murray, 2007; Horozov, 2008; Neirinck et al., 2009).

3.2.1 Methods to obtain porous ceramics

Several processing routes using replica, sacrificial template, or direct foaming methods are nowadays available for the production of macroporous ceramics. The techniques differ greatly in terms of processing features and final microstructures/properties achieved (Studart et al., 2006). Figure 2 shows the scheme of possible processing routes used for the production of macroporous ceramics.

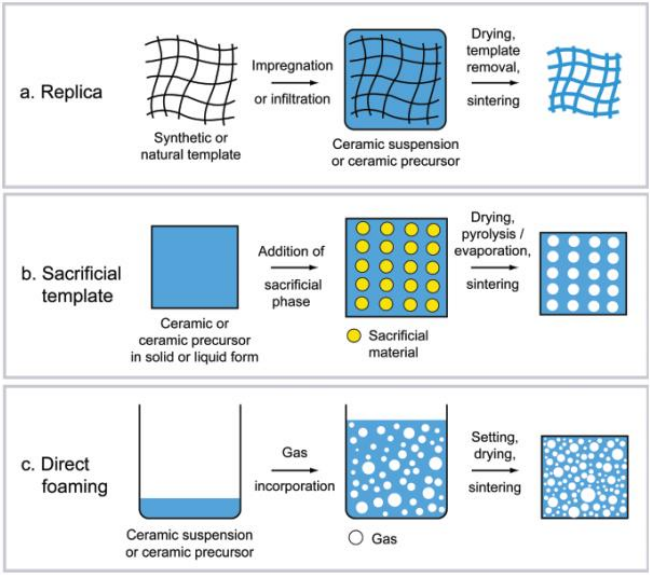

Figure 2. Processing routes used for the production of macroporous ceramics (Studart et al., 2006).

3.2.1.1 Replica

The replica method is based on the impregnation of a cellular structure with a ceramic suspension or precursor solution in order to produce a macroporous ceramic exhibiting the same morphology as the original porous material (Figure 2a). This is followed by the removal of excess slurry, pyrolysis of the polymeric substrate, and sintering to solidify the foam. Many synthetic and natural cellular structures can be used as templates to fabricate macroporous ceramics through the replica technique (Binks, 2002; Studart et al., 2006).

Binders and plasticizers are also added to the initial suspension to provide ceramic coatings sufficiently strong to prevent the struts from cracking during pyrolysis. This process is explored fully elsewhere. The resulting ceramic is formed

after removal of the polymeric template (Binks, 2002; Colombo, 2006, Studart et al., 2006).

The disadvantages of this technique are in the formation of the struts of the reticulated structure during pyrolysis of the polymeric template, which significantly weakens the mechanical strength of the resulting porous ceramic (Subramaniam, et al., 2006).

The polymer replica technique is an easy and well-established method to prepare open cellular structures with pore sizes ranging from 200 μm to 3 mm at porosity levels between 40 and 95%. A replica approach that uses wood structures as positive templates was developed in recent years. Highly oriented open pores ranging from 10 to 300 μm can be produced with this method at porosities between 25 and 95% (Studart et al., 2006).

3.2.1.2. Sacrifical template

The sacrificial template method is flexible and can employ various chemical compositions. Various oxides have been used to fabricate porous ceramics using starch particles as sacrificial templates. The sacrificial template technique usually consists of the preparation of a biphasic composite comprising a continuous matrix of ceramic particles or ceramic precursors and a dispersed sacrificial phase that is initially homogeneously distributed throughout the matrix and is ultimately extracted to generate pores within the microstructure (Figure 2b). This method leads to porous materials displaying a negative replica of the original sacrificial template, as opposed to the positive morphology obtained from the replica technique described by Studart et al. (2006).

One of the main advantages of the sacrificial template method in comparison with the other fabrication routes is the possibility to deliberately tailor the porosity, pore size

distribution, and pore morphology of the final ceramic component through the appropriate choice of the sacrificial material. Figure 3 shows that the range of porosity and pore sizes that can be achieved with this technique is very broad (20–90% and 1–700 μm, respectively), as they only depend on the volume fraction and size of the sacrificial template used (Studart et al., 2006).

The method of the sacrificial materials extraction from the consolidated composite depends primarily on the type of pore former employed. Predominantly open pores of various different morphologies can be produced with this method. The most crucial step in this technique is the removal of the sacrificial phase by pyrolysis, evaporation, or sublimation. These processes might involve the release of an excessive amount of gases and have to be carried out at sufficiently slow rates in order to avoid cracking of the cellular structure. The slow removal of the sacrificial phase may considerably increase the processing time in the case of large components. The mechanical strength of cellular structures produced with this method is often substantially higher than that achieved with the positive replica techniques (Aranberri et al., 2009; Studart et al., 2006).

3.2.1.3. Direct foaming

Porous ceramics properties are also highly influenced by their chemical compositions and microstructures, with porosity, pore morphology, and size distribution being tailored by different compositions, different physical structures of the starting materials, and the use of different amphiphiles (Aranberri et al., 2009; Pokhrel et al., 2011; Sarkar et al., 2015).

In direct foaming methods, porous materials are produced by incorporating air into a suspension or liquid media, which is subsequently set in order to keep the structure of air bubbles created (Figure 2c). In most cases, the

consolidated foams are after wards sintered at high temperatures to obtain high-strength porous ceramics. The total porosity of directly foamed ceramics is proportional to the amount of gas incorporated into the suspension or liquid medium during the foaming process. The pore size, on the other hand, is determined by the stability of the wet foam before setting takes place (Studart et al., 2006).

Direct foaming methods offer an easy, cheap, and fast way to prepare macroporous ceramics with open or closed porosities from 40 to 97%. The pores produced with this approach result from the direct incorporation of air bubbles into a ceramic suspension, eliminating the need for extensive pyrolysis steps before sintering. The stabilization and setting of the wet foams is the decisive step in direct foaming methods. Foams stabilized with surfactants lead to porous ceramics exhibiting average pore sizes from 35 µm to 1.2 mm (Studart et al., 2006).

The high stability of the wet foams allows their direct drying in ambient air at room temperature. However, in order to avoid cracking, the wet foams must be slightly strengthened to overcome the capillary stresses and to avoid differential shrinkage within the drying foam (Pokhrel et al., 2011).

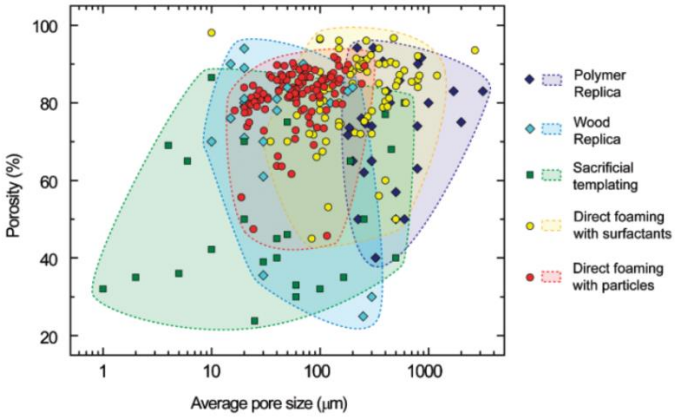

Figure 3. Typical porosity and average pore size achieved via the replica, sacrificial templating, and direct foaming processing routes (Studart et al., 2006).

3.2.1.4 Freeze -casting

Interest in the effect of freezing on solutions and suspensions dates back at least to the beginning of the 20th century, when first qualitative observations were reported by, for example, Bobertag et al. (1908) and Lottermoser (1908). Lottermoser was probably among the first who described the formation of materials with honeycomb structures upon freezing. Bobertag et al. noted structural changes in the first frozen, then remelted material, which are due to the expanding ice crystals exerting forces on the matter, which, upon freezing, is expelled from the liquid carrier and trapped between the crystals. About 50 years later, Maxwell et al**.** (1954) described freeze casting as we understand it today. They reported the successful preparation of intricately shaped objects such as turbocharger blades from an extremely thick ceramic slip by casting, freezing and liquid sublimation before sintering (Wegst et al., 2010).

The growing interest for the development of ceramic parts with hierarchical porosity exhibiting high mechanical

properties led the scientific community to focus on alternative shaping techniques to substitute the conventional foaming technique and the use of pore former precursors. Indeed, they are quite simple to implement but the organization of the resulting porosity remains random in most of the cases (Sepulveda, 1997; Studart et al., 2006). Even if new mathematical models for their presentation of the tortuosity have been recently given, it remains very difficult to model such random microstructures.

Among the emerging techniques, freeze casting is an attractive shaping method for the fabrication of highly porous and hierarchically organized ceramic structures. It consists of freezing generally by the bottom a ceramic slurry followed by the sublimation of the solvent by freeze drying at both low pressure and temperature (Zhang et al., 2015; Gaudillere and Serra, 2016).

Porous ceramics have a wide number of applications as catalyst carrier, ceramic filter, sensor, porous electrode, biomaterials, thermal barrier, among others. Freeze casting has many advantages, including small processing shrinkage, controllable and wide porosity range, and relatively high strength. Fukasawa et al. (2001; 2002) applied freeze casting to fabricate porous alumina and silicon nitride ceramics with unidirectionally aligned pore channels. Their work revealed the potentiality for fabricating porous ceramics, and a great deal of efforts has been subsequently put into practice (Deville, 2008; Hu et al., 2010).

Freeze-casting has first been developed as a near net shape forming technique, yielding dense ceramics parts with fine replicate of the mold details. Any ice crystal being converted into porosity later on in the process, introducing large size defects were largely unwelcome in ceramic applications. A great deal of efforts has been put in controlling or avoiding the formation of ice crystals. Only later on was it realized that the formation and growth of ice crystals could be

a substantial benefit if properly controlled, yielding porous ceramics with a very specific porosity (Lu et al., 1998; Sofie and Dogan, 2001; Deville, 2008).

Thus, freeze casting has received broad attention as a simple and versatile fabrication technique of porous structures, and generally offers a wider range of pore characteristics compared to other conventional fabrication methods such as foam or wood replication, direct foaming, and gel casting. Water and camphene are the most common solvents in freeze casting process (Deville et al., 2007; Fukushima et al., 2008; Yoon et al., 2008; Li and Li, 2012).

The freeze casting of ceramic parts has the potential of being a simpler approach to produce complex-shaped ceramic parts. Freeze casting involves the preparation of a ceramic slip that is poured into a mold, then frozen and subjected to sublimative drying of the solvent under vacuum. Given the inherent strength of frozen solvents, this method allows them to temporarily act as a binder to hold the part together after demolding. This, therefore, minimizes the additive concentration for enhanced solid purity and faster binder burnout cycles. Removal of the solvent by sublimation also eliminates drying stresses and shrinkage that may lead to cracks and warping during the normal drying of a solvent-saturated body (Sofie and Dogan, 2001).

The freezing of the ceramic slurry induces the growing of vertical solvent crystals along the freezing direction and the associated ceramic particles are entrapped between these crystals (Figure 4). Finally, the as-obtained green body after solvent removal by freeze-drying is sintered for consolidation and the final freeze-cast sample exhibits hierarchically and vertically aligned porosity, which is the replica of the original solvent crystals (Gaudillere and Serra, 2016).

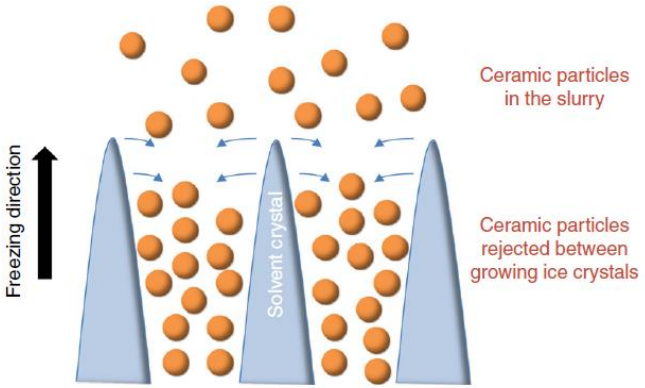

Figure 4. Sketch of the growing of ice crystals during the freezing step and the associated distribution of ceramic particles between the ice crystals (Gaudillere and Serra, 2016).

The control of pore structure is performed through composition and solid loading of slurry, as well as sintering conditions, which influence the microstructure and properties of porous ceramics fabricated by freeze casting (Hu et al., 2010).

Figure 5 shows the schematic representation of a freeze casting system and pore structure formation during freeze casting (Hu et al., 2010).

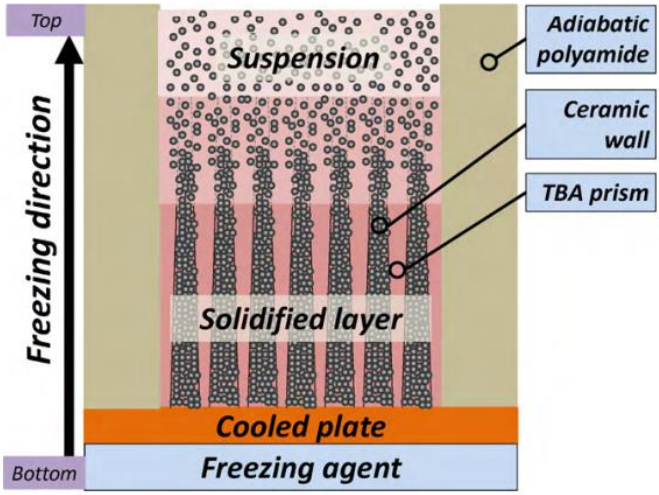

Figure 5. Schematic illustration of freeze casting system and pore structure formation during freeze casting (Hu et al., 2010).

According to Deville, the process can be divided into four steps (Figure 8), and the corresponding experimental conditions will strongly depend on the chosen solvent.

a) Preparation of the slurry

The ceramic powder must be correctly dispersed in the liquid medium (the solvent), so that dispersant and plasticizer are often used. The temperature of the slurry must fall in the range where the solvent is liquid, room temperature in the case of water, but different temperatures (60 °C and 8 °C) are necessary for respectively camphene-based and tert-butyl alcohol slurries. Moderate solid loading is used (10–40 vol%), depending of the desired amount of total porosity. The stability of the suspension must be carefully controlled to avoid any segregation taking place in the second stage, yielding gradients of density and porosity in the final materials. This can be particularly problematic for low solid

loadings. Finally, the presence of a binder is necessary, to provide green strength after sublimation. Though the solvent is playing the role of the structuring agent, binder and pore forming agent, it is nevertheless removed during the sublimation stage, so that green bodies collapse in absence of an organic binder (Deville, 2008).

Ceramic slurries for freeze casting are typically composed of micro or nanometric particles suspended in water to which dispersants (e.g. polyacrylates) and binders (e.g. polyvinyl alcohol) are commonly added. Dispersants, which can be anionic, cationic or neutral and which depend on the liquid carrier and particles suspended in it, reduce particle aggregation and flocculation. Both are undesirable because they lead to heterogeneities in the final product and they change the slurry's physical properties such as its sedimentation behavior and viscosity (Fu et al., 2008; Wegst et al., 2010).

For a given particle size, the viscosity depends on the type of interaction between particles and liquid carrier, whether by van der Waals forces, hydrogen bonds or polar interactions. For a given type of interaction, the viscosity depends on the particle size. In the case of van der Waals forces, for example, the forces grow with molecular weight and particle size; the higher the molecular weight or the larger the agglomerate, the higher the forces and the higher the viscosity. For a given particle size, an increase in solid-volume fraction has the same effect, because the particles are more closely packed, resulting in more and stronger particle–particle interactions increasing the strength to flow. The viscosity of the slurry is a particularly important processing parameter in freeze-casting. It determines, for a given particle size, both the velocity of sedimentation and the critical freezing-front velocity at which particle trapping occurs during solidification. Viscosity is thus a structural parameter that determines the material's structural and mechanical properties (Wegst et al., 2010).

b) Controlled Solidification of the Slurry

This is the critical stage where the structure is formed and the characteristics of the future porosity are determined. During this stage, continuous crystals of solvent are formed, under certain conditions, and grow into the slurry. Ceramic particles in suspension in the slurry are rejected by the moving solidification front, concentrated and entrapped in-between the crystals. To induce this natural segregation phenomenon, the slurry is poured in a mold, which undergoes isotropic or anisotropic cooling to induce homogeneous or directional solidification. The solidification conditions are dictated by the initial choice of the solvent. Low temperatures (< 0 °C) are required when using water, while room temperature are sufficient when using camphene, its solidification point being around 44–48 °C (Deville, 2008).

c) Sublimation of the Solvent

Once complete solidification of the sample is achieved, the sample is kept at conditions of low temperature and reduced pressure, conditions dictated by the physical properties of the solvent. Under these sublimation conditions, the solidified solvent is converted into the gas state. Porosity is created where the solvent crystals were, so that a green porous structure is obtained; the porosity is a direct replica of the solidified solvent structure. When using water, a conventional freeze-dryer can be used. In the case of camphene, the vapor pressure of 1.3 kPa (just below the melting temperature) is high enough to allow sublimation at room temperature, so that no specific equipment is required (Deville, 2008).

Figure 6 shows three first steps of freeze-casting process in a graphic with pressure (atm) versus temperature (°C), where in point A, there is a ceramic slurry (liquid state), in point B, the temperature decreases until having ice crystals and ceramic particles (solid state), staying in -70 °C (ultra-freezer temperature) and pressure 1 atm, after that, the solid

sample were taken to the freeze-dryer to do the lyophilization, point C, with -50 °C and 0.39 atm until the water, before ice crystals, go out of the structure (gas state), the final structure has the pores and the ceramic particles, point D.

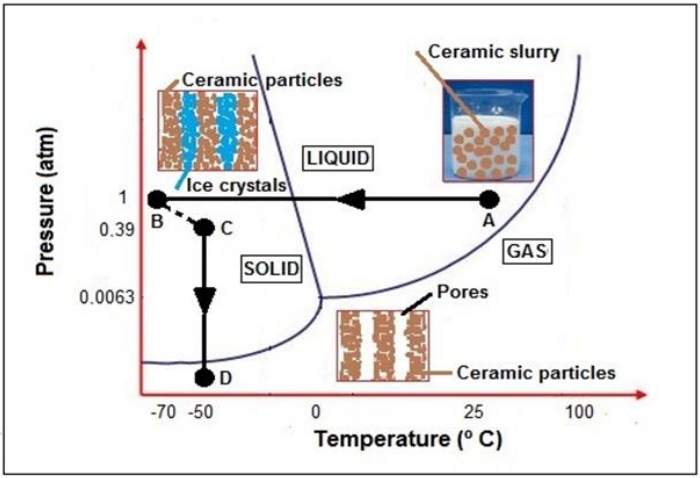

Figure 6. Steps of freeze-casting process, A) ceramic slurry (liquid state); B) ice crystals and ceramic particles (solid state); C) Low temperature and pressure until the water, before ice crystals, go out of the structure (gas state); D) final structure with pores and the ceramic particles (Source: Author).

d) Sintering or Densification of the Green Body

Once the solvent has been totally removed, the obtained green body can be sintered with conventional sintering technique. The low strength of the green body prevents any use of pressure assisted sintering (Deville, 2008).

The porosity of the sintered materials is a replica of the original solvent crystals. A variety of pores morphology can be obtained, depending on the choice of the solvent,

slurries formulation and the solidification conditions (Figure 7). Since the solidification is often directional, the porous channels run from the bottom to the top of the samples. Homogeneous freezing (i.e., cooling at constant rate starting from room temperature) results in a more homogeneous ice nucleation leading to a lamellar porous architecture (Figure 7B), with long-range order, both in the parallel and perpendicular directions of the ice front. After sintering, the ceramics walls can be completely dense with no residual porosity, depending on the sintering conditions. In the particular case of water being used as a solvent, the microstructure is lamellar, with lamellar channels between the ceramics walls (Araki and Halloran, 2004; Araki and Halloran, 2005; Deville et al., 2007; Yoon et al, 2007; Deville, 2008).

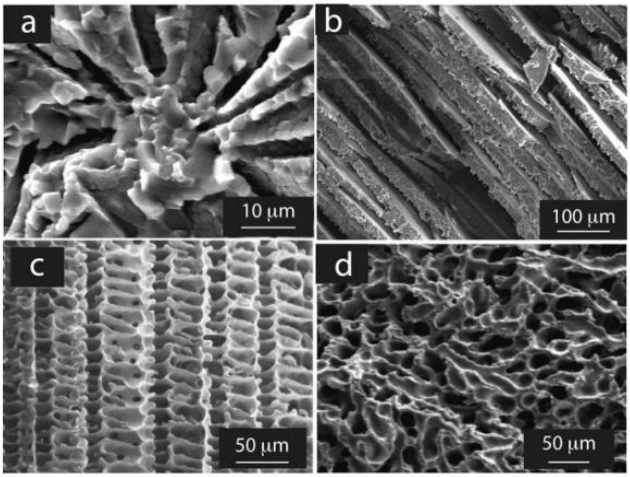

Figure 7. Typical microstructures obtained by freeze-casting (a) porous alumina using an hypoeutectic camphor/naphthalene as a solvent (b) porous alumina using water as a solvent (c) porous silicon carbide using polycarbosilane as a precursor and camphene as a solvent and (d) porous alumina using camphene as a solvent (Deville, 2008).

e) Orientation of Macroporosity

The pore channels can be oriented, depending on the solidification conditions. In most of the cases, the mold in which the slurry is initially poured is left with its bottom in part in contact with a cold surface. The solvent crystals are therefore solicited to grow vertically, along the direction of the imposed thermal gradient. However, different thermal gradients can be imposed, to induce a different anisotropy in the structure. many factors affecting the porosity and mechanical properties of the final porous ceramic, such as initial solids loading, cooling rate, sintering temperature, and additive content (Deville, 2008; Liu and Button, 2013).

3.2.2 Raw materials for porous ceramics

3.2.2.1 Clay minerals

Bentonite is a plastic and colloidal clay consisting essentially of montmorillonite and other minerals of the smectite group, with other components such as kaolinite, ilite, feldspars, amphiboles, cristobalite and quartz. The total non-clay content of the bentonite is hardly less than 10%. Such components present varying colors, such as: white, gray, yellow, brown, green and blue (Grim, 1968).

Smectite is the term given to a group of minerals consisting of: montmorillonite, beidelite, nontronite, hectorite and saponite. Each mineral forms a similar structure, though chemically different. Nontronite, for example, is an iron-rich smectite and hectorite is rich in lithium. The most common mineral in the economical deposits of the smectite group is montmorillonite, which is the predominant mineral in the composition of bentonites. In industry, montmorillonites are generally classified as sodium (Na) or calcium (Ca), depending on the predominant exchangeable ion (Hassan and Abdel-Khalek, 1998; Paiva et al., 2008).

The smectites are hydrated aluminosilicates of aluminum, iron and magnesium, in proportions 2:1 (two tetrahedron silica-oxygen layers, and the octahedral layer of metal-oxygen between them) (Holtzer et al., 2011).

The general chemical formula of montmorillonite is $M_x(Al_{4-x}Mg_x)Si_8O_{20}$- $(OH)_4$, where M^{+1} is a monovalent cation. It has particles of sizes that can vary from 0.1 to 2 μm, and format of plates or blades (Silva; Ferreira, 2008). Figure 8 shows the structure of two lamellae of montmorillonite.

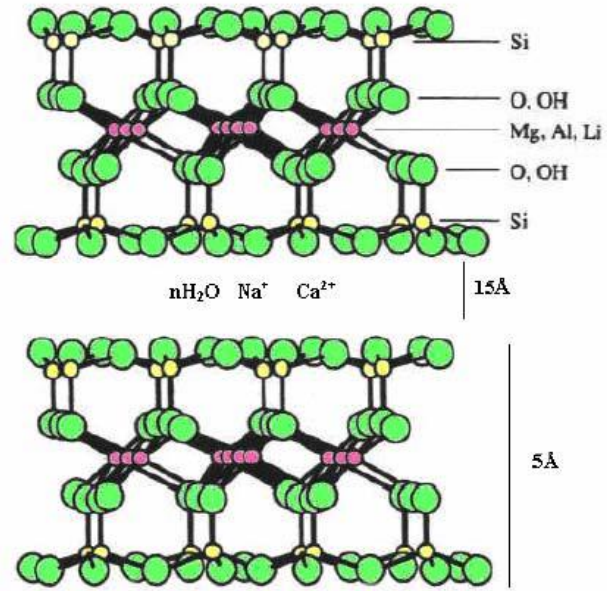

Figure 8. Structure of two lamellae of montmorillonite (Arshak et al., 2004).

The term bentonite, according to the literature, was first applied to a type of plastic and colloidal clay from a rock discovered at Fort Benton, Wyoming, USA. Although originally the term bentonite referred to the discovered clay

rock, at the moment it designates clay constituted, mainly, of the clay mineral montmorillonite. This term is also used to denote a product with high smectite content (Luz; Lins, 2008).

As a geological and petrographic term, bentonite is a rock formed from volcanic ash altered and largely composed of montmorillonite of the smectite type. It has great ability to absorb water and swell (Bulut et al., 2009).

Bentonites belong to an important type of clays widely used in many sectors of industry, such as drilling of oil wells and water collection, various foundries, pelletizing of iron ore, chemical and pharmaceutical industries (Amorim et al., 2006).

Bentonites are mostly calcic or sodic, and sodic expand many times their volumes when in contact with water, forming thixotropic gels. Some cations cause an expansion so intense that the layers of crystals can be separated up to their unit cell. Sodium causes the most notable expansion. The calcic and sodic varieties, based on exchangeable cation, are the most abundant bentonites. If the cation is Na+, the swelling may progress from 12.5 Å, when the clay is exposed to air, to a maximum of 40.0 Å, when the clay is fully dispersed in a liquid medium (Lummus and Azar, 1986).

The sodic natural bentonites, such as those found in Argentina, can withstand temperatures up to 620 °C. The activated bentonites withstand about 450 °C. (Mariotto, 2005; Amadio et al., 2017).

3.2.2.2 Kaolinite

Kaolinite ($Al_2Si_2O_5(OH)_4$) is one of the most abundant natural minerals in soils and sediments, normally associate to clays, and particularly to kaolin. I; it is a dioctahedral 1:1 phyllosilicate formed by superposition of silicon tetrahedral sheets and aluminum octahedral sheets. Adjacent layers are

linked by van der Waals forces and hydrogen bonds. This interlayer induces restricted access to the interlamellar aluminol groups (Al-OH) that may be used for grafting reactions.

Kaolinite is a clay with a theoretical chemical composition, expressed as a mass percentage of oxides, of 39.50% of Al_2O_3, 46.54% of SiO_2 and 13.96% of H_2O, it may have variations in its composition (Gu and Evans, 2008; Magriotis et al., 2010; Cheng, et al., 2012; Caglar, 2012). Figure 9 shows a schematic of the kaolinite structure.

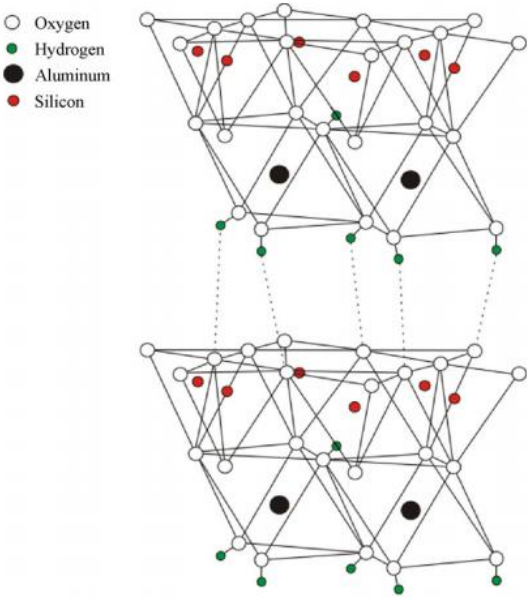

Figure 9. Schematic view of the structure of kaolinite (Cheng et al., 2012).

Kaolinite is a material with a wide variety of applications in the paper industry, where it serves as the filler material and in the ceramic coating tile industry where it is used as a pigment for coatings. It is used as an extender in

aqueous based paints and inks, a functional additive in polymers and is a major component in traditional ceramic bodies. Its great use is also largely due to the chemical inertness over a large pH range, easy dispersion, coating capacity when used as pigment and reinforcement when used as a filler. Moreover, it presents high adhesion compatibility, and low thermal conductivity and electrical conductivity (Cheng et al., 2012). Table 2 shows some values of physical and chemical properties of kaolin found in the literature.

Table 2. Selected physical and chemical properties of kaolin (Pereira and Silva, 2001; Horpibulsuk et al., 2011).

Properties	**Values**	**References**
Melting point (°C)	1650-1775	Pereira and Silva, 2001
Theoretical density (g/cm^3)	2.65	Horpibulsuk et al., 2011
pH	4.3 a 7	Pereira and Silva, 2001

The most reactive functional groups in kaolinite are hydroxyl groups, which are capable of taking part in many chemical reactions as well as ion exchange processes. It is the most abundant mineral of the kaolinite group (including dickite, nacrite, and halloysite). Depending on the application, kaolinite is often modified from its natural state by physical or chemical treatment to enhance the properties of the material (Cheng et al., 2012).

3.2.2.3 Alumina

Alumina is the inorganic product most used in the industry to obtain aluminum and ceramic products, it is obtained through the Bayer process, which is based on the physical processing of bauxite, with the presence of additives such as caustic soda at high temperatures and pressures, followed by clarification, precipitation, calcination, grinding and sizing. The structural formula of alumina is Al_2O_3 and it has only one stable natural crystallographic, the form α- Al_2O_3 called corundum (Reed, 1995; Riedel and Chen, 2010).

Figure 10 shows the crystallographic structure of alumina, with O^{2-} ions forming a compact hexagonal crystal structure and Al^{3+} cations filling the octahedral interstices (Riedel and Chen, 2010).

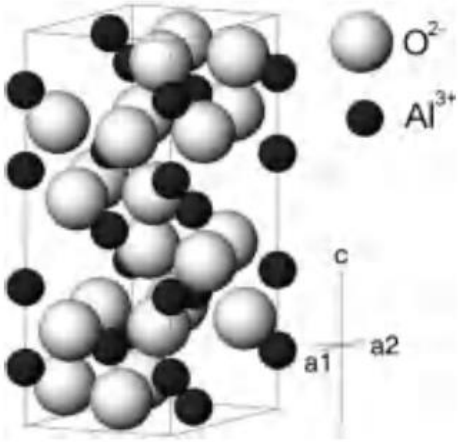

Figure 10. Corundum crystalline structure (Riedel and Chen, 2010).

Alumina ceramics are relatively low cost, and the ceramic components may be manufactured with high output

using different methods, e.g. by slip casting, pressing, or injection molding, without the use of expensive equipment such as kilns with special controlled atmosphere. These ceramics have a high level of mechanical properties; for example, some materials can be successfully used in abrasion and erosion environments; armor systems based on some kinds of alumina ceramics can defeat high-velocity projectiles with steel, lead and even tungsten carbide cores. (Medvedovski, 2006). Table 3 shows some physical, mechanical and thermal properties of alumina after sintering.

Table 3. Selected physical, mechanical and thermal properties of sintered alumina.

Properties	**Values**	**References**
Melting point (ºC)	2055	Riedel and Chen, 2010
Theoretical density (g/cm³)	3.91	Figiel et al., 2011
Hardness (GPa)	18 – 20	Acchar and Segadães, 2009
Thermal conductivity (W/mK)	40 (298˚C) 10 (1273˚C)	Riedel and Chen, 2010
Thermal expansion coefficient ($\times 10^6$/°C)	4 – 9	Acchar and Segadães, 2009
Elastic modulus (GPa)	300 – 400	Acchar and Segadães, 2009
Fracture toughness (MPa·$m^{1/2}$)	2 – 4	Acchar and Segadães, 2009
Poisson Coefficient	0.27 – 0.30	Riedel and Chen, 2010

Alumina is an excellent thermal and electrical insulator. In its crystalline form, called corundum, it has enough hardness to be used as an abrasive and as a component of cutting tools (Handbook, 2002).

Alumina is among the materials most resistant to high temperatures as well as it presents a high wear and corrosion strength and low coefficient of thermal expansion (Wood and Harris, 2008).

3.2.2.4 Silica from rice husk

Rice husk is one of the industrial byproducts of rice, a major food source around the world. It is one of the agricultural "waste" materials available in plenty in rice producing countries, which is amenable for value addition. It is reported that for every ton of rice produced, ~0.23 tons of rice husk is formed.

If rice husk can be used profitably through value addition, benefits will contribute to economic and social development particularly in developing countries. Value addition of any material including "wastes" is based on the clear understanding of its structure and properties.

Rice husk is an abundantly available waste material in all rice producing countries. In certain regions, it is sometimes used as a fuel for parboiling paddy in the rice mills. Rice husk consists of organic materials (e.g. cellulose, hemicellulose and lignin) (~75 wt%), amorphous silica (~15 wt%) and water (~10 wt%). (Chandrasekhar et al., 2003; Wu et al., 2009).

On thermal treatment, SiO_2 converts to cristobalite, which is a crystalline form of silica. However, under controlled burning conditions, amorphous silica with high

reactivity, ultra-fine size and large surface area is produced. This so-called microsilica can be a raw material for advanced materials like SiC, Si_3N_4, elemental Si and Mg_2Si. Due to the high pozzolanic activity, this rice husk silica also finds application in high strength concrete as a substitute for silica fume. Possibility of using this silica as filler in polymers has been also studied. Rice husk powders can be used as well as an additive to produce porous structures (Chandrasekhar et al., 2003; Wu et al., 2009).

The chemical composition of rice husk is found to vary from sample to sample. The differences in the type of paddy, crop year, climatic and geographical conditions, in addition to the sample preparation and method of analysis, could be the reason for this variation (Chandrasekhar et al., 2003, Jain et al., 1997). A typical chemical composition of rice husk (organic components) is shown in Table 4.

Table 4. Typical chemical composition (organic components) of rice husk (Chandrasekhar et al., 2003).

Constituent	**Amount present in rice husk (wt%)**
α-cellulose	43.30
Lignin	22.00
D-xylose	17.52
l-arabinose	6.53
Methylglucuronic acid	3.27
D-galactose	2.37
Total	94.99

3.2.2.5 Silver nanoparticles

Silver is a soft, malleable metal, which is stable in water and oxygen but attacked by sulfur compounds in air to form a black sulfide layer (CRC, 1997). The atomic number of silver is 47, its atomic weight is 107.868, and it exists in its common valence states of Ag^{+}, $Ag2^{+}$, and the mineral form of argentite, Ag_2S. Typical ambient concentrations of silver are presented in Table 5. Silver is present throughout the environment in small concentration (milligram to nanogram), but is not essential for animal or plant life (Lantagne, 2001).

Table 5. Typical Ambient Concentrations of Silver (adapted from CRC, 1997; Lantagne, 2001).

Content	Concentration
Total Content in Soils	0.03 – 0.9 mg/kg
Soluble Content in Soils	0.01 – 0.05 mg/kg in 1 N NH_4AOC
Content in Sea Water	0.04 µg/kg
Content in Fresh Water	0.13 µg/kg
Content in Marine Animals	3 – 10 mg/kg
Content in Humans	Blood: < 2.7 µg/L Bone: 1.1 mg/kg Liver: <5 – 32 ng/g
Content in Animals	6 µg/kg
Content in Plants	0.01 – 0.5 mg/kg
Content in Common Foods	0.07 – 20 mg/kg
Essentiality	Plants: no Animals: no

The daily dietary intake by humans is estimated at 0.0014 to 0.08 mg. When the maximum CRC intake per day (0.08 mg) is calculated over a 70-year lifetime, a total of 2.0 grams of silver are ingested per person per lifetime (0.08 mg/day x 365 days/year x 70 years = 2.0 grams/lifetime). Toxic intake for humans is 60 milligrams, while a lethal intake is 1.3 to 6.2 grams (CRC, 1997; Lantagne, 2001).

Nanosized inorganic particles, of either simple or composite nature, display unique properties and represent an increasingly important material in the development of novel nanodevices, which can be used in numerous physical,

biological, biomedical, and pharmaceutical applications. A number of recent achievements offer the possibility of generating new types of nanostructured materials with designed surface and structural properties (Sondi and Salopek-Sondi, 2004).

Nanomaterials are systems that at least one dimension is 1–100 nm in length with particular physical and chemical properties and can be used in numerous applications. Particularly silver, in the form of nanoparticles has efficient antimicrobial properties (Singh and Nalwa, 2011; Dash et al., 2012; Leon-Silva et al., 2016; Díaz-Soler et al., 2017).

Such powders can exhibit properties that differ substantially from those of bulk materials, as a result of small particle dimension, high surface area, quantum confinement and other effects. Most of the unique properties of nanoparticles require not only the particles to be of nano-sized, but also the particles be dispersed without agglomeration. Discoveries in the past decade have clearly demonstrated that the electromagnetic, optical and catalytic properties of silver nanoparticles are strongly influenced by shape, size and size distribution, which are often varied by varying the synthetic methods, reducing agents and stabilizers (Abou El-Nour et al., 2010).

Silver is often used as an antibacterial agent, in order to provide a sanitary environment for the wound healing process. It is considered historically as one of the most frequently used antibacterial substances before the invention of antibiotics. The multiplicity of silver's bactericidal mechanisms gives it a wide range of effective applications in the inhibition of bacterial growth. The introduction of nanoparticles has allowed the scientific community to enhance the antibacterial properties of silver. The increased surface area of the nanoparticles in turn induces an increased rate of interaction between the test subjects and the ionic silver

(Alexander, 2009; Nam et al., 2015; Bal et al., 2015; Dong et al., 2016; Mckevica et al., 2016; Amadio et al., 2017).

Strength of bacteria to bactericides and antibiotics has increased in recent years due to the development of resistant strains. Some antimicrobial agents are extremely irritant and toxic and there is much interest in finding ways to formulate new types of safe and cost-effective biocidal materials. Previous studies have shown that antimicrobial formulations in the form of nanoparticles could be used as effective bactericidal materials (Sondi and Salopek-Sondi, 2004).

Stoimenov and co-workers demonstrated that highly reactive metal oxide nanoparticles exhibit excellent biocidal action against Gram-positive and Gram-negative bacteria. Thus, the preparation, characterization, surface modification, and functionalization of nanosized inorganic particles opens the possibility of formulation of a new generation of bactericidal materials. It is well known that silver ions and silver-based compounds are highly toxic to microorganisms showing strong biocidal effects on as many as 16 species of bacteria including E. coli (Stoimenov et al., 2002; Sondi and Salopek-Sondi, 2004). According to WHO (World Health Organization) (WHO, 2014):

- The retention rate of silver in humans and animals is under 10% percent. The retained silver is mainly stored in the liver and skin. The half-life of silver in the liver is 50 days.
- Silver is occasionally found naturally in ground and surface water at 5 μg/L.
- Average human intake of silver is 7.1 μg/day.
- The acute lethal dose of silver nitrate is a minimum of 10 g.
- Argyria is the only known human health effect of silver, and is a condition in which silver is deposed on skin and hair.

The U.S. EPA has also investigated silver to determine appropriate drinking water standards and it recommends a maximum intake of 5 μg/kg/day. In the average 70-kilogram adult, this is equivalent to 350 μg/day. This recommendation was established to prevent argyria, a medically benign but permanent bluish-gray discoloration of the skin. Argyria results from the deposition of silver in the dermis and also from silver-induced production of melanin. Argyria is more pronounced in areas exposed to sunlight due to photoactivated reduction of the metal, and although the deposition of silver is permanent, it is not associated with any adverse health effects. In addition, no evidence of cancer in humans has been reported despite frequent therapeutic use of the compound over the years. Silver was used for centuries to treat syphilis, and as an astringent in topical preparations. (U.S. EPA**,** 1999).

Argyria has been described in syphilitic patients in poor health who were therapeutically dosed with a total of about 1 g of silver in the form of silver arsphenamine together with other toxic metals. There have been no reports of argyria or other toxic effects resulting from the exposure of healthy persons to silver. On the basis of present epidemiological and pharmacokinetic knowledge, a total lifetime oral intake of about 10 g of silver can be considered as the human NOAEL (no observed adverse exposure limit). As the contribution of drinking water to this NOAEL will normally be negligible, the establishment of a health based guideline value is not deemed necessary. On the other hand, special situations may exist where silver salts are used to maintain the bacteriological quality of drinking water. Higher levels of silver, up to 0.1 mg/L (a concentration that gives a total dose over 70 years of half the human NOAEL of 10 g), could then be tolerated without risk to health (WHO, 2014).

Generally, specific control of shape, size, and size distribution is often achieved by varying the synthesis

methods, reducing agents and stabilizers (Yeo et al., 2003; He et al., 2004; Abou El-Nour et al., 2010).

Metal nanoparticles can be prepared by two routes, the first one is a physical approach that utilizes several methods such as evaporation/condensation and laser ablation. The second one is a chemical approach in which the metal ions in solution is reduced in conditions favoring the subsequent formation of small metal clusters or aggregates (Khomutov and Gubin, 2002; Oliveira et al., 2005; Abou El-Nour et al., 2010).

Characterization of nanoparticles is important to understand and control nanoparticles synthesis and applications. It is performed using a variety of different techniques such as transmission and scanning electron microscopy (TEM, SEM), atomic force microscopy (AFM), dynamic light scattering (DLS), X-ray photoelectron spectroscopy (XPS), powder X-ray diffractometry (XRD), Fourier transform infrared spectroscopy (FTIR), and UV–Vis spectroscopy (Khomutov and Gubin, 2002; Yeo et al., 2003; He et al., 2004; Abou El-Nour et al., 2010).

4 Motivation, novelty and structure of the thesis

4.1 Motivation and novelty

Table 6 shows selected works performed in the last 20 years on fabrication and characterization of porous ceramic filters for water purification, with some respective performance parameters.

In the majority of the works mentioned, pressing was used as shaping technique. Freeze casting is generally used for other applications. The closest approach regarding our focus in this work, with the similar parameters, was that of Li and Li (2012). Nevertheless, they used TBA (tert-butyl alcohol) as a solvent instead of water, which increases the cost and toxicity of the process. This work presents as novelty the idea of fabricating water filter by freeze-casting using alumina and kaolinite aqueous slurries.

Table 6. Selected recent works on fabrication and characterization of pressed and freeze-cast ceramics.

Author/Year	Composition	Pores size (μm)	Porosity (total) (%)	Flow rate (l/h)	Mechanical Strength (MPa)	Shaping
Lantagne(2001)	60% clay 40% sawdust	0.6-3	-	1-3	-	Pressing
Yoon et al (2008)	10-25% alumina camphene	102-210	59-82	-	11-95	Freeze casting
Bielefeldt et al (2009)	60% kaolinite 40% sawdust	-	-	1-2	-	Pressing
Soon et al (2009)	calcium phosphate camphene	122-166	62-65	-	5-11	Freeze casting
Brown and Sobsey (2010)	clay rice husk water	-	-	1.5-3		Pressing
Simonis e Basson (2011)	lithium aluminum silicate	2-3	-	1-2	-	Pressing
Yakub et al (2012)	clay/sawdust 50/50 65/35 75/25	0.5-1.1	35-47	-	5-9.5	Pressing
Li and Li (2012)	10-20% alumina tba solvent	-	63-82	-	2.6-37	Freeze casting
Van der Laan et al (2014)	50-55% clay 17-24% rice husk 1-2% laterite	-	-	2-21	-	Pressing
Simão et al (2015)	kaolinite limestone feldspar albite quartz white clay	0.7-1.2	28-32	-	20-68	Pressing
Seuba et al (2016)	50-65% zirconia water dispersant	3.1- 28	53-72	-	22-200	Pressing
Cilla et al (2016)	36-40% solids	50-90	68-74	-	1.1-3	Freeze casting
Youmoue et al (2017)	85-100% mix clay 0-15% saw dust	0.01-1 and 10 (with sawdust)	30-48	0.008	1-3	Pressing

* With silver impregnation

4.2 Thesis structure

This thesis was structured in five main chapters:

- *Bentonites functionalized by impregnation with TiO2, Ag, Pd and Au nanoparticles*

This part of the work was carried out at ISTEC/CNR, Italy. It aimed to characterize bentonites with different features and origins (Brazil, Argentina, Italy and United States) that were impregnated with Ag, TiO2, Pd and Au nanoparticles. Either commercial (TiO2) or synthesized (Ag, Pd and Au) nanoparticles (NP) were used and characterized by DLS and XRD. Subsequently, the dispersed NP were impregnated on bentonite by two alternative methods, imbibition or dipping. The efficiency of impregnation of bentonite by metallic nanoparticles was finally tested by ICP-OES.

- *Fabrication of pressed porous ceramic filters for water purification with kaolinite and/or alumina*

In this chapter, the work aimed to obtain porous ceramic filter with kaolinite and/or alumina, by pressing, using rice husk as a sacrificial agent, for water filtration. Rice husk was characterized by TG, DSC and SEM. Many compositions were tested with kaolinite and/or alumina, with or without rice husk, and with and without water. The mechanical strength was measured by compression tests, and pre-tests of permeability of the final pellets were performed.

- *Influence of alumina particle size on the performance of freeze-cast filters*

This chapter aimed to verify the influence of the particle size on freeze cast filters. Two alumina powders (coarse and fine) of the same kind and from the same manufacturer were

used, corresponding to particle sizes of 2.5 and 0.5 µm respectively. It was intended to analyze what is the more suitable for freeze-casting for the application of ceramic filter for drinking water (pellets). The powders of alumina were characterized by average particle size and distribution, zeta potential, XRF, density by picnometry, specific surface area (BET), and SEM. Parameters like rheology, solidification rates, compression resistance, porosity and permeability were analyzed.

- *Fabrication of freeze-cast porous alumina/kaolinite filters for water purification*

This chapter aimed to obtain ceramic filter pellets with alumina and kaolinite, by freeze-casting method, for water filtration applications. The powders were characterized by analyses of average particle size, zeta potential, TG, DSC, XRD, XRF, density by picnometry, and specific surface area (BJH). The mechanical strength was measured under compression, and permeability evaluation was based on Forchheimer's equation; final pellets were analyzed by SEM, and their filtration efficiency was assessed using Colilert and Quanti-Tray/2000.

- *Freeze-cast porous ceramic filters impregnated with silver nanoparticles*

In this chapter pellets of porous ceramic filters of alumina and kaolinite were impregnated with silver nanoparticles to test the bactericidal efficiency. Silver nanoparticles were characterized by average particle size, zeta potential, SEM/EDS and TEM. The AgNPs were impregnated by dipping (method developed in the first part of this work). After impregnation, leached water was analyzed by graphite furnace atomic absorption spectrometry (GFAAS) to measure efficiency in silver impregnation.

5 Bentonites functionalized by impregnation with TiO_2, Ag, Pd and Au nanoparticles[1]

5.1 Introduction

Bentonite is a clay composed by montmorillonite and/or other terms of the smectite group, and minor non-clay minerals. Montmorillonites are swellable dioctahedral 2:1 layersilicates, which consist of stacks of several so-called 2:1 layers. This clay mineral has a permanent negative charge that arises from isomorphous substitution of Al^{3+} for Si^{4+} at the tetrahedral sheet and Mg^{2+} for Al^{3+} at the octahedral sheet. This negative charge is naturally compensated by exchangeable cations (i.e. Na^{+}, Ca^{2+}) located in the interlayer space (Bergaya et al., 2006). Montmorillonite has a high cation exchange capacity (CEC), marked swelling and high specific surface area leading to a strong adsorption/desorption capacity of ionic or polar compounds (Ikhtiyarova et al., 2012; Parolo et al., 2014).

When individual lamellae of montmorillonite are exposed to water, the water molecules are adsorbed on silica sheets, which are then separated from each other. This interlayer swelling is controlled by the cation associated with the clay structure. The thickness of the water interlayer varies with the nature of the cation adsorbed and the amount of water available (Brindley, 1955; Bergaya et al., 2006).

Sodic bentonites expand many times their volumes when in contact with water. If the cation is Na^{+}, the swelling may progress from 12.5 Å, when the clay is exposed to air, to a maximum of 40.0 Å, when the clay is fully dispersed in a liquid medium (Lummus and Azar, 1986). The sodic natural

[1] Published in Applied Clay Science, Volume 146, 15 September 2017, Pages 1-6.
http://www.sciencedirect.com/science/article/pii/S016913171730234X

bentonites, such as those found in Argentina, can withstand temperatures up to 620 °C. The activated bentonites withstand about 450 °C.

The features of a bentonite directly depend on its composition, impurities and origin (Paiva et al., 2008; Holtzer et al., 2011). The bentonites that do not have the desired properties for an application can be modified in some ways to reach the requirements and market demands, for example, by impregnation of nanoparticles. According to current definitions, nanomaterials are considered natural, fabricated or incidentally formed materials having 50% or more particles with one or more external dimensions in the range of 1-100 nm (European Commission, 2011). Their outstanding properties have been described in many books, comprehensive reviews and research papers (e.g., Rao et al., 2007).

Clay minerals may be regarded as natural nanostructured materials, since their crystallites are usually characterized by one dimension in the nanorange. Clay minerals present external surfaces including edges and internal surfaces of interlayer spaces. A clay particle is an assembly of layered crystallites and a clay aggregate is an assembly of clay particles. Therefore, we may distinguish between interlayer, interparticle, and interaggregate pores of different sizes and shapes (Bergaya et al., 2006; Praus et al., 2013; Abreu et al., 2015).

Bentonites with more than 70% montmorillonite have attracted considerable interest because they are easily available in bulk quantities, economically attractive and environmentally friendly. They have excellent swelling and adsorption properties, being used as a support to disperse and stabilize nanoparticles in various applications (Ayari et al., 2005; Hashemian, 2010; Zamparas et al., 2012; Motshekga et al., 2015).

Nanoparticles of metals and metal oxides, such as Ag, Au, Pd and TiO_2 have physical and chemical properties that

depend on their size and shape. The size reduction to nanometric dimensions causes the material to acquire a behavior between "bulk" and molecular. One of the features related to the decrease in particle size is the increasing of surface area, which greatly enhances their applications that depends on surface sites.

The objective of this part of the work is to develop a novel route, which may be transferred to the industry, aiming the functionalization of bentonites through the impregnation of nanoparticles. This implies a dual target: primarily, to enable bentonites to acquire properties that are not preexistent (improving their performance in current uses and disclosing new applications) and, additionally, to exploit the use of bentonite as encapsulating matrices for the handling and transportation of nanoparticles. In the latter case, new promising prospective uses are open for the development of cost-effective, molecular designed solutions that decrease the potential risk associated to NP exposure (Ortelli and Costa, 2016; Costa et al., 2016) thanks to the encapsulating effects of environmental friendly bentonite. In line with the performance requirements of a sustainable and safer design approach, the mesoporosity of bentonite hosting structure should also guarantee the preservation of NP reactivity.

5.2 Materials and methods

5.2.1 Raw materials and synthesis methods

Bentonites from Brazil (QB; T-Cota), Argentina (BL; T-Cota), Italy (P1 and P4; Laviosa) and United States (WY; Laviosa) were characterized by surface area (BET, Quantachrome, NOVA 2200e, USA) swelling (Foster method), chemical composition (XRF, Epsilon 3, PANalytical), particle size distribution by sedimentation (SediGraph 5100, Micromeritics), CEC (cation exchange capacity) by the methylene blue method. Thermal analyses (TG and DSC) were performed simultaneously (Netzsch,

STA449 Jupiter, Germany) within the 25-1000 °C range under air atmosphere at a heating rate of 5 °C min^{-1}.

TiO_2 nanosols (nanoparticle dispersions) were commercially available (Cericol, Colorobbia), with a solid loading of 1 wt%); Ag, Au and Pd nanoparticles were synthesized in the laboratory. The following analytic grade reagents (Sigma-Aldrich, USA) were used: $AgNO_3$, $HAuCl_4$, NaOH, and $PdCl_2$, as well as polyvinylpyrrolidone (PVP, Mw 29000, Sigma-Aldrich, USA) and D(+) glucose (Merck, Germany). Metallic nanoparticles were prepared by using a microwave assisted eco-friendly method (Blosi et al., 2014). Ag colloids were obtained through the reduction of $AgNO_3$ in the presence of PVP. First, 3.13 g of PVP were dissolved in 90 ml of distilled water, then 0.28 g of NaOH and 0.90 g of D(+) glucose were added to the solution. When all the reagents were dissolved, the solution was heated at 70 ºC, 10 ml of an aqueous $AgNO_3$ solution (0.5 M) was injected, and the reaction was allowed to proceed for 3 min. By adding $AgNO_3$, the solution immediately turned brown with intense yellow shades. Highly stable suspensions with a solid loading of 0.5 wt% were initially achieved and, by using optimized conditions, the solid loading was further increased to 4 wt% (Blosi et al., 2010; Blosi et al., 2014).

Au nanoparticles were synthesized by mixing PVP (0.35 g) and glucose (from 0.20 to 0.40 g) in a round bottom flask containing water (80 ml). The solution was microwave-heated at ambient pressure to a temperature ranging from 70 to 90 °C (heating rate of 30 °C/min). At this temperature, aqueous NaOH (0.88 M) and $HAuCl_4$ (10 ml, 0.11 M) solutions were added to the flask and stirred for 2.5 min. After the reaction, a red, stable suspension of gold nanoparticles with a solid loading of 0.2 wt% was obtained (Blosi et al., 2010; Blosi et al., 2014).

Pd nanoparticles were synthesized through reduction of $PdCl_2$. The experiments were performed following the same

procedure used for gold colloids. In the Pd case, only the NaOH/metal molar ratio was adjusted during the synthesis optimization procedure (Blosi et al., 2010; Blosi et al., 2014).

5.2.2 Processing and characterization

The nanoparticles used in this study (Ag, TiO_2, Au and Pd) were characterized by XRD (Bruker, D8 Advance with LynxEye detector, Germany) with a 2θ range from 0 to 80°, 0.02 step size, 16 s (equivalent) time-per-step, and DLS (Malvern, MPT-2, UK), working at a fixed angle of 173°. XRD was performed on the nanoparticles in an aqueous suspension to overcome problems due to the high hygroscopicity of the dried particles. Some drops of the suspension were deposited on a borosilicate sample holder and submitted to XRD analysis. Although this procedure is not conventional, it has been mentioned in the literature (Cruciani et al., 2011; Taglieri et al., 2013).

QB and BL bentonites were impregnated with Ag, TiO_2, Au and Pd nanosols. In the direct method or imbibition, the nanoparticles suspensions were dropped on a certain amount of powder. The imbibition was performed with spatula and mortar until the initial coloration of bentonite was not more observed. The procedure was repeated varying the nanoparticle percentage in relation to the bentonite mass: 1 and 2 wt% Ag, 1 to 3 wt% TiO_2 and 0.1 wt% Au and Pd.

The impregnation efficiency was characterized in samples of bentonites impregnated with nanoparticles (2 wt% Ag, 3 wt% TiO_2 and 0.1 wt% Au and Pd), after washing with water. The clay was dispersed in distilled water (10 wt% clay/water), the slurry underwent a magnetic stirring and was then centrifuged with 5000 rpm during 10 min. The supernatant (15 mL) was transferred to a plastic test tube coupled to a filter of 10 kDa to detect remaining nanoparticles. This tube was centrifuged again in the same conditions described before. The resulting solution above the filter possibly containing the nanoparticles was then collected

and analyzed by Inductively Coupled Plasma Optical Emission Spectrometry (ICP-OES, Varian, Liberty 200, Australia) and by X-ray Powder Diffraction (XRD, Bruker, D8 Advance, Germany).

Another impregnation method used was dipping. Aqueous slurries of 10 wt% Ag, TiO_2, Pd or Au nanoparticles were prepared. Samples of bentonites BL and QB were chosen to continue the tests. The samples were stored in a grid/filter with holes of 149 μm, and dipped into the respective slurries. Then, the bags were removed from the slurries and samples were taken for drying in oven at 100 °C during 1 h.

A heat treatment was performed for the bentonites QB and BL to identify the influence of temperature on the nanoparticles impregnation process. The bentonites were treated at temperatures from 100 to 700 °C. Table 1 shows the bentonites QB and BL and their method of impregnation with their Ag NP solution used and their treatments in their respective order of process.

SEM-FEG was employed to characterize Ag nanoparticles distribution within the bentonite BL matrix. In this case, samples were prepared according to either one of the following sequences:

- imbibition, thermal treatment at 100 °C – BL 1
- imbibition, thermal treatment at 700 °C – BL 3
- thermal treatment at 700 °C, imbibition – BL 7
- thermal treatment at 700 °C, dipping – BL 8

Table 5. 1. QB and BL samples and their method of impregnation with Ag NP solution and treatments in the respective order of process.

Bentonite	Ag NP Solution wt%	Impregnation Method of Ag NP		Thermal Treatment	
		Imbibition	Dipping	100 °C	700 °C
QB 1	3	1st	-	2nd	-
QB 2	10	-	1st	2nd	-
QB 3	3	1st	-	-	2nd
QB 4	10	-	1st	-	2nd
QB 5	3	2nd	-	1st	-
QB 6	10	-	2nd	1st	-
QB 7	3	2nd	-	-	1st
QB 8	10	-	2nd	-	1st
BL 1	3	1st	-	2nd	-
BL 2	10	-	1st	2nd	-
BL 3	3	1st	-	-	2nd
BL 4	10	-	1st	-	2nd
BL 5	3	2nd	-	1st	-
BL 6	10	-	2nd	1st	-
BL 7	3	2nd	-	-	1st
BL 8	10	-	2nd	-	1st

5.3 Results and discussion

Table 2 shows characteristic physical properties and chemical composition of the bentonites employed in this work: QB, BL, P1, P4 and WY.

The bentonite WY remained dispersed without settling down, even after 4 days of rest. Only for bentonite

QB, it was possible to measure the particle size by sedimentation. The other bentonites showed the formation of a dense and viscous layer, both in water and in alcohol, corresponding to flocculation and phase separation.

Comparing the chemical composition of bentonites to the cation exchange capacity (CEC) and swelling, it can be seen that the sodic bentonites are those which have the highest CEC and swelling values. Therefore, they attract the greatest attention from the industry.

Table 5. 2. Characterization of bentonites QB, BL, P1, P4 and WY.

Physical Properties	**QB**	**BL**	**P1**	**P4**	**WY**
CEC (meq/100 g)	38.1	74.6	87.4	58.7	76.4
Swelling (ml/2 g)	8	25	30-35	25-28	–
BET (m^2/g)	99.9	12.8	27.3	29.8	28.8
Average particle size (μm)	0.26	–	–	–	–
Chemical composition (wt%)					
SiO_2	64.34	62.27	58.61	72.66	62.90
Al_2O_3	17.23	18.24	23.36	12.59	19.60
Na_2O	0.56	3.15	3.99	2.32	1.53
K_2O	1.89	0.51	0.94	1.16	0.53
MgO	2.23	2.71	2.71	2.18	3.05
CaO	0.65	1.41	1.19	1.57	1.68
TiO_2	0.88	0.40	0.19	0.27	0.09
MnO	0.04	0.01	0.01	0.03	0.01
Fe_2O_3	5.79	5.15	2.62	2.09	3.35
Loss on Ignition	6.36	5.88	6.35	5.08	6.06

The thermogravimetric behavior of bentonites is similar in all samples (Figure 1A). There is a significant initial loss of mass, around 100 °C, related to water adsorbed on the

external surface of the material and located in the interlayers of the crystalline structure. The mass lost between 500 and 650 °C corresponds to dehydroxylation. From 700 °C on, the curves present practically no longer any significant loss of mass. WY and P1 bentonites had the lowest and the highest mass losses, respectively. These transformations are shown in DSC curves (Figure 1B). In addition, it is possible to observe a significant exothermic peak between 800 and 900 °C, characteristic of crystallization of a new phase. At 910 °C, an event represents the decomposition of dolomite impurity. Above 900 °C major structural changes resulting in the development of cristobalite and mullite in montmorillonite can occur (Galindo et al., 2013; Caglar et al., 2009; Bergaya et al., 2006; Occelli and Tindwa, 1983; Neaman et al., 2003).

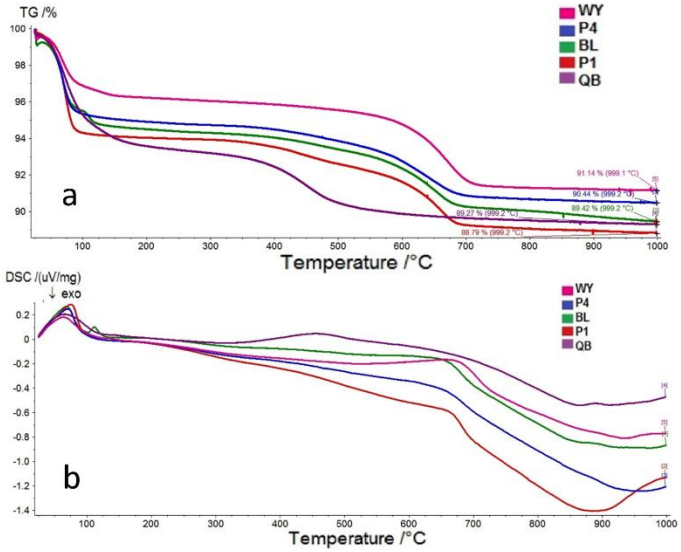

Figure 5. 1. Thermal analyses of bentonites QB, BL, P1, P4 and WY: (a) TG; (b) DSC.

Figure 2 shows the particle size distribution measured by DLS of TiO_2, Au, Pd and Ag nanoparticles. Nano-TiO_2 (Figure 2A) presents a bimodal distribution possibly due to agglomeration, with peaks respectively at ~6 and ~70 nm. For 3 different measurements, the distribution is constant. Figure 2B shows minor peaks in the micrometric range (5 μm) that occur due to agglomeration of nano-Au. The highest peak occurs between 100 and 200 nm, with primary nanoparticles in the range of 20 to 30 nm. Figure 2C shows that Pd nanoparticles have a variation of peaks for each analysis, which demonstrates a possible instability of the suspension. The occurrence of several peaks may occur due to an agglomeration of nano-Pd. A major peak is located at about 200 nm, with the smallest fraction at 10 to 30 nm. Figure 2D shows the distribution of Ag nanoparticles with constant, well-defined peaks. In this case, no detectable agglomeration occurred. A single peak can be observed at approximately 90 nm.

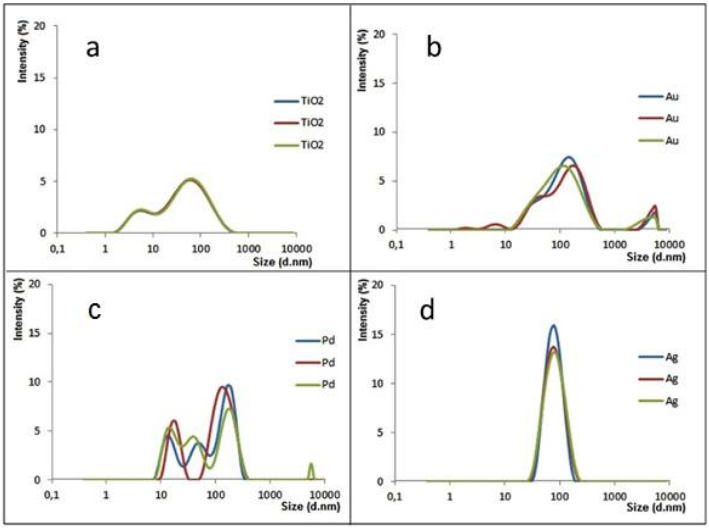

Figure 5. 2. Particle size distribution (three DLS repetitions) of nanoparticles: (a) TiO_2, (b) Au, (c) Pd and (d) Ag.

The nanoparticles were characterized by XRD directly in their aqueous suspension (Figure 3). The broad band at ~28° in Figures 3A, 3B and 3C, typical of borosilicate glass, can be observed because of the low concentration of nanoparticles and to the glassy nature of the sample holder. In Figure 3D, the hump at 28° is hardly visible due to the much higher concentration of TiO_2 (15.5 wt%), which presents a higher degree of crystallinity as well. Figure 3A shows the diffractogram of nano-Ag (1 wt% in water) with indication of the peaks of silver. A similar feature occurs for nano-Au (Figure 3B) even if its concentration in the aqueous suspension is as low as 0.011 wt%. Figure 3C shows the diffractogram of nano-Pd, which does not present well-defined peaks. This can be attributed to the low concentration (0.011 wt% in water) and small size (under 20 nm) of primary Pd nanoparticles in the suspension. Figure 3D shows the diffractogram of nano-TiO_2 (15.5 wt% in water). Two crystalline phases were detected, being anatase predominant over brookite.

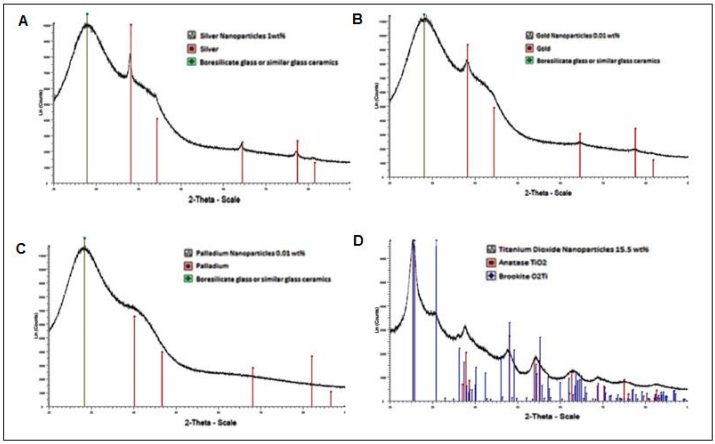

Figure 5. 3. XRD patterns of nanoparticles in aqueous suspension: (a) 1 wt% Ag; (b) 0.01 wt% Au; (c) 0.01 wt% Pd; (d) 15.5 wt% TiO_2.

A leached solution resulting from washing the impregnated bentonite samples QB (QB 7 and QB 8) and BL (BL 7 and BL 8) with water was analyzed by ICP-OES (Table 3). Both imbibition and dipping processes showed satisfactory results for the impregnation efficiency. All values of residual nanoparticles in the bentonites are above 90%. In the case of Ag, above 99% of nanoparticles were retained by the bentonite after washing with water. TiO_2 could not be measured by ICP-OES due to low accuracy of the detection method for this sample. According to Motshekga et al. (2015), the nanoparticles in the bentonites were proven to be stable, with leaching values under the accepted WHO standards (0.1 mg/l) (WHO, 2011).

Table 5. 3. Metal nanoparticles retained by bentonites QB and BL after washing with water, as measured by ICP-OES.

Bentonite samples	**Residual nanoparticles in bentonite (wt%)**		
	Ag	Au	Pd
QB 7	99.4	92.7	91.5
BL 7	99.8	95.2	94.6
QB 8	99.5	94.6	91.7
BL 8	99.8	96.4	95.8

Based on these results, bentonite BL and Ag nanoparticles (BL 1, BL 3, BL 7 and BL 8) were selected for further SEM-FEG analyses (Figure 4). The micrographs correspond to the bentonites impregnated with nanoparticles by either imbibition or dipping, and submitted to a heat treatment at either 100 or 700°C. The lighter spots in the micrographs indicate that the Ag nanoparticles are not agglomerated and are homogenously distributed in the clay matrix.

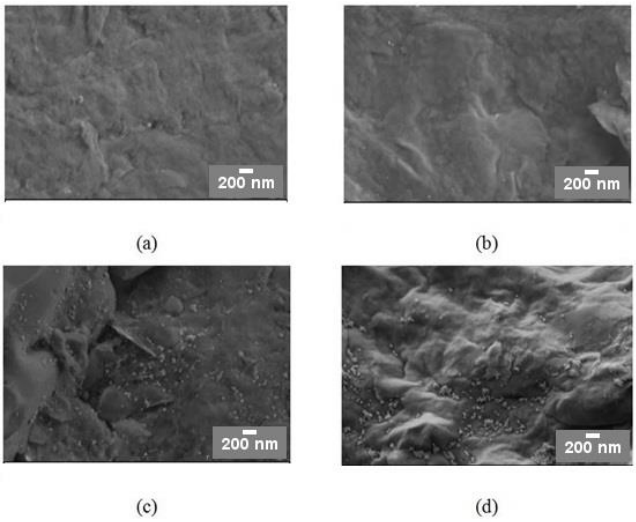

Figure 5. 4. SEM-FEG micrographs of Ag nanoparticles impregnated in bentonite BL: (a) BL 1; (b) BL 3 (c) BL 7 (d) BL 8.

5.4 Conclusions

Bentonite-nanoparticles composites have been successfully obtained by simple impregnation procedures, easily transferable to industry, which can be performed either by imbibition or by dipping.

Best results were achieved submitting bentonites to a preliminary heat treatment at 700 °C. The impregnation efficiency after washing with water is over 99% in the case of nano-Ag, and over 90% for Au, Pd and TiO_2 nanoparticles. Such a different behavior could be related to the colloidal stability of nanosuspensions used during impregnation.

Nano-Ag was characterized by a higher stability and particle dispersion in suspension, while Au, Pd and TiO_2 nanoparticles suffered from some agglomeration and their suspensions exhibited an unstable behavior.

6 Fabrication of pressed porous ceramic filters for water purification with kaolinite and/or alumina[2]

6.1 Introduction

The access to clean and safe water is of paramount importance for human health. It is estimated that in the 21st century more than one billion people do not have access to safe drinking water. Much of this population is concentrated in underdeveloped countries, especially in rural areas. Small communities have the most difficulty in receiving water in sufficient quantity and quality, population is exposed to diseases transmitted through the water (Mwabi et al., 2011).

Porous ceramic filters are among the most effective treatments for water purification. Ceramic filters have been widely used for microbiological treatment of water due to its low cost. Porous ceramics may be manufactured from oxides such as alumina, titania, or zirconia. The advantages of porous ceramics over other filtration techniques and materials are their chemical, thermal and pH stability. Allied to the previous features, there is also the longevity and strength to pressure, temperature and corrosion, bringing an excellent cost/benefit relationship (Lv et al, 2009; Bielefeldt et al, 2009; Simonis and Basson, 2011).

Several processing routes such as replica, sacrificial template, or direct foaming methods are available for the production of macroporous ceramics. The techniques differ greatly in terms of processing features and final microstructures/properties achieved (Studart et al., 2006).

The sacrificial template technique usually consists of the preparation of a biphasic composite comprising a continuous matrix of ceramic particles or ceramic precursors

[2] Submitted.

and a dispersed sacrificial phase that is homogeneously distributed throughout the matrix and ultimately extracted to generate pores within the microstructure. This method leads to porous materials displaying a negative replica of the original sacrificial template, as opposed to the positive morphology obtained from the replica technique (Studart et al., 2006).

The extraction of the sacrificial material from the consolidated composite depends primarily on the type of pore former employed. Predominantly open pores of various different morphologies can be produced with this method. The mechanical strength of cellular structures produced is often substantially higher than that achieved with the positive replica techniques (Aranberri et al., 2009; Studart et al., 2006).

Rice husk is an abundantly available waste material in all rice producing countries. It consists of organic materials (e.g. cellulose, hemicellulose and lignin) (~75 wt%), amorphous silica (~15 wt%) and water (~10 wt%). In certain regions, rice husk is sometimes used as a fuel for parboiling paddy in the rice mills. The partially burnt rice husk in turn contributes to more environmental pollution. There have been efforts not only to overcome this but also to find value addition to these wastes using them as secondary source of materials. In respect of environmental friendly and cost-effectiveness, the rice husk powders have been used as an additive to produce porous structure (Chandrasekhar et al., 2003; Wu et al., 2009).

In this work, water filters were obtained by a simple uniaxial pressing from alumina and/or kaolinite powders with and without rice husks, as pore forming agents.

6.2 Materials and methods

6.2.1 Raw materials and processing

The powders used as raw materials for the porous filters were kaolinite, (Colorminas) and alumina (CT 3000, Almatis). Rice husk was provided by Arroz Fumacense (Morro da Fumaça, SC, Brazil) was used as a porogenic agent and characterized by moisture content, TG/DSC (STA 449 F3, Jupiter) and SEM (TM3030, Hitachi).

For the moisture tests, the samples were prepared according to NBR 6923 (1981), and set in a furnace at 105 °C during 6 h, with measures after 3, 4, 5 and 6 h. Moreover, NBR 8112 (1986) and ASTM E871 (2014) were applied (ABNT 1981; ABNT 1986; ASTM, 2014).

Rice husks were milled in a jar mill (CB2-T, BP), during 20 min. Fractions of rice husks of different sizes were taken. After every milling around 15 g powder (<70 mesh, 210 µm), 12 g (between 35 and 70 mesh), and 11 g (>35 mesh, 420 µm) was obtained.

The samples were pressed at 10, 20, 30, or 50 MPa, during 1 to 5 min to produce pellets with 20.0 ± 0.5 mm diameter and 6.5 ± 1 mm length. A heat treatment was done to remove the porogenic agent (rice husks) and the organic dispersant (Darvan CN, Vanderbilt), at 1 ºC/min up to 500 ºC with a soaking time of 1 h at 500 ºC, in a resistive furnace (J-200, Jung). Then, samples with only kaolinite were sintered at 900, 1000 and 1100 ºC, and samples of alumina, with or without kaolinite, were sintered at 1500, 1550 and 1600 ºC, with a heating rate of 5 °C/min, and dwell time of 1 and 2 h, respectively, for kaolinite and alumina, at the maximum temperature, in another resistive furnace (EDG-1600).

6.2.2 Formulation and characterization

Different compositions were tested, as shown in Table 1.

Table 6. 1. Composition of samples with kaolinite (K) and/or alumina (A).

Sample	Alumina (wt%)	Kaolinite (wt%)	Water (wt%)	Darvan (wt%)	RH < 70 mesh (wt%)	35 mesh < RH < 70 mesh (wt%)
K1	-	60	-	-	40	-
K2	-	70	-	-	30	-
K3	-	80	-	-	20	-
K4	-	90	-	-	10	-
K5	-	60	-	-	-	40
K6	-	70	-	-	-	30
K7	-	80	-	-	-	20
K8	-	90	-	-	-	10
K9	-	35	33.5	1.5	30	-
K10	-	40	33.5	1.5	25	-
K11	-	50	18.5	1.5	30	-
K12	-	55	23.5	1.5	20	-
K13	-	60	18.5	1.5	20	-
A1	60	-	-	-	40	-
A2	70	-	-	-	30	-
A3	80	-	-	-	20	-
A4	90	-	-	-	10	-
A5	60	-	-	-	-	40
A6	70	-	-	-	-	30
A7	80	-	-	-	-	20
A8	90	-	-	-	-	10
A9	35	-	33.5	1.5	30	-
A10	40	-	33.5	1.5	25	-
A11	50	-	18.5	1.5	30	-
A12	55	-	23.5	1.5	20	-
A13	60	-	18.5	1.5	20	-
KA1	25	25	28.5	1.5	20	-
KA2	40	10	28.5	1.5	20	-
KA3	30	20	28.5	1.5	20	-
KA4	10	40	28.5	1.5	20	-
KA5	20	30	28.5	1.5	20	-
KA6	30	30	18.5	1.5	20	-
KA7	50	10	18.5	1.5	20	-
KA8	40	20	18.5	1.5	20	-
KA9	10	50	18.5	1.5	20	-
KA10	20	40	18.5	1.5	20	-

The samples with compositions of Table 1 were pressed at 10, 20, 30, or 50 MPa, during 1 to 5 min. For the porosity desired, a pressure as low as possible is better, but the samples needed a minimal mechanical strength to keep the shape. Considering it, the best results were obtained applying 10 MPa, during 3 min.

Samples of alumina with or without kaolinite, were moved to another furnace and sintered at 1550 ºC (minimum temperature with complete sintering of alumina), with a heating rate of 5 °C/min, and dwell time of 2 h at the maximum temperature.

For the determination of apparent density, water absorption) and apparent porosity of the final filter, ASTM C20-00 (2015) was applied. The compression strength was measured by a universal mechanical testing machine (DL 20000, Emic), with a load cell of 20 N and a loading velocity of 0.5 mm/min, according to ASTM C133 (1997). Pre-tests of permeability of the final pellets were carried in a lab build apparatus, using a glass funnel on the top of a graded burette. Each pellet was placed in the glass funnel and sealed with silicone to prevent the water leaking. The flow rate was measured by the amount of water passing through the filter in ml/h.

6.3 Results and discussion

The moisture of rice husk samples was determined after 3, 4, 5 and 6 h at 105ºC (Figure 1A). The main loss of water occurred in the first 3 h, around 10 wt%. From 3 to 6 h, there was no significant weight loss. Figure 1B shows the corresponding total solids loss.

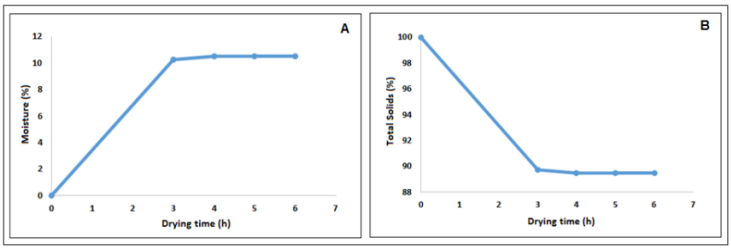

Figure 6. 1. Drying of rice husk: (a) residual moisture, (b) total solids loss.

Figure 2 shows the results of thermogravimetric analysis confirming an initial mass loss of 10% around 100 ºC, corresponding to the sample moisture, and a sharp loss of mass between 250 and 400 ºC, where rice husk decomposition occurs.

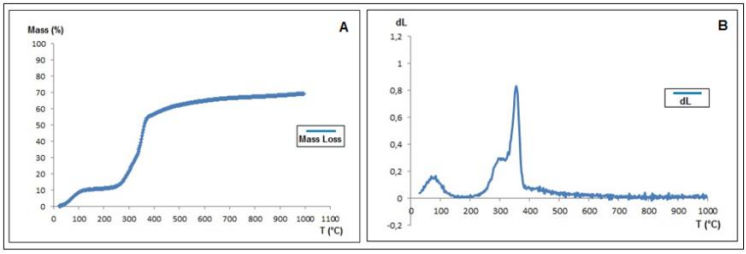

Figure 6. 2. Thermogravimetric analysis of rice husk: (a) TGA, (b) DTG.

Figure 2B shows the derivative of the mass loss curve, where a small peak of the water loss of the sample is observed at ~100ºC and then a very sharp peak showing the critical temperature where the rice husk decomposition takes place can be seen at ~370 °C. Next to this peak, a shoulder starting at 300 °C may correspond to the constitutional water loss of the sample.

A DSC analysis of the rice husk, Figure 3, shows a small endothermic peak due the water loss, and a gradual exothermic feature due to the combustion of the rice husk.

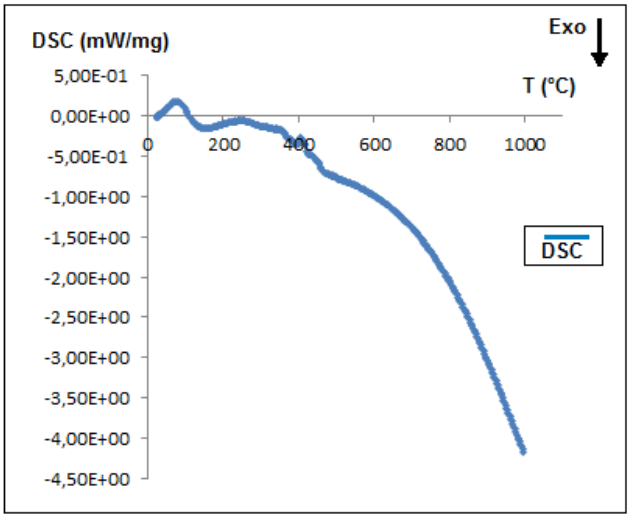

Figure 6. 3. DSC curve of rice husk.

Figures 4A and 4B show micrographs of the rice husk respectively before and after milling (<70 mesh, 210 µm)), with 3 different magnifications.

The micrographs show that the powder with less than 210 µm has a more homogenous distribution; thus, this was chosen for compaction of most of pellets compositions thereafter.

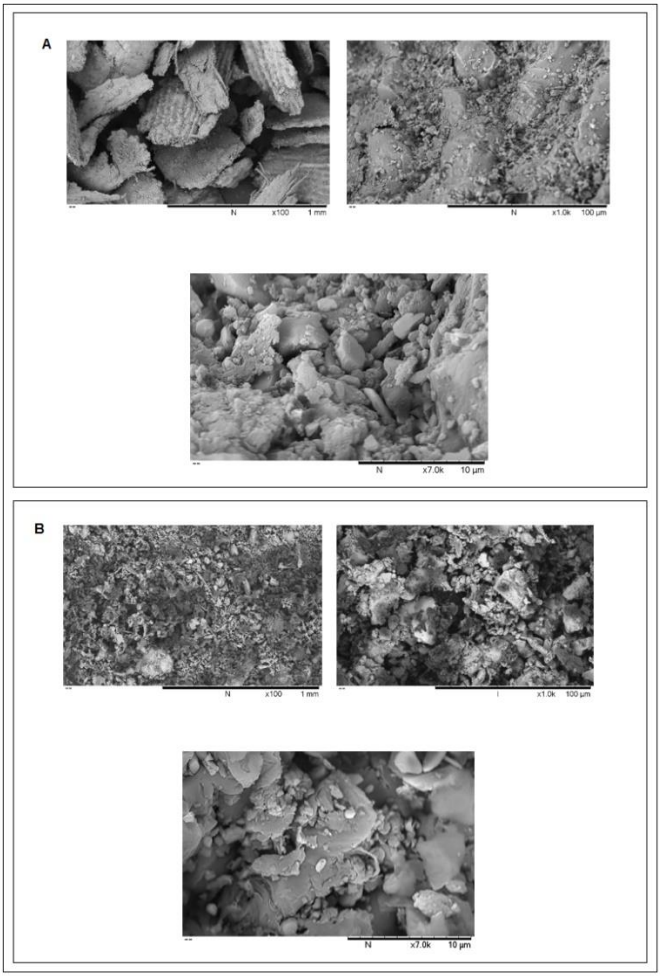

Figure 6. 4. SEM micrographs of rice husk: (a) before and (b) after milling (< 210 µm).

Table 2 shows the values of average apparent porosity and deviation of kaolinite (K) and/or alumina (A) pellets.

Table 6. 2. Average apparent porosity of kaolinite (K) and/or alumina (A) filter pellets.

Kaolinite			Alumina			Kaolinite/Alumina		
Sample	**Apparent Porosity (%) Average**	**Average Deviation (±)**	**Sample**	**Apparent Porosity (%) Average**	**Average Deviation (±)**	**Sample**	**Apparent Porosity (%) Average**	**Average Deviation (±)**
K1	38.2	0.5	A1	28.7	0.2	KA1	62.4	1.2
K2	37.5	0.7	A2	31.6	0.2	KA2	67.6	0.9
K3	32.3	0.8	A3	27.9	0.6	KA3	63.2	1.8
K4	30.1	0.4	A4	34.6	0.4	KA4	61.6	1.8
K5	39.4	0.7	A5	31.2	0.4	KA5	61.3	0.8
K6	37.1	0.3	A6	29.8	0.6	KA6	67.2	0.9
K7	34.6	0.7	A7	34.8	0.7	KA7	59.4	1.6
K8	31.8	0.7	A8	29.9	0.5	KA8	65.8	1.3
K9	54.1	0.4	A9	57.8	0.4	KA9	68.2	1.3
K10	49.7	0.6	A10	54.3	0.3	KA10	61.4	1.4
K11	51.2	0.4	A11	52.8	0.8			
K12	52.4	0.4	A12	56.2	0.5			
K13	49.6	0.7	A13	54.7	0.6			

Samples with only kaolinite have low porosity but their densification was incomplete, the samples did not reach enough mechanical strength for their handling without rupture. Samples with only alumina have a higher densification, in consequence, lower porosity; the higher porosities occurred in samples with lower percentage of solids (35 to 60 wt%). Alumina and kaolinite mixtures with total

solids of 50 and 60 wt% had similar porosity and higher values than samples with only alumina or kaolinite.

The mechanical tests showed that all the samples had an average compression strength of 90 ± 5 MPa, corresponding to high densification and low permeability to be used as a filter. During the tests of water flow rate, with samples with only alumina or kaolinite, some defects could be observed in the pellets, as shown in Figure 5.

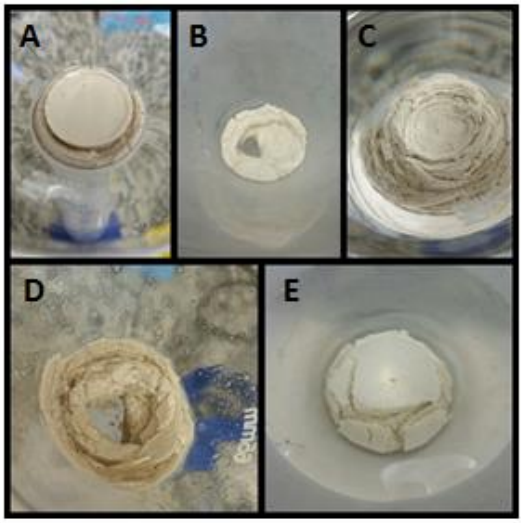

Figure 6. 5. Different defects that appeared in the pellets during the tests of permeability (flow rate). A) Walls falling apart; B) Flow through the funnel; C) Division into layers; D) Center went down ; E) Cracks.

All samples with both kaolinite and alumina (KA1, KA2, KA3, KA4, KA5, KA6, KA7, KA8, KA9 and KA10) presented a suitable strength after contact with water. The pellets remained constant, but the water flow rate did not reach values high enough for water filtering, with less than 0.01 l/h. According to Lantagne (2001), Bielefeldt et al.

(2009) and Salvinelli et al. (2016), a flow rate recommend to water filters is 1-3 l/h.

6.4 Conclusions

Filter samples made only with kaolinite presented low porosity and their densification was incomplete after sintering at 1100 ºC. They did not reached enough mechanical strength for their handling without degradation.

Alumina samples were denser, i. e., less porous, which were not suitable for water filtration purposes. All the samples with kaolinite and alumina presented a good strength after contact with water, but the flow rate of less than 0.01 l/h is not indicated for water filtering.

Thus, uniaxial pressed water filters of kaolinite and/or alumina with or without rice husks are not suitable for the intended application, at least in the conditions tested here.

7 Influence of alumina particle size on the performance of freeze-cast filters[3]

7.1 Introduction

Freeze casting has received broad attention as a simple and versatile fabrication technique of porous structures, which generally offers a wider range of pore characteristics. It involves the preparation of a ceramic slip that is poured into a mold, which is then frozen and subjected to sublimation drying of the solvent under vacuum (Sofie and Dogan, 2001; Deville et al., 2007; Fukushima et al., 2008; Yoon et al., 2008; Li and Li, 2012).

Given the inherent strength of frozen solvents, this method allows the frozen solvent to temporarily act as a binder to hold the part together for demolding. Removal of the solvent by sublimation also eliminates drying stresses and shrinkage that may lead to cracks and warping during the normal drying of a solvent-saturated body (Sofie and Dogan, 2001).

Many factors influence the microstructure and properties of porous ceramics fabricated by freeze casting, such as composition and initial solids loading, cooling rate, sintering temperature, and additive content (Deville, 2008; Hu et al., 2010; Liu and Button, 2013).

Nevertheless, the effect of particle size of the ceramic powder constituent in freeze casting has attracted little attention. The particle size has a major effect on the final mechanical properties, since it is expected that smaller particles improve the densification and lead to lower porosity (Araki and Halloran, 2005; Koh et al., 2006; Yoon et al, 2007; Liu and Button, 2013).

[3] Submitted.

Fukasawa et al. applied freeze casting to fabricate porous alumina ceramics with unidirectionally aligned pore channels, which is a desirable feature for water filters (Fukasawa et al., 2001; Fukasawa et al., 2002; Deville, 2008).

We employed two alumina with different particle sizes to investigate the influence of the particle size on freeze casting processing and products as a filters for potable water.

7.2 Materials and methods

7.2.1 Raw materials and characterization

The powders used as raw materials for the filter were alumina (CT 3000, Almatis), with mean particle size of 0.5 and 2.5 μm, named respectively as F for fine, and C for coarse powder. They were characterized by measuring particle size distribution and zeta potential (Zetasizer, Nanosizer, Malvern; Stabino, Nanoflex, Particle Metrix), dispersion stability (Lumisizer, L.U.M.); as well as by TG/DSC (STA 449 F3 Jupiter, Netzsch); XRD (Desktop MiniFlex II, Rigaku); XRF (WDXRF Axios Max, Panalytical); picnometric density (Ultrapicnometer 1200 P/N, Quantachrome); specific surface area (BJH, Nova 1200e, Quantachrome); and SEM (TM3030, Hitachi).

7.2.2 Formulation, processing and characterization of filters

The forming of the samples was by freeze casting, where the velocity and the angle that the slurry was cast was maintained as constant as possible. The pores were controlled by changing the concentration of solids in the slurry. The compositions of the slurries are shown in Table 1, where C stands for coarse alumina (2.5 μm) and F for fine alumina (0.5 μm). All the samples have 1.5% organic dispersant (Darvan, C-N, Vanderbilt) and the balance is distilled water.

After freeze-casting, samples were kept in an ultra-freezer at -70 °C, during 24 h, and then transferred to a freeze-dryer (Liotop L102, Liobras) with pressure < 0.39 atm (300 μmHg) and temperature -50 °C, during 48 h. The freeze-dried samples were then sintered in an furnace (EDG-1600, EDG) at 1550 °C, with a heating rate of 5 °C/min, and dwell time of 2 h at the maximum temperature. The sintered filters were 20 ± 0.5 mm in diameter and 12 ± 1 mm thick.

Table 7. 1. Composition of coarse (C) and fine (F) alumina slurries.

Sample	**Alumina (wt%)**	**Darvan (wt%)**	**Water (wt%)**
C40	40	1.5	58.5
C50	50	1.5	48.5
C60	60	1.5	38.5
C70	70	1.5	28.5
F40	40	1.5	58.5
F50	50	1.5	48.5
F60	60	1.5	38.5
F70	70	1.5	28.5

Rheology measurements were performed with a viscometer (ViscotesterTM 550, Haake), with SV2P geometry of concentric cylinders with toothed surface. Each analysis was performed within 3 min at a shear rate of 0 to 600 s^{-1}, at room temperature. The viscosity values were adjusted according to the Herschel-Bulkley model (Equation 1) (Moreno, 2005).

$$\tau = \tau_0 + K\dot{\gamma}^n \quad (1)$$

where τ is the shear stress; τ_0, the yield stress; K, the consistency; $\dot{\gamma}$, the shear rate; and n, the flow index.

The average solidification rate of each sample could be obtained by measuring the height of the samples and controlling the time for complete solidification of the material. The final pellets had 20 ± 0.5 mm diameter and 12 ± 1 mm thickness. They were analyzed by SEM (TM3030, Hitachi).

For the tests of apparent specific gravity (relative density), water absorption and apparent porosity of the final filter, ASTM C20-00 standard was used. The mechanical strength was measured through compression tests in a universal machine (DL 20000, Emic) with a load cell of 20 N and a loading velocity of 0.5 mm/min, according to ASTM C133-97.

Permeability evaluation of the filters in air was based on Forchheimer's model (Equation 2 and auxiliary equations), an empirical relationship to express the parabolic dependence of pressure drop ($\Delta P_{(Pa)}$) through the medium with the resulting face velocity ($v_{s\,(m/s)}$):

$$\frac{\Delta P}{L} = \frac{\mu}{k_1} v_s + \frac{\rho}{k_2} {v_s}^2 \quad \text{Forchheimer's equation} \qquad (2)$$

$$\frac{\Delta P}{L} = \frac{\mu}{k_1} v_s \quad \text{Darcy's law}$$

$$\Delta P = \frac{{P_i}^2 - {P_o}^2}{2P_o} \quad \text{(for compressible flow)}$$

$$\frac{\Delta P}{L} = \frac{\Delta P_{viscous}}{L} + \frac{\Delta P_{inertial}}{L} \begin{cases} \Delta P_{viscous}(\%) = 100\left(\frac{1}{1+Fo}\right) \\ \Delta P_{inertial}(\%) = 100\left(\frac{Fo}{1+Fo}\right) \end{cases}$$

$$Fo = \frac{\rho v_s (k_1/k_2)}{\mu}$$

$$Eu = \frac{P_i - P_0}{\rho {v_s}^2}$$

Where ΔP is the pressure drop (Pa); Pi (Pa) and Po (Pa) are the absolute pressures at the bed entrance and exit, respectively. Pi is the reference pressure for the density and viscosity of the flowing fluid; L (m), the medium thickness; ρ (kg/m^3), density of the fluid; μ (Pa·s), the viscosity; v per unit of cross-sectional area of the flowing fluid is the volumetric flow rate; and k_1 (m^2) and k_2 (m) are the Darcyan and non-Darcyan permeability parameters, respectively. The dimensionless Forchheimer number (parameter) Fo represents the ratio between kinetic and viscous forces that contribute to fluid pressure drop. Since the ratio k_1/k_2 is expressed as length. (Innocentini et al., 1999; Moreira et al., 2004; Innocentini et al., 2010; Vakifahmetoglu et al., 2017). Table 2 shows the permeability test parameters.

Table 7. 2. Permeability test parameters.

Parameter (unit)	**Value**
T_{atm} (°C)	~ 25.0
P_{atm} (mmHg)	711
$\mu_{o,\ ar}$ (Pa·s)	1,88E-05
$\rho_{o,\ ar}$ (kg/m^3)	~ 1.09

7.3 Results and discussion

7.3.1 Raw materials characterization

Table 3 shows characteristic physical properties and chemical composition of alumina C and alumina F. Their particle size distributions, measured with Zetasizer, is shown in Figures 1 and 2, in which there are four measures (40, 50, 60 and 70 wt% of alumina in the initial suspension (respectively A, B, C and D). In all cases, there are more than

one peak, mainly in alumina C, showing agglomeration of the particles in the micrometric range.

Table 7. 3. Physical properties and chemical composition of alumina C and alumina F.

Physical Properties	**Alumina C**	**Alumina F**
Average particle size - Zetasizer (µm)	2.62	0.54
Average particle size - Lumisizer (µm)	2.28	0.48
Density (g/cm³)	3.89	3.83
S_{BET} (m^2/g)	2.28	5.79
Chemical composition (wt%)		
SiO_2	0.00	0.00
Al_2O_3	99.69	99.62
Fe_2O_3	0.04	0.02
CaO	0.05	0.02
Na_2O	0.02	0.02
K_2O	0.02	0.00
MnO	0.00	0.00
TiO_2	0.00	0.00
MgO	0.00	0.00
P_2O_5	0.00	0.00
Loss on Ignition	0.15	0.30

The density values are close to those reported by the manufacturers and found in the literature for alumina, approximately 3.91 g/cm³ (Figiel et al., 2011). Specific surfaces areas are close to the reported in the literature, in the range 2 to 6 m^2/g (El Hafiane et al., 2012). The chemical composition shows the high purity of the alumina powders.

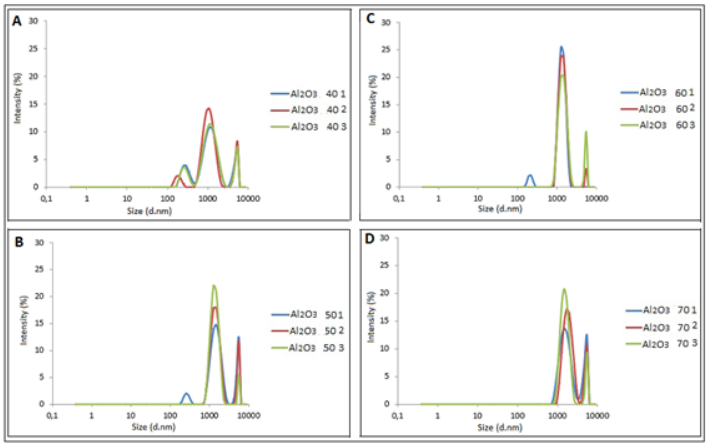

Figure 7. 1. Particle size distribution of alumina C, with 40, 50, 60 and 70 wt% alumina in the initial suspension (respectively A, B, C and D).

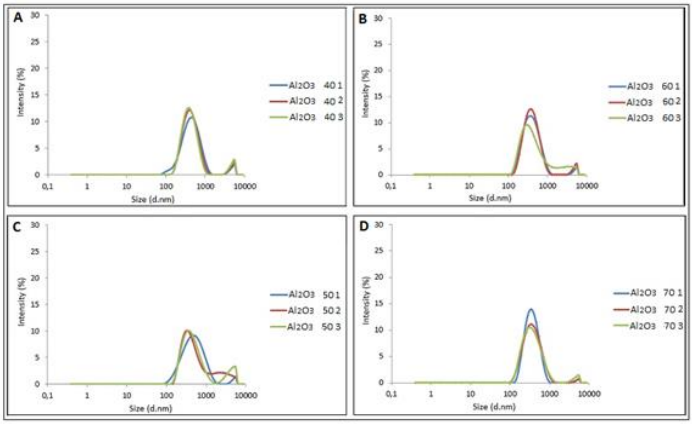

Figure 7. 2. Particle size distribution of alumina F, with 40, 50, 60 and 70 wt% solids in the initial suspension (respectively A, B, C and D).

The SEM micrographs of the alumina powders are in Figure 3 at different magnifications. It is possible to observe that the particle size of the coarse alumina C powder is ~2.5 μm with some larger particles ~6 μm, and the particle size of the fine alumina is ~0.5 μm with some larger particles ~4 μm. Those values are in good agreement with the analysis of particle size distribution by DLS. In Figures 3C and 3D, a larger agglomeration of the powder is observed due to its higher reactivity corresponding to smaller particle size and consequently larger surface area.

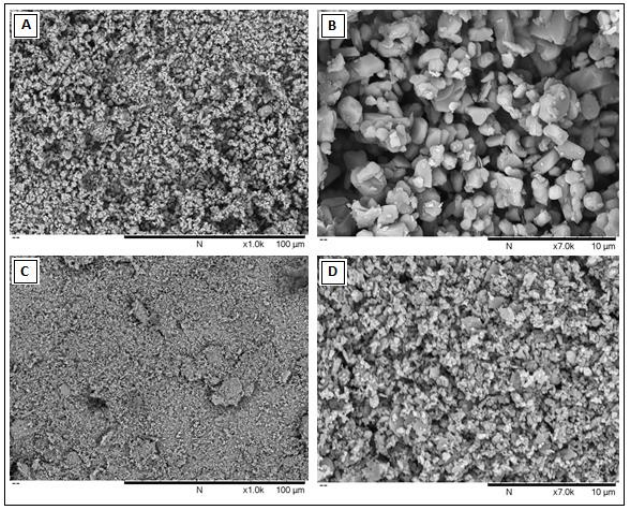

Figure 7. 3. SEM micrographs of the coarse alumina powder (A, B) and fine alumina powder (C, D) at different magnifications.

7.3.2 Rheological behavior of alumina suspensions

Figures 4 shows the curve of zeta potential versus pH of alumina C (4A) and alumina F (4B) suspensions. In case of alumina C, the zeta potential is around -77 mV (in acid pH) and -68 mV (in basic pH). The isoelectric point of the

suspensions can be observed in pH around 2.5, so that it is better to work with pH range 6-10, as far from pH 2.5 as possible, because the suspensions are more stable in these ranges. In alumina F, the zeta potential is around -38 mV (in acid pH) and -45 mV (in basic pH). The isoelectric point of the suspensions can be observed in pH around 3.5, it means that it is better to work with the same pH range that alumina C suspension. The initial suspensions were very stable, with pH 8.5 approximately.

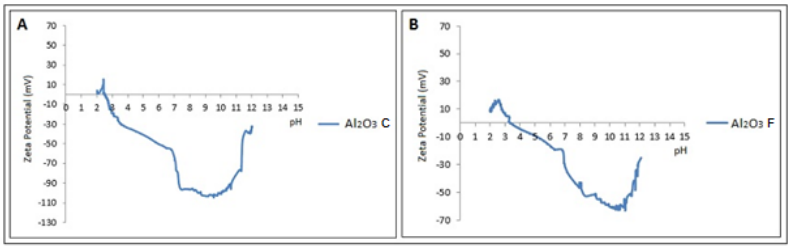

Figure 7. 4. Zeta potential versus pH of A) alumina C and B) alumina F suspensions.

In the rheological analysis, the flow data of the suspensions was fitted according to the Herschel-Bulkley (HB) model. The HB parameters, volumetric fraction of alumina, correlation coefficient (r) and viscosity at 300 s-1 (Ƞ300) of samples with 40, 50, 60 and 70 wt% alumina C and F are shown in Table 4.

Table 7. 4. Rheological parameters of coarse and fine alumina (C and F) suspensions, fitted according to the Herschel-Bulkley model.

Alumina sample	Solid load (%v)	τ_0 (s^{-1})	K	n	r	η_{300} (Pa·s)
C40	14.4	0.00	0.034	0.69	0.955	4.8
C50	20.2	0.00	0.073	0.66	0.961	5.2
C60	27.5	0.02	0.257	0.57	0.967	22.2
C70	37.1	1.20	4.925	0.30	0.996	96.5
F40	14.4	0.12	0.020	0.76	0.928	5.8
F50	20.2	0.03	0.010	0.87	0.972	4.8
F60	27.5	0.42	0.043	0.81	0.960	15.8
F70	37.1	2.90	0.036	1.04	0.884	54.7

The yield stress is around zero for lower solid loads, and the n index is less than the unit, indicating a pseudoplastic behavior as usually found for alumina suspensions in water, although the correlation coefficient r is not that high. For both coarse and fine alumina suspensions, the viscosity is higher when the amount of solids is increasing, as expected. Slurries with 50 wt% solids, the percentage chosen for the next steps, considering average deviation, have about the same viscosity for both alumina C and F suspensions.

The rheograms of alumina C (Figure 5) and F (Figure 6), showing viscosity (Pa·s) versus shear rate (s^{-1}) and shear stress (Pa) versus shear rate (s^{-1}) for 40, 50, 60 and 70 wt% attest that the behavior is similar in all the compositions, and the values are almost the same, with exception of samples with 70 wt% solids.

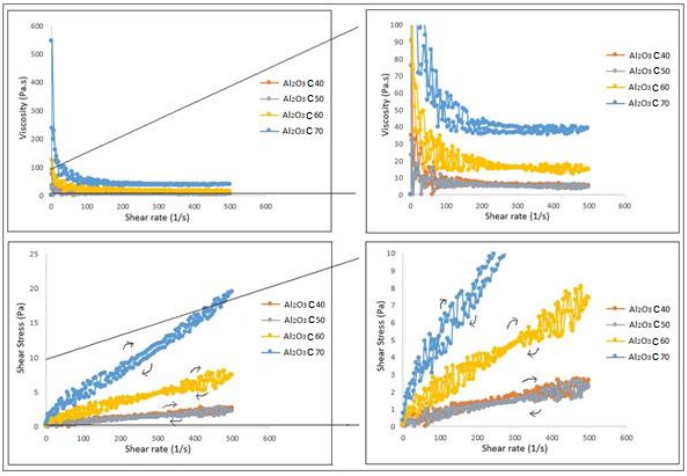

Figure 7. 5. Curves of viscosity (Pa·s) versus shear rate (s^{-1}) and shear stress (Pa) versus shear rate (s^{-1}) for 40, 50, 60 and 70 wt% alumina C suspensions.

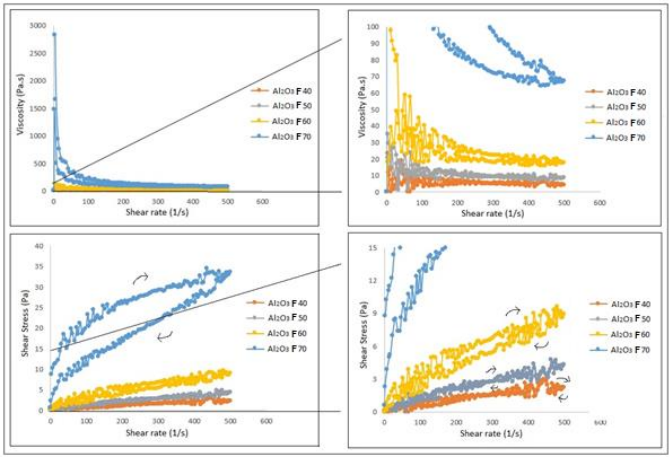

Figure 7. 6. Curves of viscosity (Pa·s) versus shear rate (s^{-1}) and shear stress (Pa) versus shear rate (s^{-1}) for 40, 50, 60 and 70 wt% alumina F suspensions.

7.3.3 Porosity and permeability of filters

The solidification rate is one of the parameters that most interferes in the pore size, Figure 7 shows the average solidification rate found, during the freeze casting process, for alumina samples containing 50 wt% and 50 wt% coarse and fine powder, respectively. The variation in sample height is due to the difficulty of accurately controlling the volume of suspension cast into the mold.

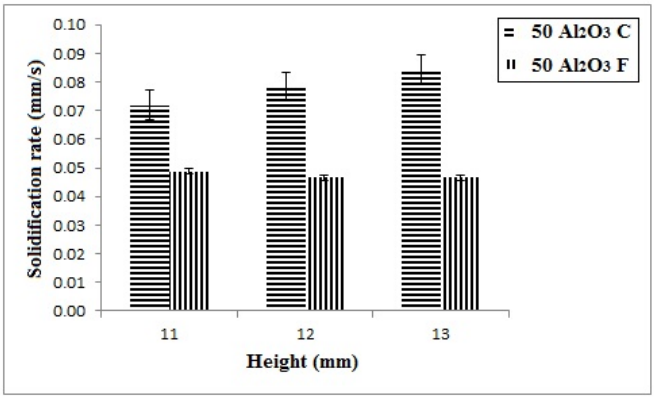

Figure 7. 7. Average solidification rate found for alumina samples containing 50 wt% coarse (C) and fine (F) fine powder, respectively.

The difference in the solidification rate is due to the difference in particle size between alumina C (2.5 μm) and F (0.5 μm). As the particle size decreases, the solidification rate also decreases. At a high freezing rate, ice nucleation is kinetically more favorable than crystal growth, small pore formation is more likely. Moreover, the dispersing state of the suspension is more likely to be maintained at a high freezing rate since there is less time for particles to rearrange. Lower freezing rate offers more densely packed particles and lower porosity (Li et al., 2012).Since alumina C has a higher solidification rate, the stability of their slurries is higher.

Figure 8 shows the appearance of the sintered filter samples.

Figure 7. 8. Appearance of the sintered filter samples.

Figure 9 shows the SEM micrographs in samples with 50 wt% solids, of the external surface of alumina C50 (Figure 9A) and alumina F50 (Figure 9B), and of the fractured inner surface C50 (Figure 9C) and F50 (Figure 9D).

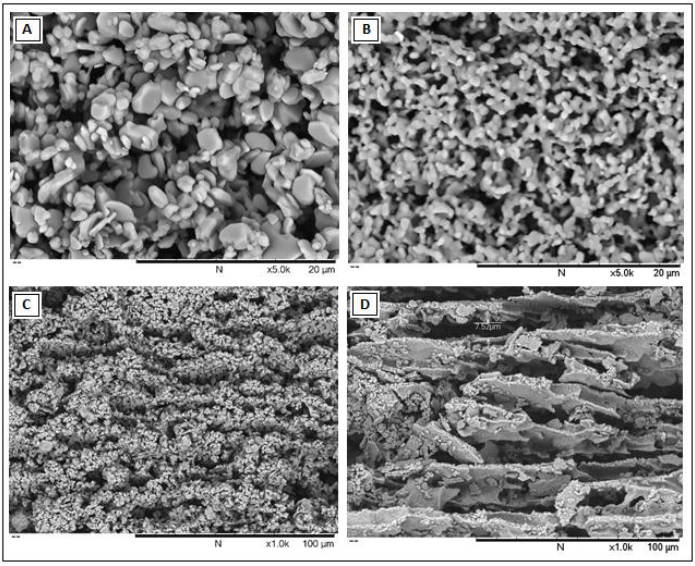

Figure 7. 9. SEM micrographs of the external surface of sintered alumina samples A) C50 and B) F50, and of the fractured inner surface of samples C) C50 and D) F50.

A difference in the distribution and shape of the pores and their connectivity can be observed. The pore size in the sintered samples, both at the external surface and the fractured inner surface, varies remarkably. Roughly, pores are ~3 µm for sample C50 and ~7 µm for sample F50. For the intended application, it is desirable to have pores with 3 µm or less. Through the fractured inner surface micrograph, it is possible to observe the high alignment of pores due to the freeze casting. In the sample C50, a more homogeneous structure with better densification is observed, while in the sample F50, a less homogeneous structure with the formation of layers can be seen.

Table 7. 5. Physical and mechanical properties of filters of coarse and fine alumina (C and F) with solids loads of 40 to 70 wt%.

Alumina sample	Solids load (wt%)	Open pores volume (m^3)	Apparent Porosity (%)	Water absorption (%)	Density (g/cm^3)	Compressive strength (MPa)
C40	40	3.0×10^{-6}	55.5	31.8	3.9	8.6 ± 0.8
C50	50	3.8×10^{-6}	73.1	69.9	3.9	8.9 ± 0.2
C60	60	2.1×10^{-6}	61.8	45.7	3.9	0.5 ± 0.4
C70	70	3.2×10^{-6}	67.1	51.4	3.9	1.9 ± 0.5
F40	40	2.4×10^{-6}	80.1	102.5	3.9	2.8 ± 0.3
F50	50	2.9×10^{-6}	67.9	53.7	3.9	11.7 ± 0.5
F60	60	2.2×10^{-6}	55.6	32.6	3.8	24.8 ± 3.2
F70	70	1.3×10^{-6}	35.8	14.4	3.9	35.8 ± 2.8

Table 5 and Figure 10 show the apparent porosity versus total solids (wt%) of alumina C and F samples. Alumina F shows a decreasing curve behavior: the higher the amount of solids, the lower the porosity; while alumina C does not show any decreasing trend. At around 50 wt%, which is approximately the percentage chosen for the pellets of this work based on experimental results, the porosity of alumina C is slightly higher than that of alumina F, around 73 and 68%, respectively.

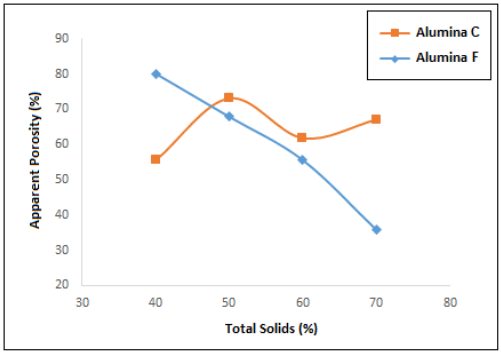

Figure 7. 10. Apparent porosity versus total solids load (wt%) of the alumina C and F samples.

Figure 11 and Table 5 show the relationship between porosity and compressive strength of samples of coarse and fine alumina with 40, 50, 60 and 70 wt% solids. The mechanical strength of alumina F reached higher values, corresponding to a very low porosity (in samples with higher solids percentages); alumina C maintained a lower range of compressive strength, and porosity remained higher in all solids percentages. For the filters, a balance of good mechanical strength and high porosity must be found.

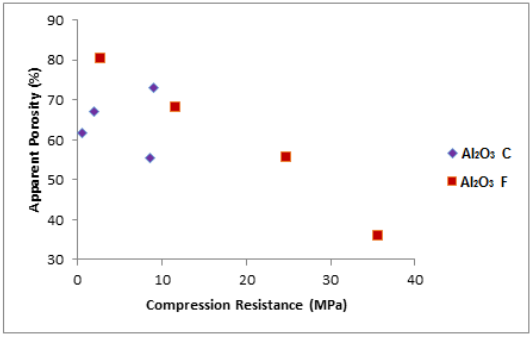

Figure 7. 11. Apparent porosity versus compressive strength of coarse and fine alumina (C and F) samples.

Table 6 shows values of k_1 and k_2, Darcyan and non-Darcyan permeability parameters respectively, of samples with coarse and fine alumina, with 40 to 70 wt% solids.

Table 7. 6. Darcyan and non-Darcyan permeability parameters, k_1 and k_2, of coarse and fine alumina samples, respectively, C and F, with 40 to 70 wt% solids.

Alumina sample	**Total solids (wt%)**	**k_1 (m^2)**	**k_2 (m)**
C40	40	5.1×10^{-13}	3.1×10^{-7}
C50	50	1.3×10^{-13}	2.0×10^{-7}
C60	60	4.2×10^{-13}	1.9×10^{-7}
C70	70	2.2×10^{-13}	2.5×10^{-7}
F40	40	1.5×10^{-12}	3.9×10^{-7}
F50	50	1.4×10^{-12}	3.0×10^{-7}
F60	60	6.1×10^{-13}	1.7×10^{-7}
F70	70	1.7×10^{-13}	1.3×10^{-8}

Figure 12 shows permeability parameters, k_1 or k_2 versus apparent porosity, respectively, of samples with coarse and fine alumina with 40 to 70 wt% solids.

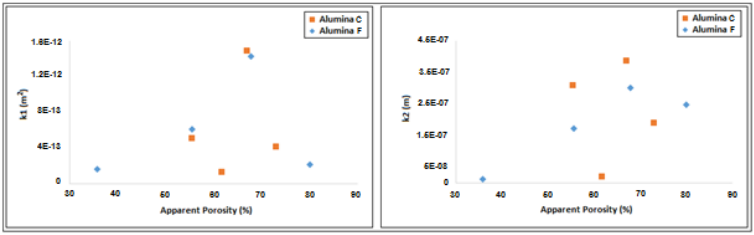

Figure 7. 12. Curves of k_1 (m^2) versus apparent porosity and k_2 (m), respectively, versus apparent porosity of samples with coarse and fine alumina with 40 to 70 wt% solids.

The Darcyan and non-Darcyan permeability parameters do not show a direct relationship with the apparent porosity in samples with coarse or fine alumina; the second ones present an increasing linear behavior in samples with apparent porosity between around 35 and 70%, though. The data obtained in this work were inserted in a data map with data available in the literature (Figure 13) (Vakifahmetoglu et al., 2017).

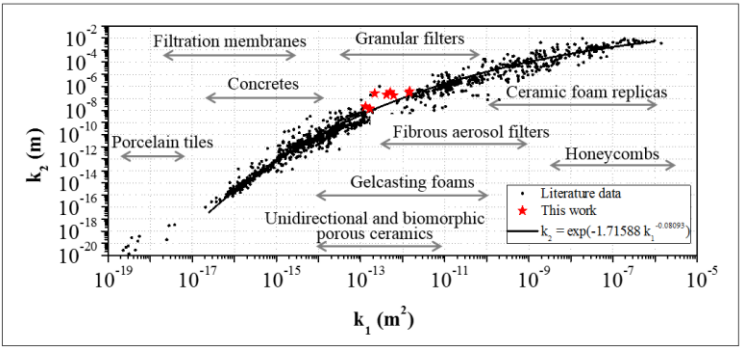

Figure 7. 13. Location of permeability data of obtained in this work in a comprehensive data map available in the literature (Vakifahmetoglu et al., 2017).

The values of k_1 and k_2, obtained in this work were in the range of granular filters (ceramic filters able to water purification) and fibrous aerosol filters (ceramic filters useful to allow savings in thermal energy with simultaneous removal of particulate material and chemical contaminants from flue gases) (Innocentini et al., 2009). In this way, desired permeability values were obtained here for the application as drinking water filters.

7.4 Conclusions

As the particle size decreases, the solidification rate also decreases, so the solidification rate is lower for fine alumina, and lower freezing rate offers more densely packed

particles and lower porosity. Since alumina C has a higher solidification rate, the stability of their slurries is higher, since there is less time for particles to rearrange.

The average pore size is ~3 μm for sample C50 (more suitable for the intended application) and up to 7 μm for sample F50. In the sample C50, a more homogeneous structure with better densification is observed, at around 50 wt% solids. The porosity of coarse alumina is slightly higher than that of fine alumina, between 73 and 68% respectively.

The compressive strength of fine alumina reached higher values, but with a very low porosity (particularly in samples with higher solids loading). Coarse alumina presented a lower mechanical strength, and the porosity remained higher in all solids concentrations.

Considering permeability parameters k_1 and k_2 obtained in this work, the ceramic filters achieved the desired permeability values for the application of filters for drinking water, regardless of the alumina particle size.

According to the experimental data, coarse alumina is more suitable for this application, so it was chosen to be used in the next steps of this work.

8 Fabrication of freeze-cast porous alumina/kaolinite filters for water purification[4]

8.1 Introduction

Porous ceramics is a field of intense research for their wide applications as catalyst carriers, ceramic filters, sensors, porous electrodes, biomaterials, and thermal barriers. Various fabrication methods of porous ceramics have been employed, including different pore-foaming techniques, infiltration of ceramic sol into template structures, gel-casting, slip-casting, starch consolidation, microwave processing, electrophoretic deposition, and freeze casting (Deville, 2008; Hu et al., 2010).

A comparative study of thirty-seven different water treatments indicate that porous ceramic water filters are among the five most effective treatments for turbidity reduction and a 99% reduction of bacteria (Lantagne, 2001; Clasen and Boisson, 2006; Simonis and Basson, 2011).

Among many emerging techniques, freeze casting is an attractive shaping method for the fabrication of highly porous and hierarchically organized ceramic structures. (Zhang et al., 2015; Gaudillere and Serra, 2016).

Freeze casting has received broad attention as a simple and versatile fabrication technique of porous structures, which generally offers a wider range of pore characteristics compared to other conventional fabrication methods such as foam or wood replication, direct foaming, gel casting and others. Water and camphene are common solvents in freeze-casting process (Deville et al., 2007; Fukushima et al., 2008; Yoon et al., 2008; Li and Li, 2012).

The technique consists of freezing a ceramic slurry, followed by sublimation of the solvent by freeze drying at both low pressure and temperature, and subsequent sintering,

[4] Submitted.

leading to a porous structure with unidirectional channels, where pores are a replica of the solvent crystals (Deville, 2008; Gaudillere and Serra, 2016).

The control of pore structure is very important because of its relation to properties. Many factors, including the composition and solid loading of slurry as well as sintering conditions, influence the microstructure and properties of porous ceramics fabricated by the freeze casting (Hu et al., 2010).

In this work, filters composed of alumina and kaolinite were obtained by freeze casting for water filtration.

8.2 Materials and methods

8.2.1 Raw materials and characterization

The powders used as raw material for the porous filters were kaolinite (Colorminas) and alumina (UC, CT 3000, Almatis). They were characterized by measuring particle size distribution (Nanosizer, Malvern; Lumisizer, LUM); zeta potential (Stabino, Particle Metrix); TG/DSC (STA 449 F3 Jupiter, Netzsch); XRD (MiniFlex II, Rigaku); XRF (WDXRF Axios Max, Panalytical); picnometric density (Ultrapicnometer 1200 P/N, Quantachrome); and specific surface area (BJH, Nova 1200e, Quantachrome).

8.2.2 Formulation, shaping and sintering

The compositions of the slurries are shown in Table 1. To all the samples 1.5 wt% organic dispersant (Darvan, C-N, Vanderbilt) was added, and the balance is distilled water.

Table 8. 1. Compositions of the alumina/kaolinite slurries.

Sample	Total solids (wt%)	Alumina C (wt%)	Kaolinite (wt%)
A15K25	40	15	25
A20K30	50	20	30
A30K20	50	30	20
A50	50	50	-
A30K25	55	30	25
A30K30	60	30	30
A35K25	60	35	25
A60	60	60	-
A40K25	65	40	25
A40K30	70	40	30

The shaping of filters was performed by freeze casting, and the porosity was adjusted by changing the concentration of solids in the slurry. Before freeze casting, the slurries were mixed in a ball mill during 12 h. Filter samples of 20 ± 1 mm diameter, 12 ± 2 mm thickness were produced. Figure 1 shows a schematic representation of the so-called "cold finger" equipment used in the freeze-casting technique.

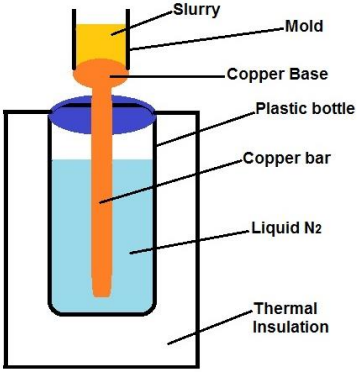

Figure 8. 1. A schematic of the freeze-casting apparatus used in this work.

The velocity and the angle that the slurry was cast was maintained as constant as possible. After freeze-casting, samples were kept in an ultra-freezer at -70 °C, during 24 h, and then transferred to a freeze-dryer (Liotop L102, Liobras) with pressure < 0.39 atm (300 μmHg) and temperature -50 °C, during 48 h.

The freeze-dried samples were then sintered in an furnace (EDG-1600, EDG) at 1550 °C, with a heating rate of 5 °C/min, and dwell time of 2 h at the maximum temperature. The sintered filters were 20 ± 0.5 mm in diameter and 12 ± 1 mm thick.

8.2.3 Characterization of sintered filters

For the tests of water absorption, apparent specific gravity (relative density) and apparent porosity of the final filter, ASTM C20-00 standard was used. The mechanical strength was measured through compression strength, in the instrument DL 20000, Emic, with a load cell of 20 N and a loading velocity of 0.5 mm/min. ASTM C133-97 standard was used. The sintered samples were analyzed by SEM (TM3030, Hitachi).

Permeability evaluation was based on Forchheimer's equation, an empirical relationship well accepted in the literature to express the parabolic dependence of pressure drop through the medium with the resulting superficial or face velocity. The Darcyan and non-Darcyan permeability parameters (Innocentini et al., 1999; Moreira et al., 2004; Innocentini et al., 2010; Vakifahmetoglu et al., 2017) were estimated.

Filter efficiency was analysed as well (Colilert and Quanti-Tray/2000, Idexx). To conduct filter efficiency and turbidity tests, some very dirty and contaminated water samples were collected in bottles decontaminated by an autoclave (Vertical, Phoenix). This water samples was analyzed before and after passing through the filter.

Colilert tests simultaneously detect total coliforms and E. coli in water, based on Idexx's patented Defined Substrate Technology (DST). When total coliforms metabolize Colilert's nutrient-indicator, ONPG, the sample turns yellow. When E. coli metabolize Colilert's nutrient-indicator, MUG, the sample also fluoresces.

Firstly, the content of one pack of Colilert was added to a 100 mL water sample in a sterile bottle and shaken until being dissolved. Then, the sample/reagent mixture was set into a tray, sealed in an sealer (Quanti-Tray Sealer, 2X, Idexx), and placed in 35°C ± 0.5°C incubator for 24 h.

After that, results have been read counting the number of positive wells (yellow wells = total coliforms, yellow/fluorescent wells = E. coli) and refer to the MPN table provided with the trays to obtain a most probable number. The fluorescence was read with a 6-watt, 365-nm UV light within ~13 cm of the sample in a dark environment.

If the appearance result less yellow than the reference, it is negative for total coliforms and E. coli; when it is yellow comparably to or more intense than the reference, it is positive

for total coliforms; and when it is yellow and fluorescence just like or more than the reference, it is positive for E. coli. Figure 2 shows as an example one tray negative for total coliforms and E. coli, and other positive for total coliforms, respectively.

(a) (b)

Figure 8. 2. Filter efficiency test: (a) tray negative for total coliforms and E. coli, and (b) tray positive for total coliforms.

Turbidity is the cloudiness in water caused by particles in suspension, which makes chemical disinfection of the water less effective. It is commonly measured in nephelometric turbidity units (NTU) (WHO, 2008; WHO, 2017b). The turbidity of the dirty (contaminated) and clean (after filter) water were measured (Turbidimeter, 2100N, Hach) with distilled and tap water to compare the results.

8.3 Results and discussion

8.3.1 Characterization of powders and suspensions

Table 2 and Figure 3 show characteristic physical properties and chemical composition of the kaolinite and alumina. Some agglomeration of the particles in the micrometric range can be seen, mainly with alumina that presents more than one peak.

Table 8. 2. Physical properties and chemical composition of kaolinite and alumina powders.

Physical Properties	**Kaolinite**	**Alumina**
Average particle size - Zetasizer (µm)	2.18	2.62
Average particle size - Lumisizer (µm)	2.16	2.28
Density (g/cm³)	2.71	3.89
S_{BJH} (m^2/g)	13.23	6.80
Chemical composition (wt%)		
SiO_2	46.93	0.00
Al_2O_3	37.92	99.69
Fe_2O_3	0.40	0.04
CaO	0.00	0.05
Na_2O	0.25	0.02
K_2O	0.94	0.02
MnO	0.00	0.00
TiO_2	0.00	0.00
MgO	0.24	0.00
P_2O_5	0.00	0.00
Loss on Ignition	13.14	0.15

The density values are close to those reported by the manufacturers, which are respectively 3.91 g/cm³ for alumina and 2.65 g/cm³ for kaolinite (Figiel et al., 2011; Horpibulsuk et al., 2011).

The chemical composition shows the high purity of the alumina powder and kaolinite powders, which presented very close weight percent values when compared to the theoretical ones: 46.55% SiO_2; 39.50% Al_2O_3 and 13.96% H_2O (Moreira et al., 2004; Barg et al., 2011).

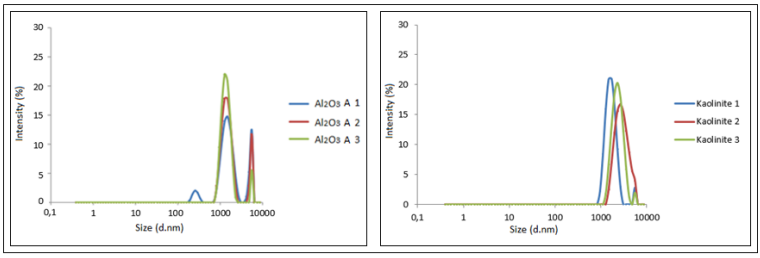

(a) (b)

Figure 8. 3. Particle size distribution of powders: (a) alumina and (b) kaolinite.

Figures 4 shows the curve of zeta potential versus pH of kaolinite and alumina suspensions. In case of kaolinite, the zeta potential is around -72 mV (in acid pH) and -53 mV (in basic pH). The isoelectric point of the suspensions can be observed in pH around 2; it means that it is advisable to work with pH range 6-10, as far from pH 2 as possible, because the suspensions are more stable in these ranges. For alumina, the zeta potential is around -77 mV (in acid pH) and -68 mV (in basic pH). The isoelectric point of the suspensions can be observed in pH around 2.5. Thus, the same pH range that kaolinite suspension is adequate for alumina as well. The suspensions at natural pH, around 8.5, were very stable.

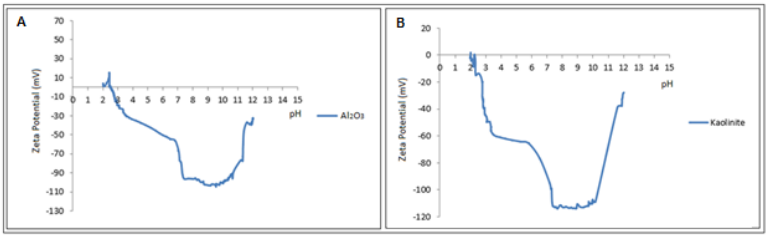

Figure 8. 4. Zeta potential versus pH of suspensions: (a) alumina and (b) kaolinite.

The thermogravimetric behavior of alumina and kaolinite is presented in Figure 5A. Kaolinite has a mass loss around 500 °C due to the loss of constitutional water (Albuquerque et al., 2007; Araújo et al., 2012). These transformations are shown in DSC curves (Figure 5B), corresponding to endothermic curves that are related to the evaporation of water.

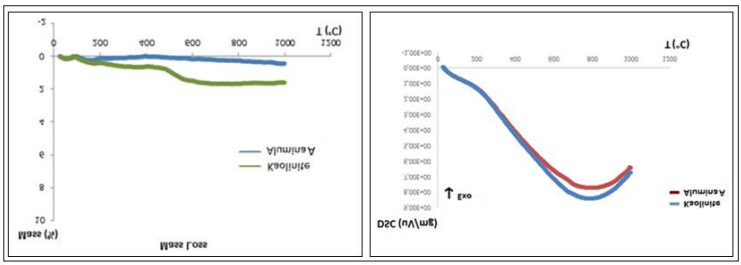

(a) (b)

Figure 8. 5. Thermal analyses of alumina and kaolinite: (a) TG (mass loss) and (b) DSC.

The diffractograms of alumina and kaolinite, identified with Crystallography Open Database (COD) are shown in Figure 6. For alumina samples, all the peaks refer to the presence of crystalline phase of the rhombohedral type (α-

alumina or corundum, code 96-900-8095), and absence of amorphous phase. The diffractogram of kaolinite as well as that of alumina refers only to the presence of crystalline phase of monoclinic type (96-154-4873) and absence of amorphous phases.

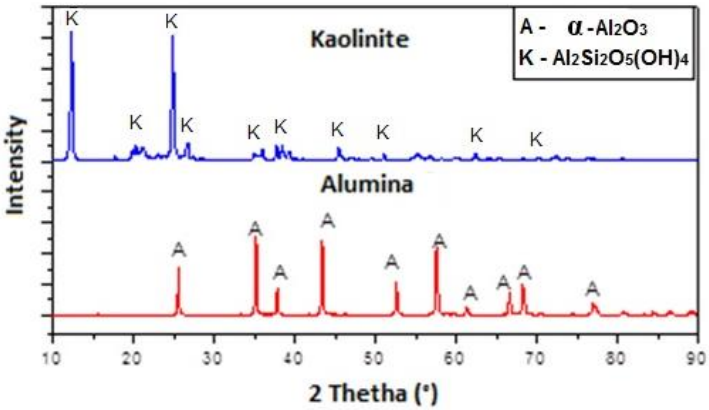

Figure 8. 6. Powder diffractograms of alumina (A for alpha phase) and kaolinite (K), identified with Crystallography Open Database (COD).

8.3.2 Characterization of sintered samples

Table 3 shows the mean and dispersion values of apparent porosity (%), water absorption (%), density and compressive strength (MPa) of 10 alumina/kaolinite sintered samples.

Table 8. 3. Mean and standard deviation (SD) of apparent porosity, water absorption, density and mechanical strength of alumina/kaolinite samples.

Sample	Apparent porosity (%)		Water absorption (%)		Density		Compressive strength (MPa)	
	Mean	SD	Mean	SD	Mean	SD	Mean	SD
A15K25	73.5	1.1	90.7	5.1	3063.9	0.0	12.2	1.3
A20K30	69.8	2.4	73.8	6.3	3134.5	0.1	13.9	2.1
A30K20	64.3	0.4	56.1	1.4	3217.8	0.0	14.3	1.5
A50	70.9	4.1	63.4	8.4	3190.8	0.0	8.9	2.7
A30K25	67.1	0.1	62.1	0.1	3132.9	0.0	16.7	3.3
A30K30	63.7	0.3	54.9	0.6	3090.1	0.0	31.4	1.8
A35K25	64.6	0.1	56.1	0.5	3125.1	0.0	29.8	1.1
A60	57.1	4.7	34.5	5.6	3215.2	0.0	0.5	0.4
A40K25	57.6	0.4	40.9	0.7	3614.3	0.0	22.1	1.9
A40K30	54.1	0.1	35.4	0.1	3962.1	0.0	21.3	1.1

There is a decrease in the value of both apparent porosity and water absorption, as the solids content increases. This is because these phenomena are interconnected. It is possible to observe that there is no tendency to increase or decrease the density of the samples as the solids content increase, this was not expected because the relative density is the ratio of bulk density of the sample to the theoretical density of the material, and the bulk density is the ratio of the sample mass to its total external volume. The theoretical density is usually fixed, but increasing the amount of solids (with higher density), would increase the mass of the sample, consequently increase the relative density, but it must be considered that the samples have different compositions of solids, which directly affect the values of theoretical and relative densities.

Figure 7 shows the relationship of porosity and compressive strength of samples with only alumina and alumina/kaolinite mixtures. In this case, the mechanical strength is not directly proportional with the apparent porosity. For example, samples with the lowest and higher values of compression strength present both around 60% apparent porosity. This occurs because of different samples compositions.

For the filters, a very high mechanical strength is not necessary, but a high porosity is essential. Considering this, the samples with 40 wt% solids (A15K25) and 50 wt% solids (A50 and A30K20) have suitable values of compression strength and apparent porosity.

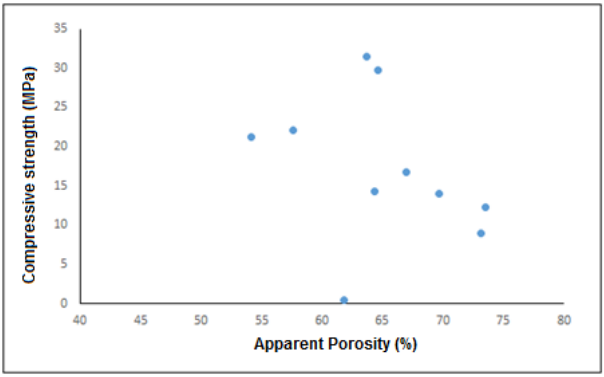

Figure 8. 7. Porosity versus compressive strength of alumina and alumina/kaolinite samples.

Figure 8 shows the relationship of the percentage of the components (alumina and kaolinite) and the compressive strength.

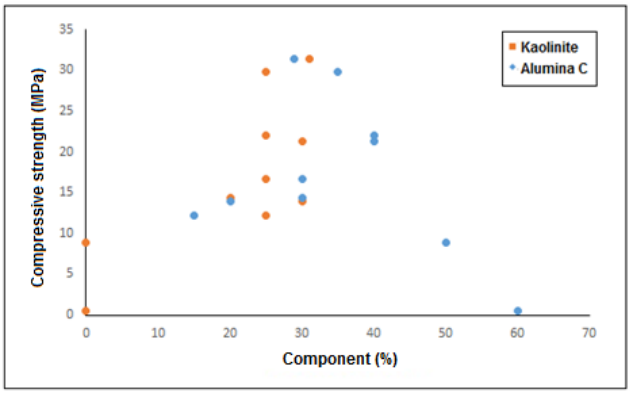

Figure 8. 8. Effect of the composition (alumina and kaolinite) on the compressive strength.

Samples with around 70 wt% of total solids have high values of compression strength, due to a larger alumina densification that occurs during sintering, but they are not suitable for this application because their permeability/flow rate is very less than the necessary for ceramic filters. Samples with alumina and kaolinite with similar percentage (around 50 wt% of total solids) presented the best results of compression strength.

8.3.3 Porosity and permeability of filters

Considering this and other experimental data, samples with suitable values of apparent porosity and compression strength were chosen for the tests of permeability, A15K25 and A30K20. Table 4 shows values of k_1 (m2) and k_2 (m), Darcyan and non-Darcyan permeability parameters respectively, of samples A15K25 and A30K20, comparing them with previously results of coarse and fine alumina (C and F) with the same percentage of total solids (40 and 50 wt%).

Table 8. 4. Values of permeability of samples A15K25 and A30K20, comparing them with previous results with coarse (C) and fine (F) alumina with the same percentage of total solids (40 e 50 wt%).

Sample	**Total Solids (wt%)**	**k_1 (m^2)**	**k_2 (m)**
C40	40	5.1×10^{-13}	3.1×10^{-07}
F40	40	1.5×10^{-12}	3.9×10^{-07}
A15K25	40	8.1×10^{-13}	6.3×10^{-07}
C50	50	1.3×10^{-13}	2.0×10^{-07}
F50	50	1.4×10^{-12}	3.0×10^{-07}
A30K20	50	6.6×10^{-13}	3.9×10^{-07}

Figure 9 shows permeability parameters, k_1 (m^2) versus apparent porosity and k_2 (m) versus apparent porosity respectively, of samples with coarse and fine alumina (C, F) and alumina/kaolinite (A/K) with 40 and 50 wt%.

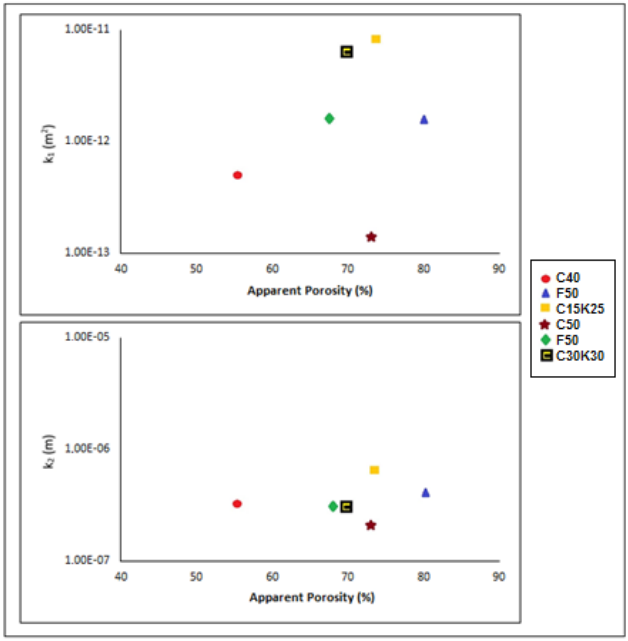

Figure 8. 9. Permeability parameters, k_1 (m^2) and k_2 (m) versus apparent porosity respectively, of samples with alumina (coarse, fine) and kaolinite, with 40 and 50 wt% solids.

The Darcyan and non-Darcyan permeability parameters respectively do not present a direct relationship with the apparent porosity. Samples A50 and A15K24, for example, have a similar value of apparent porosity (around 73%) and they have the lowest and the highest values, respectively, in both parameters (k_1 and k_2).

Samples with the higher values of k_1 and k_2 were samples with alumina and kaolinite mixtures (A15K24 and A30K20), and their values of apparent porosity are suitable for the application aimed in this work. They have been inserted in a data map with data available in the literature (Figure 10) (Vakifahmetoglu et al., 2017).

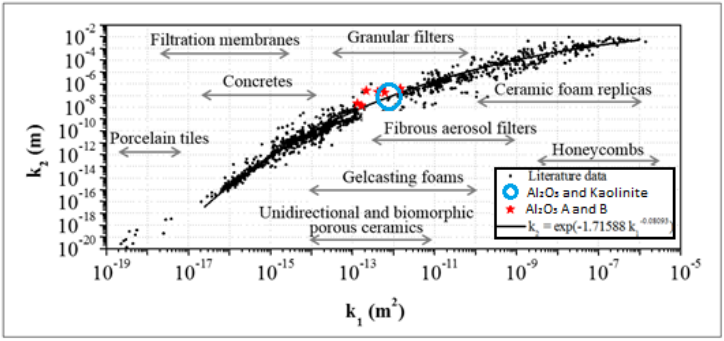

Figure 8. 10. Location of permeability data of samples of alumina/kaolinite mixtures obtained in this work in a data map (Vakifahmetoglu et al., 2017).

The values of k_1 and k_2, obtained in this work, were between values in data of granular filters (ceramic filters able to water purification) and fibrous aerosol filters (ceramic filters useful to allow savings in thermal energy with simultaneous removal of particulate material and chemical contaminants from flue gases) (Innocentini et al., 2009). Thus, the samples achieved the desired permeability values for drinking water filtration.

Considering all the experimental data, sample A30K20, with 50 wt% solids (alumina 30 wt% and kaolinite 20 wt%) was chosen to be used in the next steps of this work.

Figure 11 shows SEM micrographs of sample A30K20 at the external surface (and at the fractured inner surface, with different magnifications.

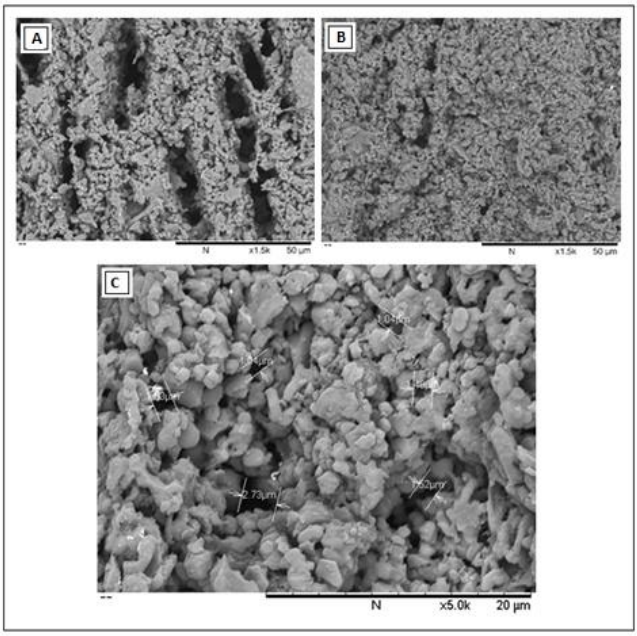

Figure 8. 11. SEM micrographs of sample A30K20: A) external surface; B) fractured inner surface and C) the fractured inner surface with measurement of the pores indicated.

In the micrograph of the external surface, it is possible to observe a strong characteristic of the freeze-casting process, the pores are aligned and directed, with homogeneous distribution. In the fractured inner surface, there is a homogeneous distribution of pores too, and the average size of pores measured in this micrograph is 1.55 µm. Comparing these pore sizes with the literature, they are suitable for water filtration (Lantagne, 2001; Yakub et al., 2012; Youmoue et al., 2017).

According to the application map of porosity versus pore or channel size (Figure 12), the sample A30K20, considering porosity and pore size, is within the range of "purification and filtration" (Vakifahmetoglu et al., 2017).

8.3.4 Filter biocide efficiency

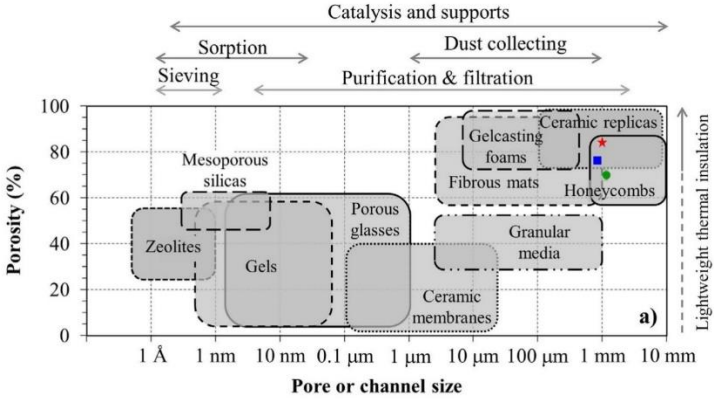

Figure 8. 12. Application map of porosity versus pore or channel size (Vakifahmetoglu et al., 2017).

Table 5 shows the results of filter efficiency according to the MPN table provided with the trays to obtain a most probable number of total coliforms and E. coli, after counting yellows and fluorescent wells.

Table 8. 5. Results of filter biocide efficiency according to the MPN table provided with a most probable number of total coliforms and E. coli.

	Positive Wells				**Total Coliforms**	**E. Coli**
Water analyzed (100 mL)	**Yellow Large**	**Yellow Small**	**Yellow/ Fluorescent Large**	**Yellow/ Fluorescent Small**	**Most Probable Number**	**Most Probable Number**
Dirty/ Contaminated	49	48	49	48	>2419.6	>2419.6
Clean/ After filter	21	38	17	33	77.9	63.5

According to the CONAMA Resolution 396/2008, Table 6 shows the list of parameters with the highest probability of occurrence in groundwater, their respective Maximum Allowed Values (MAV) for each of the uses considered as preponderant and the Practicable Quantification Limits (PQL), considered as acceptable for the application of this Resolution.

Table 8. 6. Amount of E. coli and Thermotolerant Coliforms allowed in groundwater. Adapted from CONAMA, 2008.

Type	**MAV (µg/L)**			**PQL (µg/L)**
	Human consumption	**Animal Consumption**	**Recreation**	
Microorganisms				
E. coli	Absent in 100 mL	200/100 mL	800/100 mL	-
Thermotolerant Coliforms	Absent in 100 mL	200/100 mL	1000/100 mL	-

Considering this, the water passed through the filter pellets was not suitable for the human consumption, but it is acceptable for the animal consumption and for recreation. The most probable numbers of total coliforms and E. coli had a large decrease after the filtration, reaching less than a half of the value allowed for animal consumption and less than an eighth of the value allowed for recreation.

Turbidity can be caused by silt, sand and mud; bacteria and other germs; chemical precipitates (WHO, 2008). Achieving low turbidities in drinking-water is a proven indicator of pathogen removal and hence of drinking-water safety. Incidents of elevated turbidity have been associated with several outbreaks of disease (WHO, 2017a; Mann et al., 2007).

Mihelcic et al. (2009) stated that turbidity has a negative impact on many water treatment processes in

different ways, including clogging filters and therefore reducing their effectiveness. They also concluded that turbidity is easily measurable in the field with the use of a turbidity tube, and that the pretreatment turbidity limit for ceramic filters is between 15 NTU and 20 NTU. (Mihelcic et al. 2009; Salvinelli et al., 2016).

The dirty/contaminated sample for the test of filter efficiency and turbidity was collected from a stream at UFSC. Its turbidity was 17.41 ± 2.42 NTU, in the range of the pretreatment turbidity limit for ceramic filters. Figure 13 shows the turbidity of the water before (dirty/contaminated) (13A) and then of passing through the filter pellet (clean) (13B).

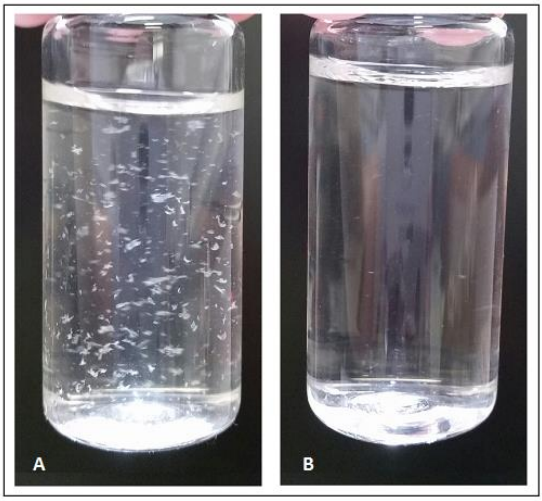

Figure 8. 13. Turbidity of the water, A) before (dirty/contaminated) and B) then of passing through the filter pellet (clean).

Table 7 shows the results of turbidity of the dirty (contaminated), clean (after filter) water, tap water and distilled water.

Table 8. 7. Turbidity of the dirty (contaminated), clean (after filter) water, tap water and distilled water.

Sample	Turbidity (NTU)
Distilled Water	0.34 ± 0.23
Tap Water	1.97 ± 0.81
Dirty/ Contaminated	17.41 ± 2.42
Clean/ After filter	0.56 ± 0.31

Effective disinfection requires the water to have a low turbidity. Ideally, median turbidity should be below 1 nephelometric turbidity unit (NTU) (WHO, 1997). However, 5 NTU is the minimum turbidity measurable with simple equipment (turbidity tube), so this level may be used in practice. If turbidity exceeds 5 NTU, then the water should be treated to remove suspended matter before disinfection (WHO, 2017b). Most of papers/guidelines affirms that drinking water should have a turbidity of 5 NTU or less (Brazilian Health Ministry, 2004; CONAMA, 2008; WHO, 2008; WHO, 2017b).

Considering this, our sample, after pass through the filter, has a turbidity of 0.56 ± 0.31 NTU, below the value allowed, below even the turbidity of tap water and close to the turbidity of distilled water. Attesting the efficiency of our filter considering the turbidity parameter.

8.4 Conclusions

Samples with only alumina C have high values of compression strength, but low values of permeability/flow rate. Samples with alumina C and kaolinite with around

50wt% of total solids have best results of compression strength with acceptable value of permeability/flow rate.

The higher values of k_1 and k_2 were of samples with alumina and kaolinite, with suitable values of apparent porosity and a homogeneous distribution of pores, with average pore size of 1.55 μm, with pores between 1.04 and 2.73 μm.

The most probable numbers of total coliforms and E. coli had a large decrease after the filtration, reaching less than a half of the minimum value allowed for animal consumption and less than an eighth of the value allowed for recreation.

The dirty/contaminated water, after pass through the filter, had a turbidity of 0.56 ± 0.31 NTU, below the value allowed, attesting the efficiency of our filter considering the turbidity parameter.

9 Freeze-cast porous ceramic filters impregnated with silver nanoparticles[5]

9.1 Introduction

Nanomaterials are systems in which at least one dimension is 1–100 nm in length. They present particular physical and chemical properties and can be used in numerous applications. Particularly silver, in the form of nanoparticles, has shown highly efficient antimicrobial properties (Singh and Nalwa, 2011; Dash et al., 2012; Leon-Silva et al., 2016; Díaz-Soler et al., 2017).

Silver is often used as an antibacterial agent to provide a sanitary environment for the wound healing process. It is considered as one of the most frequently used antibacterial substances before the invention of antibiotics. The multiplicity of silver's bactericidal mechanisms gives it a wide range of effective applications in the inhibition of bacterial growth. The introduction of silver nanoparticles (AgNP) has allowed the scientific community to enhance antibacterial properties. Moreover, the increased surface area of nanoparticles induces an increased rate of interaction between the test subjects and ionic silver (Alexander, 2009; Nam et al., 2015; Bal et al., 2015; Dong et al., 2016; Mckevica et al., 2016; Amadio et al., 2017).

Spectrophotometric analysis is one of the most widely used analytical techniques available. The largest use of UV-Vis absorption spectroscopy lies in its application to quantitative analysis. The reasons for this stem from the ease with which most spectrophotometric measurements can be made, their sensitivity and precision, and the relatively low cost of instrument purchase and operation (Frank, 1997; Fereja, et. al, 2015).

[5] Accepted by Brazilian Journal of Chemical Engineering.

To quantify AgNP in suspension, a technique with a very low limit of detection is necessary, such as graphite furnace atomic absorption spectrometry (GFAAS). Graphite furnace is generally considered an ultratrace and microtrace analytical technique with limits of detection in the low picogram range, precision of a few percent (relative standard deviation) and a dynamic range of about three orders of magnitude. In addition to its high sensitivity, it is unique in its ability to handle microsamples including aqueous solutions, viscous liquids, slurries and even solids. GFAAS is an atomic spectroscopic technique in which a small sample is placed inside a graphite tube that is then resistively heated to accomplish sample desolvation (for liquid samples), ashing or charring (to decompose the sample and volatilize some of the matrix) and finally atomization (Holcombe, 2006).

Stoimenov and co-workers (2002) demonstrated that highly reactive metal oxide nanoparticles exhibit excellent biocidal action against Gram-positive and Gram-negative bacteria (Stoimenov et al. 2002; Sondi 2004). One way to test the bactericidal properties in the filter pellets is the Disc Diffusion Test (also known as Kirby-Bauer antibiotic testing). This is a test of the antibiotic sensitivity of bacteria. It uses antibiotic-impregnated pellets to test the extent to which bacteria are affected by those antibiotics. In this test, pellets containing antibiotic are placed on an agar plate where bacteria, Gram-positive or Gram-negative, have been placed, and the plate is left to incubate. In these tests, if an antibiotic stops the bacteria from growing or kills the bacteria, there will be an area around the pellet where the bacteria have not grown enough to be visible, it is called a zone or halo of inhibition (Mohanty 2010; Shahzada et al. 2014).

Neomycin, the antibiotic used, is an aminoglycoside antibiotic produced during fermentation of *Streptomyces fradiae* with a high antimicrobial efficacy, and broad antibacterial spectrum. It inhibits the growth of Gram-negative

and Gram-positive bacteria (Adams et al. 1996; Chang-Chien et al. 2017).

Gram-positive bacteria are bacteria that give a positive result in the Gram stain test. Gram stain differentiates bacteria by the chemical and physical properties of their cell walls by detecting peptidoglycan, which is present in the cell wall of Gram-positive bacteria. Gram-positive bacteria retain the crystal violet dye, and thus are stained violet, while the Gram-negative bacteria do not; after washing, a counterstain is added (commonly safranin or fuchsine) that will stain these Gram-negative bacteria a pink color (Holt 1994).

Enterococcus faecalis is formerly classified as part of the group D Streptococcus system – is a Gram-positive, commensal bacterium inhabiting the gastrointestinal tracts of humans and other mammals. It is usually outnumbered by strictly anaerobic bacteria (Russell et al. 2001; Ryan et al. 2004).

Escherichia coli, *E. coli*, is a Gram-negative, anaerobic, rod-shaped, coliform bacterium of the genus *Escherichia* that is commonly found in the lower intestine of warm-blooded organisms (endotherms) (Singleton 1999; Olivier et al. 2010).

In this work, an innovative approach for impregnation of porous ceramic filters, which can be used for water or wastewater treatment is proposed. Filter elements are produced by freeze casting, in which AgNP are impregnated in order to optimize reactive surface area and to enhance bactericidal effects.

9.2 Materials and methods

9.2.1 Raw materials and fabrication of filters

Porous ceramic filters samples (20 mm diameter, 15 mm thickness) of alumina (CT 3000, Almatis) and kaolinite

(Colorminas) were produced from mixtures of 30 wt% alumina, 20 wt%, kaolinite, 1.5 wt% Darvan C-N (Vanderbilt) and 38.5 wt% distilled. The slurry was homogenized, freeze-cast, dried and sintered, as described in the flow chart in Figure 1, to produce porous filter elements.

Silver nanoparticles were analyzed by Transmission Electron Microscope (TEM, JEM 1011, JEOL), with maximum acceleration voltage, 100 kV and magnification range, 800× to 600,000×. Particle size distribution was measured by direct light scattering (Zetasizer, Nanosizer – ZS, Malvern).

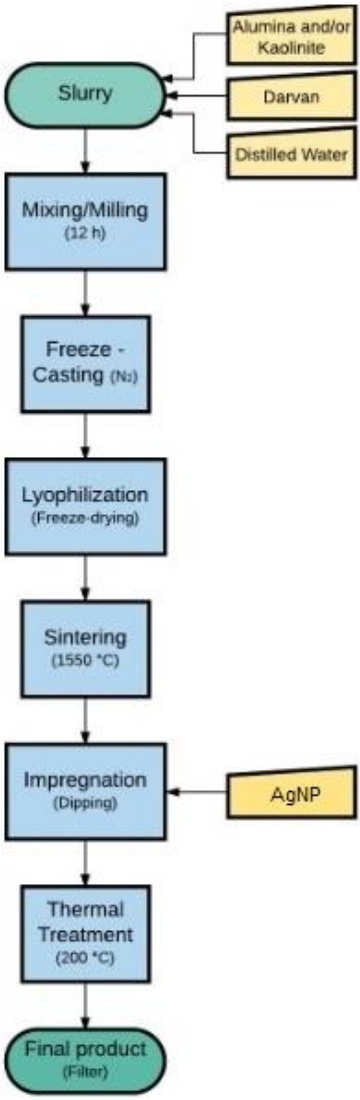

Figure 9. 1. Flowchart of processing of filter elements including impregnation of silver nanoparticles (AgNP).

9.2.2 Filter impregnation with silver nanoparticles and characterization

The samples were impregnated with an aqueous solution of silver nanoparticles (TNS, 1000 µg/L, pH 4) by dip coating in a sealed borosilicate glass beaker, during 24 h. After that, a thermal treatment was performed in a resistive furnace (J 200, Jung) at a heating rate of 5 °C/min and dwell time of 2 h at 200 °C, to fix the silver nanoparticles on the sample surface (Amadio et al., 2017).

The impregnated samples were coated with a thin layer of gold and characterized in a scanning electron microscope and energy dispersive x- ray spectroscopy (SEM/EDS, TM3030, Hitachi). EDS was used to provide rapid semi-quantitative analysis of elemental composition and to form map profiles, showing the AgNP distribution at the sample top and fracture surfaces.

To test the efficiency of impregnation, leaching tests were performed using:

- Mechanical stirring (overhead stirrer mixer**)** at 2000 rpm during 1 h (MS 1); 2 h (MS 2); 3 h, resting of 24 h and more 3 h (MS 3-24).
- Centrifugation at 3600 rpm during 15 min (CE 15) and 30 min (CE 30).
- Ultrasonic bath during 5 min (UL 5) and 15 min (UL 15).

To quantify silver in the leached water UV/VIS (UV-1800, Shimadzu), at wavelength of 405 nm (Zamiri, et. al, 2012; Vasireddy, et. al, 2012; Guzmán, et. al, 2009), and graphite furnace atomic absorption spectrometry (PinA Acle 900T, Perkin Elmer) with limit of detection of 0.35 ng/L and limit of quantitation of 1.16 ng/L were employed.

The efficiency of impregnation was estimated as a correlation of the amount of nanosilver fixed in the sample and to that leached in water, as shown in Table 1.

Table 9. 1. Concentration of silver nanoparticles and the corresponding absorbance.

Concentration (g/L)	**Abs**
0.5	0.06
1	0.07
2	0.13
3	0.16
4	0.19
5	0.16
6	0.21
7	0.28
8	0.37
9	0.45
10	0.54
11	0.60
12	0.69
13	0.76
14	0.84

To obtain the linearity, the absorbance was plotted versus the concentration (g/mL) to obtain the Beer-Lambert calibration curve (Figure 2). The equation for the calibration curve was Y = 0.0778X - 0.2473, where Y is the absorbance and X is the concentration in g/L. The value of correlation coefficient (R^2) was 0.9979. The result reveals that there is a strong linear relationship between the concentration of the test sample and the absorbance values over the concentration range 5 to 14 g/L (Figure 3). The second curve has the linearity and accuracy necessary but the range of analyte is not suitable, how is possible to observe in Figure 4, A is the color

of the sample with the analyte of the leached water and B is the color of solution which concentrations were in linearity curve. The solution A, and all the others leached waters were analyzed but their absorbance were less than 0.0045, so it is not in the range of the curve of linearity. Then it is possible affirm that the quantity of silver nanoparticle is below detection limit, so the quantity of AgNP are very small.

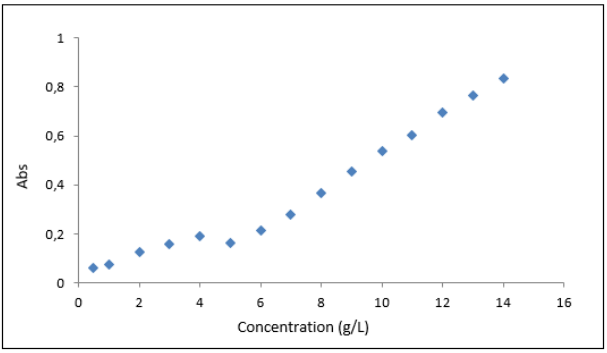

Figure 9. 2. Absorbance was plotted versus the concentration (g/mL) to obtain the Beer-Lambert calibration curve.

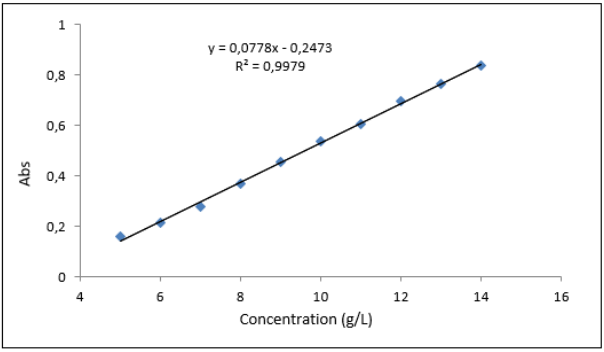

Figure 9. 3. Beer-Lambert calibration curve for AgNP in water at wavelength of 405 nm over the range of 5 to 14 g/L AgNP.

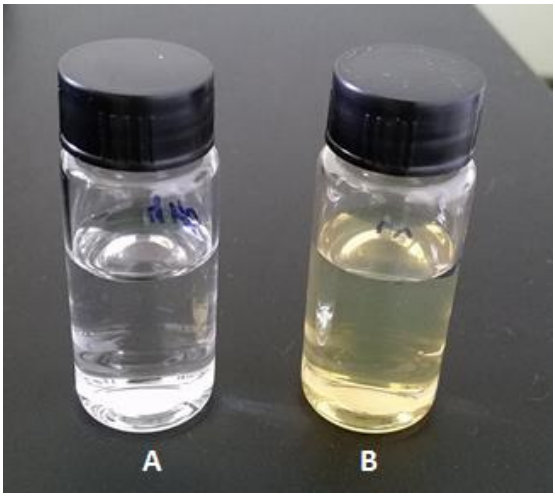

Figure 9. 4. Color of our samples, A) solution with analyte of the leached water and B) solution which concentrations were in linearity curve.

To analyze the bactericidal effects of AgNP in the filter pellets, the Disc Diffusion Test (Kirby-Bauer antibiotic testing) was used according to a standard approved by the NCCLS (National Committee for Clinical Laboratory Standards) (NCCLS, 2000). Two bacteria with distinct characteristics were chosen : *Escherichia coli* (Gram-negative) and *Enterococcus faecalis* (Gram-positive).

Pellets containing antibiotic (Neomycin) were placed on an agar plate with each bacteria type. The plate is left to incubate during 24 h at 35 °C. It was necessary to test if the antibiotic stops the bacteria from growing or kills them. The results show a halo of inhibition if silver has bactericidal effects.

9.3 Results and Discussion

9.3.1 Characterization of silver nanoparticles

The particle size distribution of AgNP was determined by DLS (Figure 5). The average size is around 46 nm in the three measures, where some agglomeration of the particles in the micrometric range can be seen.

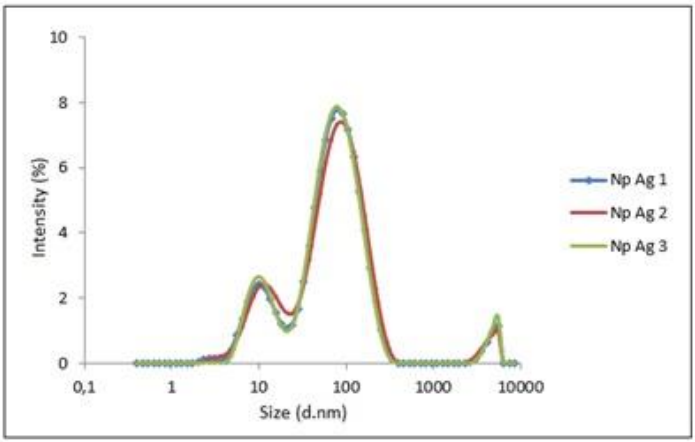

Figure 9. 5. Size distribution of AgNP analyzed by DLS.

Figure 6 shows the curve of zeta potential versus pH of silver nanoparticle concentrated (AgNP-C) and diluted (AgNP-D) suspensions. In the diluted suspension, the pH is higher (around 8), it has a broader range of zeta potential than the concentrated suspension, which has a pH 4 and a zeta potential of -29.6 mV. The isoelectric point of the suspensions can be observed at pH around 8.5. Thus, it is advisable to work with basic or acid suspensions, as far from pH 8.5 as possible, because the suspensions are more stable in these regions.

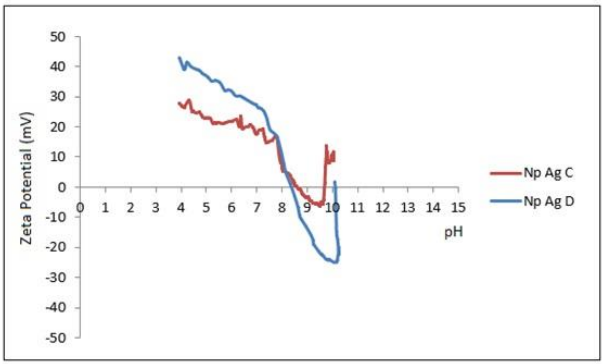

Figure 9. 6. Zeta potential versus pH, showing the isoelectric point of the silver nanoparticles concentrated and diluted suspensions.

Nanosilver particles were analyzed by TEM, as shown in the micrographs in Figure 7.

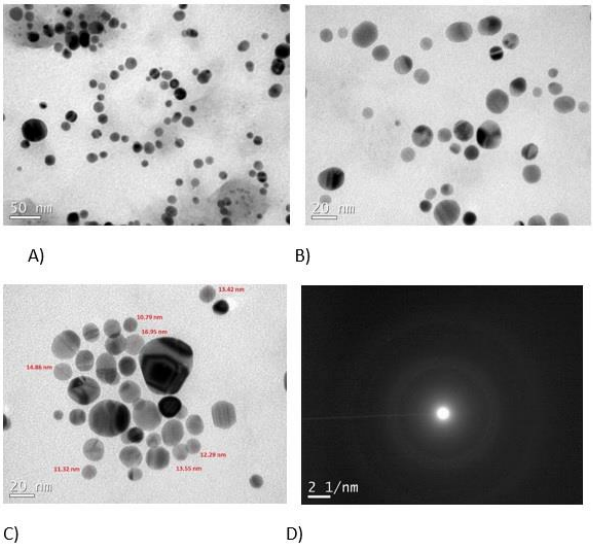

Figure 9. 7. TEM micrographs of AgNP at different magnifications and electron diffraction pattern.

Different spots or textures are seen due to the difference in crystallographic orientation or interference. Using an image processing software (ImageJ, version k 1.45), some particle considered in the same crystallographic orientation were measured, and the diameter size of these particles was between 10 nm and 16 nm, being the average around 13 nm. Figure 7D shows the distance between the transmitted point and the diffraction point, which determines the diffraction pattern.

9.3.2 Characterization of AgNP-impregnated filters

The final appearance of the AGNP-impregnated filter elements is shown in Figure 8.

Figure 9. 8. Final appearance of the sample impregnated with nano-Ag.

The impregnated samples were further characterized by a scanning electron microscope and energy dispersive x-ray spectroscopy (SEM/EDS). Figure 9 shows the micrographs of the outer and fractured surfaces of the samples. Figure 9A shows the external surface of the impregnated sample, and Figure 9B, the fractured sample. It is difficult to observe the nanoparticles in the structure due to their small size; in Figure 9C, fractured inner surface, it is possible to notice some agglomeration.

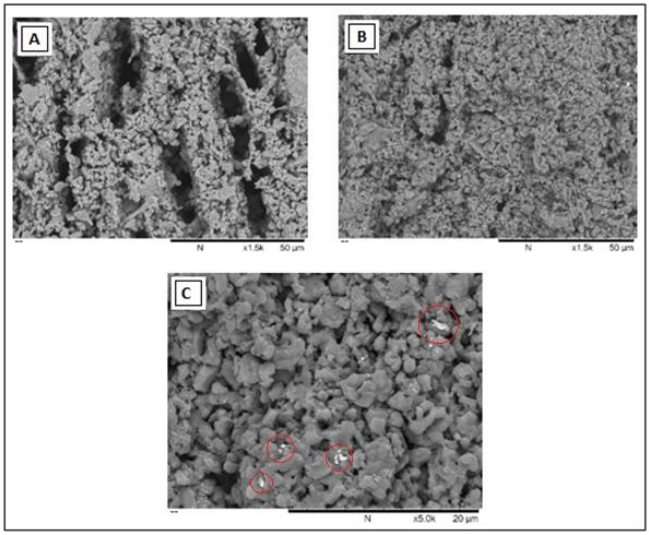

Figure 9. 9. SEM micrographs of the outer and inner (fractured) surfaces of impregnated samples: A) outer, B) inner and C) inner in detail.

To attest if this agglomeration is silver, EDS was used to provide rapid semiquantitative analysis of elemental composition. Figure 10 shows the micrograph with the spot from where EDS was performed. Firstly, a square area was chosen where a homogeneous distribution was present (Figure 11A); then, a dot corresponding to an area of agglomerated nanoparticles was also analyzed (Figure 11 B), Table 2 shows the results of elemental analysis.

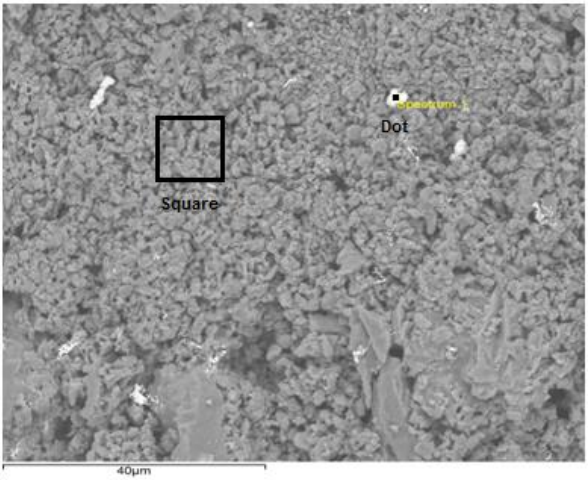

Figure 9. 10. SEM micrograph with the internal (fractured) area from where EDS was performed: square (homogeneous distribution) and dot (agglomerated particles).

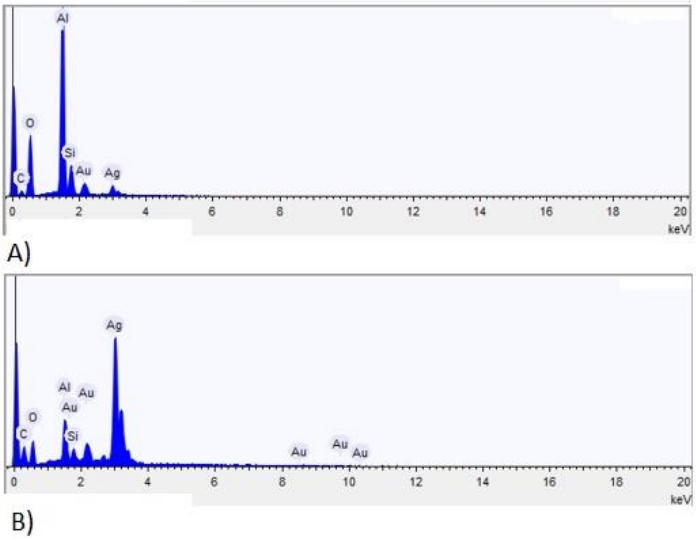

Figure 9. 11. EDS elemental analysis in: A) area of homogeneous distribution (square), B) area of nanoparticles agglomeration (dot).

Table 9. 2. EDS elemental analyze of the area of: A) homogeneous distribution (square); and B) area of nanoparticles agglomeration (dot).

Element	**A**	**B**	**A**	**B**
	Weight %		**Atomic %**	
Carbon	10.29	7.15	17.74	20.54
Oxygen	42.24	24.28	54.64	52.37
Aluminum	27.64	5.19	21.20	6.64
Silicon	6.03	1.45	4.45	1.78
Silver	5.97	53.91	1.14	17.25
Gold	7.80	8.01	0.82	1.41

EDS was used also to do build up a profile map to see the distribution of silver nanoparticles on the surface and in the samples bulk. The texture of the porous ceramic filter surfaces impregnated with silver nanoparticles is shown in Figures 12 and 13, outer and inner bulk (fractured) surfaces, respectively. It is observed that the silver nanoparticles have a homogeneous distribution along both outer and fractured surfaces of the sample and the amount of nanosilver is apparently higher in the inner part (bulk) of the fractured sample.

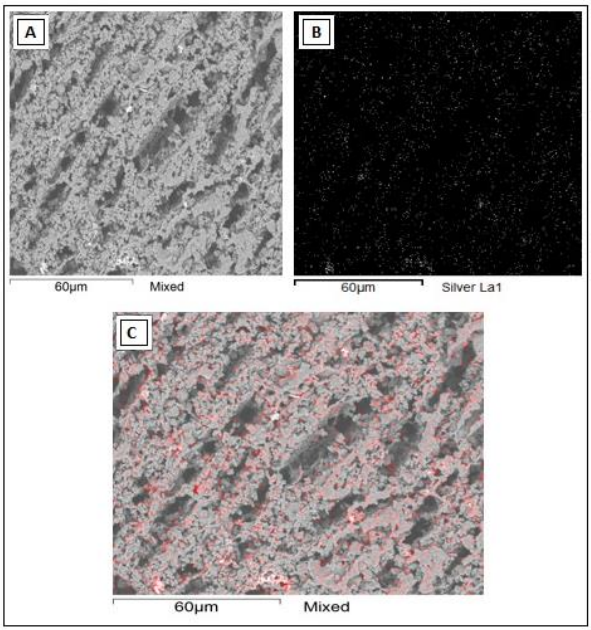

Figure 9. 12. SEM/EDS of the sample external surface: A) micrograph; B) elemental map showing the silver distribution (white dots); C) silver element distribution (red dots to increase the visibility).

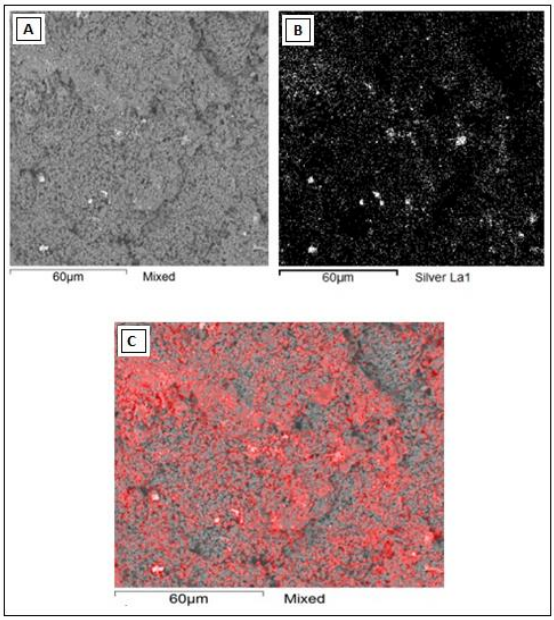

Figure 9. 13. SEM/EDS of the sample fractured bulk surface: A) micrograph; B) elemental map showing the silver distribution (white dots); C) silver element distribution (red dots to increase the visibility).

GFAAS was applied to quantify silver nanoparticles with a lower limit of detection, as seen in Table 3.

Table 9. 3. Amount of silver in the different leached samples as detected by GFAAS.

Sample	Concentration Ag (µg/L)
MS 1	0.0096
MS 2	0.0097
MS 3-24	0.0178
CE 15	0.0074
CE 30	0.0175
UL 5	0.0457
UL 15	0.0829

GFAAS was applied to quantify silver nanoparticles with a lower limit of detection, as seen in Table 3. The results confirm that there is a very small amount of silver in the leached water. The initial suspension concentration was 1000 µg/L; so that it is estimated that more than 99% of silver nanoparticles was fixed in the filter pellets.

According to CONAMA (Resolution 396/2008), the Maximum Allowed Values (MAV) for metallic silver is 100 and 50 µg/L for human consumption and recreation, respectively.

Higher levels of silver, up to 0.1 mg/L (a concentration that gives a total dose over 70 years of 10 g), could then be tolerated without risk to health (WHO, 2014). Considering those values, the quantity of silver in the leached water is well below the values allowed and it is without any risk to health.

The Disc Diffusion Test (Kirby-Bauer antibiotic testing) was performed to detect if the silver nanoparticles present inhibitory and bactericidal effects. Table 4 shows the results of this test.

Table 9. 4. Inhibition halo in the AgNP-impregnated filter elements as detected by the Disc Diffusion Test.

Bacteria	**Samples**	**Inhibition halo**
Gram-negative	Neomycin	Present
(Escherichia	Pellet without Ag	Absent
coli)	Pellet with Ag	Present
Gram-positive	Neomycin	Present
(Enterococcus	Pellet without Ag	Absent
faecalis)	Pellet with Ag	Present

In this test, the antibiotic and the nanosilver impregnated samples stopped the bacteria from growing or even killed the bacteria, because there was an area around the pellets where the bacteria have not grown enough to be visible, i.e., the halo of inhibition was present. In the pellets without nanosilver, the halo of inhibition was absent. Accordingly, the filter pellets impregnated with AgNP showed strong inhibitory and bactericidal effects.

9.4 Conclusions

Silver nanoparticles impregnation was very efficient, considering that around 99% of the initial silver was fixed in the filter elements through an easy method of impregnation, such as dipping. Graphite furnace atomic absorption spectrometry was a suitable technique to quantify the silver in the leached water.

The silver nanoparticles were homogeneously distributed along the entire structure, both at the outer and at the inner bulk fracture surface. SEM/EDS detected the presence of nanosilver throughout the samples.

The filter elements showed a strong bactericidal effect, according to the Disc Diffusion Test, which indicated the presence of a halo of inhibition in the pellets impregnated with silver nanoparticles and absence of this halo in the pellets without silver.

10 General conclusions

Composites of bentonite/nanoparticles were successfully obtained by simple impregnation procedures, which can be performed either by imbibition or by dipping, with efficiency after washing with water over 99% in the case of nano-Ag, and over 90% for Au, Pd and TiO_2 nanoparticles.

Alternatively, porous pressed filters with only kaolinite have low porosity and low compression strength; samples with only alumina have a high densification and very low porosity (including samples with rice husks). Samples with kaolinite and alumina have a good strength after contact with water, but the permeability and flow rate did not reach enough values for a water filtration, with less than 0.01 l/h. Thus, pressed alumina or kaolinite filters were not suitable for the intended application.

As an innovative approach, freeze-cast alumina with varying particle sizes were tested as water filters. Coarse alumina presented a higher solidification rate than fine alumina. The pore size for sample A50, around 3 μm, was more suitable for water purification.

The compression strength of fine alumina reached higher values, but with very low porosity. Conversely, coarse alumina presented a lower range of compressive strength, and the porosity remained higher in all the solids loads.

Considering permeability parameters k_1 and k_2 obtained in this work, the porous alumina samples achieved the desired permeability values for water filtration, regardless the particle size. According to the experimental data, coarse alumina is more suitable for this application than fine alumina.

Samples with coarse alumina and kaolinite with around 50 wt% total solids presented the highest results of compression strength, an acceptable value of

permeability/flow rate, higher values of k_1 and k_2, and suitable values of apparent porosity with a homogeneous distribution of pores. According to the experimental data, samples with coarse alumina and kaolinite are more suitable for this application.

The number of total coliforms and *E. coli* had a large decrease after filtration, reaching less than a half of the minimum value allowed for animal consumption and less than one eighth of the value allowed for recreation.

The contaminated water, after passing through the filter, had a turbidity of 0.56 ± 0.31 NTU, below the value allowed, attesting the efficiency of filter considering the turbidity parameter.

Silver nanoparticles impregnation was very efficient, with around 99% of the initial silver fixed in the filter elements, and with nanosilver homogeneously distributed along the entire structure. The silver impregnated filters showed a strong bactericidal effect.

11 References

ABNT, 1981. ABNT NBR 6923. Charcoal sampling and sample preparation, Brazil.

ABNT, 1986. ABNT NBR 8112. Charcoal: immediate analysis: test method, Brazil.

Abou El–Nour, K.M.M.A., Eftaiha, A., Al–Warthan, A., Ammar, R.A.A., 2010. Synthesis and applications of silver nanoparticles. Arab. J. Chem. 3, 135–140.

Abreu, A.S., Oliveira, M., Sá, A., Rodrigues, R.M., Cerqueira, M.A., Vicente, A.A., Machado, A.V., 2015. Antimicrobial nanostructured starch based films for packaging. Carbohydr. Polym., 129, 127–134.

Acchar, W., Segadães, A.M., 2009. Properties of sintered alumina reinforced with niobium carbide. Int. J. Refract. Met. Hard Mater. 27, 427–430.

Adams, E., Schepers, R., Roets, E., Hoogmartens, J., 1996. Determination of neomycin sulfate by liquid chromatography with pulsed electrochemical detection. J. Chromatogr. A 741, 233–240.

Ahmed, Z., 2011. Ceramic Filters, Silver, and Flow Rates. S–STEM Res. Rep.

Albuquerque, F., Santos, I., Lima, S., Cássia–Santos, M., Soledade, L., Souza, A., Martinelli, A., 2007. Experimental design applied to the optimization of ceramic pastes obtained from natural raw materials. Cerâmica 53, 300–398.

Alexander, J.W., 2009. History of the medical use of silver. Surg. Infect.(Larchmt.) 10, 289–292.

Amadio, T. M., Hotza, D., Rodrigues–Neto, J. B., Blosi, M., Costa, A. L., Dondi, M., 2017. Bentonites functionalized by impregnation with TiO_2, Ag, Pd and Au nanoparticles. Appl. Clay Sci., 146, 1–6.

Amorim, L.V., Viana, J.D., Farias, K.V., Barbosa, M.I.R., Ferreira, H.C., 2006. Estudo Comparativo entre Variedades de Argilas Bentoníticas de Boa Vista, Paraíba. Rev. Matéria 11, 30 – 40.

Anderson, C.W., 2005. Turbidity, in: National Field Manual for the Collection of Water–Quality Data. pp. 1–55.

Araki, K., Halloran, J.W., 2004. Room–temperature freeze casting for ceramics with nonaqueous sublimable vehicles in the naphthalene–camphor eutectic system. J. Am. Ceram. Soc. 87, 2014–2019.

Araki, K., Halloran, J.W., 2005. Porous ceramic bodies with interconnected pore channels by a novel freeze casting technique. J. Am. Ceram. Soc. 88, 1108–1114.

Aranberri, I., Binks, B.P., Clint, J.H., Fletcher, P.D.I., 2009. Synthesis of macroporous silica from solid–stabilised emulsion templates. J. Porous Mater. 16, 429–437.

Arshak, K., Moore, E., Lyons, G.M., Harris, J., Clifford, S., 2004. A review of gas sensors employed in electronic nose applications. Sens. Rev. 24, 181–198.

ASTM, 1997. ASTM C133–97 – Standard Test Methods for Cold Crushing Strength and Modulus of Rupture of Refractories, ASTM International, West Conshohocken, PA.

ASTM, 2014. ASTM E871–82 – Standard Test Methods for Moisture Analysis of Particulate Wood Fuels. ASTM International, West Conshohocken, PA.

ASTM, 2015. ASTM C20–00 – Standard Test Methods for Apparent Porosity, Water Absorption, Apparent Specific Gravity, and Bulk Density of Burned Refractory Brick and Shapes by Boiling Water. ASTM International, West Conshohocken, PA.

Ayari, F., Srasra, E., Trabelsi–Ayadi, M., 2005. Characterization of bentonitic clays and their use as adsorbent. Desalination, 185, 391–397.

Bahera, S., Ghanty, S., Ahmad, F., Santra, S., Banerjee, S., 2012. UV–Visible Spectrophotometric Method Development and Validation of Assay of Paracetamol Tablet Formulation. Int. J. Electrochem. Sci. 3, 3–6.

Bal, A., Çepni, F. E., Çakir, Ö, Acar, I., Güçlü, G., 2015. Synthesis and characterization of copolymeric and terpolymeric hydrogel–silver nanocomposites based on acrylic acid, acrylamide and itaconic acid: investigation of their antibacterial activity against gram–negative bacteria. Braz. J. Chem. Eng., 32, 2, 509–518.

Banhart, J., 2000. Manufacturing routes for metallic foams. Jom 52, 22–27.

Banhart, J., 2001. Manufacture, characterisation and application of cellular metals and metal foams. Prog. Mater. Sci. 6, 559–632.

Barg, S., Innocentini, M.D.M., Meloni, R. V., Chacon, W.S., Wang, H., Koch, D., Grathwohl, G., 2011. Physical and high–temperature permeation features of double–layered cellular filtering membranes prepared via freeze casting of emulsified powder suspensions. J. Memb. Sci. 383, 35–43.

Behera S, Ghanty S, Ahmad F, Santra S, B.S., 2012. UV–Visible Spectrophotometric Method Development and Validation of Assay of Department of Quality Paracetamol Tablet Formulation. J. Anal. Bioanal. Tech. 3, 6.

Bergaya, F., Theng, B.K.G., Lagaly, G. (Eds.), 2006. Handbook of Clay Science. Elsevier, Developments of Clay Science, Volume 1, Amsterdam.

Bernabé, Y., Li, M., Maineult, A., 2010. Permeability and pore connectivity: A new model based on network simulations. J. Geophys. Res. 115, 1–14.

Bicho, R.S.L., 2012. Desenvolvimento de estruturas porosas tridimensionais por Moldação por Congelamento (Freeze–Casting). Univ. Nov. Lisboa 64.

Bielefeldt, A.R., Kowalski, K., Schilling, C., Schreier, S., Kohler, A., Scott Summers, R., 2010. Removal of virus to protozoan sized particles in point–of–use ceramic water filters. Water Res. 44, 1482–1488.

Bielefeldt, A.R., Kowalski, K., Summers, R.S., 2009. Bacterial treatment effectiveness of point–of–use ceramic water filters. Water Res. 43, 3559–3565.

Binks, B.P., 2002. Particles as surfactants – Similarities and differences. Curr. Opin. Colloid Interface Sci. 7, 21-41.

Blosi, M., Albonetti, S., Dondi, M., Baldi, G., Barzanti, A, Bitossi, M., 2010. Eur. Pat., WO 2010/100107 PCT/EP2010/052534.

Blosi, M., Albonetti, S., Ortelli, S., Costa, A. L., Ortolani, L., Dondi, M., 2014. Green and easily scalable microwave synthesis of noble metal nanosols (Au, Ag, Cu, Pd) usable as catalysts. New J. Chem. 38, 1401–1409.

Blunt, M.J., 2001. Flow in porous media – Pore–network models and multiphase flow. Curr. Opin. Colloid Interface Sci. 6, 3.

Bobertag O., Feiat K., Fischer H.W., 1908. Über das Ausfrieren von Hydrosolen. Ber. Dtsch. Chem. Ges. 41, 3675–3679.

BP – British Pharmacopoeia. The Pharmaceutical Press, Her Majesty's Stationery Office, London, 1 and 2 (2009).

Brady, M.J., Lisay, C.M., Yurkovetskiy, A. V., Sawan, S.P., 2003. Persistent silver disinfectant for the environmental control of pathogenic bacteria. Am. J. Infect. Control 31, 208–214.

Brazilian Health Ministry - Portaria Ministério da Saúde, 2004. Diário Oficial da União, Brasília, 518.

Brindley, G.W., 1955. Structural Mineralogy of Clays. Clays and Clay Technology. Bulletin 169, 53.

Brown, J., Sobsey, M., Proum, S., 2007. Use of Ceramic Water Filters in Cambodia, Water and Sanitation Program.

Brown, J., Sobsey, M.D., 2010. Microbiological effectiveness of locally produced ceramic filters for drinking water treatment in Cambodia. J. Water Health 8, 1–10.

Bulut, G., Chimeddorj, M., Esenli, F., Çelik, M.S., 2009. Production of desiccants from Turkish bentonites. Appl. Clay Sci. 46, 141–147.

Cabala, G. van E., Acchar, W., 2015. Silver Nanoparticle Surface Functionalized Alumina Filters for Disinfection of Potable Water. Mater. Today Proc. 2, 321–330.

Caglar, B., 2012. Structural characterization of kaolinite–nicotinamide intercalation composite. J. Mol. Struct. 1020, 48–55.

Caglar, B., Afsin, B., Tabak, A., Eren, E., 2009. Characterization of the cation–exchanged bentonites by

XRPD, ATR, DTA/TG analyses and BET measurement. Chem. Eng. J. 149, 242–248.

Chandrasekhar, S., Satyanarayana, K.G., Pramada, P.N., Raghavan, P., Gupta, T.N., 2003. Review Processing, properties and applications of reactive silica from rice husk—an overview. J. Mater. Sci. 38, 3159–3168.

Chang–Chien, J., Yen, Y.C., Li, S.Y., Hsu, T.C., Yang, J.J., 2017. Ferulic acid–mediated protection against neomycin–induced hair cell loss in transgenic zebrafish. J. Funct. Foods 28, 157–167.

Cheng, H., Liu, Q., Yang, J., Ma, S., Frost, R.L., 2012. The thermal behavior of kaolinite intercalation complexes–A review. Thermochim. Acta. 545, 1–13.

Cho, K.H., Park, J.E., Osaka, T., Park, S.G., 2005. The study of antimicrobial activity and preservative effects of nanosilver ingredient, in: Electrochimica Acta. 956–960.

Cilla, M.S., de Melo Cartaxo, J., Menezes, R.R., de Lima Santana, L.N., de Araujo Neves, G., 2015. Production of fire clay porous structure with no aligned macro porosity from water–based slurry by freeze casting process: A new approach. Ceram. Int. 42, 9278–9282.

Clasen, T., Boisson, S., 2006. Household–based ceramic water filters for the treatment of drinking water in disaster response: and assessment of a pilot programme in the Dominican Republic. Water Practice Technol. 1 (2).

Clasen, T., Schmidt, W.P., Rabie, T., Roberts, I., Cairncross, S., 2007. Interventions to improve water quality for preventing diarrhoea: systematic review and meta–analysis. BMJ 334, 782.

Clasen, T.F., Bastable, A., 2003. Faecal contamination of drinking water during collection and household storage: The

need to extend protection to the point of use. J. Water Health 1, 109–115.

Clasen, T.F., Brown, J., Collin, S., Suntura, O., Cairncross, S., 2004. Reducing diarrhea through the use of household–based ceramic water filters: A randomized, controlled trial in rural Bolivia. Am. J. Trop. Med. Hyg. 70, 651–657.

Colombo, P., 2006. Conventional and novel processing methods for cellular ceramics. Philos. Trans. A. Math. Phys. Eng. Sci. 364, 109-124.

Colombo, P., Hellmann, J.R., 2002. Ceramic foams from preceramic polymers. Mater. Res. Innov. 6, 260–272.

CONAMA – Conselho Nacional do Meio Ambiente, 2008. RESOLUTION nº 396, Water Quality. Brazil 396, 1, 64–68.

Costa, A.L., Murphy, F., Mc Alea, E.M., Mullins, M. (Eds.) 2016. Applying Safety by Molecular Design Concepts to Nanomaterials Risk Management. Managing Risk in Nanotechnology Springer Publishing. 171–195.

CRC, 1997. The Handbook of Trace Elements. CRC Press, Boca Raton, FL.

Cruciani, G., Dalconi, M. C., Dondi, M., Meneghini, C., Matteucci, F., Barzanti, A., Lorenzi, G., Baldi, G. (2011). Temperature–resolved synchrotron X–ray diffraction of nanocrystalline titania in solvent: the effect of Cr–Sb and V–Sb doping. Journal of Nanoparticle Research, 13(2), 711–719.

Dash, A., Singh, A. P., Chaudhary, B. R., Singh, S. K., Dash, D., 2012. Effect of Silver Nanoparticles on Growth of Eukaryotic Green Algae, Nano–Micro Lett., 4, 3, 158–165.

De Marcos, A., Naït–Ali, B., Tessier–Doyen, N., Alzina, A., Pagnoux, C., Peyratout, C.S., 2014. Influence of the ice front velocity and of the composition of suspensions on thermal

properties of bentonite materials prepared using freeze–casting process. J. Eur. Ceram. Soc. 34, 4433–4441.

Deville, S., 2008. Freeze–casting of porous ceramics: A review of current achievements and issues. Adv. Eng. Mater. 10, 155–169.

Deville, S., 2010. Freeze–casting of porous biomaterials: Structure, properties and opportunities. Materials (Basel). 3, 1913–1927.

Deville, S., Saiz, E., Tomsia, A.P., 2006. Freeze casting of hydroxyapatite scaffolds for bone tissue engineering. Biomaterials 27, 5480–5489.

Deville, S., Saiz, E., Tomsia, A.P., 2007. Ice–templated porous alumina structures. Acta Mater. 55, 1965–1974.

Díaz–Soler, B. M., López–Alonso, M., Martínez–Aires, M. D., 2017. Nanosafety practices: results from a national survey at research facilities. J. Nanopart. Res., 19, 169.

Dickhout, J.M., Moreno, J., Biesheuvel, P.M., Boels, L., Lammertink, R.G.H., de Vos, W.M., 2017. Produced water treatment by membranes: A review from a colloidal perspective. J. Colloid Interface Sci. 487, 523–534.

Dickinson, E., Ettelaie, R., Kostakis, T., Murray, B.S., 2004. Factors controlling the formation and stability of air bubbles stabilized by partially hydrophobic silica nanoparticles. Langmuir 20, 8517–8525.

Dies, R.W., 2003. Development of a Ceramic Water Filter for Nepal. Massachusetts Inst. Technol. Master Thesis 170.

Dong, F., Valsami–Jones, E., Kreft, J., 2016. New, rapid method to measure dissolved silver concentration in silver nanoparticle suspensions by aggregation combined with centrifugation. J. Nanopart. Res., 18, 259.

Duncan, T. V., 2011. Applications of nanotechnology in food packaging and food safety: Barrier materials, antimicrobials and sensors. J. Colloid Interface Sci. 363, 1–24.

Edberg, S.C., Allen, M.J., Smith, D.B., 1991. Defined substrate technology method for rapid and specific simultaneous enumeration of total coliforms and Escherichia coli from water: collaborative study. J. Assoc. Off. Anal. Chem. 74, 526–9.

El Hafiane, Y., Smith, A., Chartier, T., Abouliatim, Y., Nibou, L., Bonnet, J.P., 2012. Role of dispersant and humidity on the setting of millimetric films of aluminous cement prepared by tape casting. J. Eur. Ceram. Soc. 32, 2103–2111.

European Commission, Commission recommendation of 18 October 2011 on the definition of nanomaterial, Off. J. Eur. Union 275, 38–40.

Fereja, T. H., Seifu, M. F., Mola, T. Y., 2015. UV–Visible Spectrophotometric Method Development and Quantification of Ciprofloxaciline in Tablets Dosage Form. American Journal of Pharmacy and Pharmacology. 2, 1, 1–8.

Fey, G.T.K., Chen, C.L., 2001. High–capacity carbons for lithium–ion batteries prepared from rice husk, in: J. Power Sourc. 97-98, 47–51.

Figiel, P., Rozmus, M., Smuk, B., 2011. Properties of alumina ceramics obtained by conventional and non–conventional methods for sintering ceramics. J. Achiev. Mater. Manuf. Eng. 48, 29–34.

Frank, A. S., Handbook of instrumental techniques for analytical chemistry, Prentice Hall, Inc. A Simon & Schuster Company, New Jersey (1997).

Fukasawa, T., Ando, M., Ohji, T., Kanzaki, S., 2001. Synthesis of Porous Ceramics with Complex Pore Structure by Freeze–Dry Processing. J. Am. Ceram. Soc. 84, 230–232.

Fukasawa, T., Deng, Z.–Y., Ando, M., Ohji, T., Kanzaki, S., 2002. Synthesis of Porous Silicon Nitride with Unidirectionally Aligned Channels Using Freeze–Drying Process. J. Am. Ceram. Soc. 85, 2151–2155.

Fukushima, M., Yoshizawa, Y.I., 2016. Fabrication and morphology control of highly porous mullite thermal insulators prepared by gelation freezing route. J. Eur. Ceram. Soc. 36, 2947–2953.

Fukushima, M., Zhou, Y., Yoshizawa, Y.–I., Hirao, K., 2008. Water vapor corrosion behavior of porous silicon carbide membrane support. J. Eur. Ceram. Soc. 28, 1043–1048.

Galindo, L.S.G., Neto, A.F.A., Silva, M.G.C., Vieira, M.G.A., 2013. Removal of Cadmium(II) and Lead(II) Ions from Aqueous Phase on Sodic Bentonite. Mater. Res. 16 (2), 515–527.

García, R., Pizarro, C., Lavín, A.G., Bueno, J.L., 2012. Characterization of Spanish biomass wastes for energy use. Bioresour. Technol. 103, 249–258.

Gaudillere, C., Serra, J.M., 2016. Freeze–casting: Fabrication of highlyporous and hierarchical ceramic supports for energy applications. Bol. la Soc. Esp. Ceram. y Vidr. 55, 45–54.

Gonzenbach, U.T., Studart, A.R., Tervoort, E., Gauckler, L.J., 2006. Ultrastable particle–stabilized foams. Angew. Chemie – Int. Ed. 45, 3526–3530.

Grim, R.E., 1968. Clay Mineralogy. Second Edition. McGraw–Hill Co., New York.

Gu, X., Evans, L.J., 2008. Surface complexation modelling of Cd(II), Cu(II), Ni(II), Pb(II) and Zn(II) adsorption onto kaolinite. Geochim. Cosmochim. Acta 72, 267–276.

Guzmán, M. G., Dille, J., Godet, S., 2009. Synthesis of silver nanoparticles by chemical reduction method and their antibacterial activity. International Journal of Chemical and Biomolecular Engineering 2, 3.

Guzman, Y., 2003. Certain principles of formation of porous ceramic structures, proper- ties and applications–a review. Glass Ceram. 9, 28–31.

Hashemian, S., 2010. $MnFe_2O_4$/bentonite nano composite as a novel magnetic material for adsorption of acid red 138. Afr. J. Biotechnol. 9 (50), 8667–8671.

Hassabo, A.G., Nada, A.A., Ibrahim, H.M., Abou–Zeid, N.Y., 2015. Impregnation of silver nanoparticles into polysaccharide substrates and their properties. Carbohydr. Polym. 122, 343–350.

Hassan, M.S., Abdel–Khalek, N.A., 1998. Beneficiation and applications of an Egyptian bentonite. Appl. Clay Sci. 13, 99–115.

Hautcoeur, D., Lorgouilloux, Y., Leriche, A., Gonon, M., Nait–Ali, B., Smith, D.S., Lardot, V., Cambier, F., 2016. Thermal conductivity of ceramic/metal composites from preforms produced by freeze casting. Ceram. Int. 42, 14077–14085.

He, B., Tan, J.J., Liew, K.Y., Liu, H., 2004. Synthesis of size controlled Ag nanoparticles. J. Mol. Catal. A Chem. 221, 121–126.

Holcombe, J.A., 2006. Graphite Furnace Atomic Absorption Spectrometry, in: Encyclopedia of Analytical Chemistry. pp. 807–818.

Holt, J.H., Krieg, N.R., Sneath, P.H. A., Staley, J.T., Williams, S.T., 1994. Bergey's manual of determinative bacteriology ninth edition. Eur. J. Paediatr. Neurol. 13, 560.

Holtzer, M., Bobrowski, A., Ymankowska–Kumon, S., 2011. Temperature influence on structural changes of foundry bentonites. J. Mol. Struct. 1004, 102–108.

Horozov, T.S., 2008. Foams and foam films stabilised by solid particles. Curr. Opin. Colloid Interface Sci. 13, 3, 134-140.

Horpibulsuk, S., Yangsukkaseam, N., Chinkulkijniwat, A., Du, Y.J., 2011. Compressibility and permeability of Bangkok clay compared with kaolinite and bentonite. Appl. Clay Sci. 52, 150–159.

Hu, L., Wang, C.A., Huang, Y., Sun, C., Lu, S., Hu, Z., 2010. Control of pore channel size during freeze casting of porous YSZ ceramics with unidirectionally aligned channels using different freezing temperatures. J. Eur. Ceram. Soc. 30, 3389–3396.

Hu, X., Yang, L., Li, L., Xie, D., Du, H., 2016. Freeze casting of composite system with stable fiber network and movable particles. J. Eur. Ceram. Soc. 36, 4147–4153.

Huang, H.I., Shih, H.Y., Lee, C.M., Yang, T.C., Lay, J.J., Lin, Y.E., 2008. In vitro efficacy of copper and silver ions in eradicating Pseudomonas aeruginosa, Stenotrophomonas maltophilia and Acinetobacter baumannii: Implications for on–site disinfection for hospital infection control. Water Res. 42, 73–80.

Hunger, P.M., Donius, A.E., Wegst, U.G.K., 2013. Structure–property–processing correlations in freeze–cast composite scaffolds. Acta Biomater. 9, 6338–6348.

ICH – International Conference on Harmonization of Technical Requeriments for registration of Pharmaceutical for

Human use, 1996. Q2B Validation of Analytical Procedures– Methodology. ConsensusGuidelines, ICH Harmonized Tripartite Guidelines.

ICH – International Conference on Harmonization, 2005. ICH Topic Q2 (R1) Validation of Analytical Procedures : Text and Methodology. Int. Conf. Harmon. 1994, 17.

Ikhtiyarova, G.A., Ozcan, A.S., Gok, O., Ozcan, A., 2012. Characterization of natural– and organo–bentonite by XRD, SEM, FT–IR and thermal analysis techniques and its adsorption behaviour in aqueous solutions. Clay Miner. 47, 31–44.

Innocentini, M.D.M., Faleiros, R.K., Pisani, R., Thijs, I., Luyten, J., Mullens, S., 2010. Permeability of porous gelcast scaffolds for bone tissue engineering. J. Porous Mater. 17, 615–627.

Innocentini, M.D.M., Pandolfelli, V.C., 2001. Permeability of Porous Ceramics Considering the Klinkenberg and Inertial Effects. J. Am. Ceram. Soc. 84, 941–944.

Innocentini, M.D.M., Rodrigues, V.P., Romano, C.O., Pileggi, R.G., Silva, G.M.C., Coury, J.R., 2009. Permeability optimization and performance evaluation of hot aerosol filters made using foam incorporated alumina suspension. J. Hazard. Mater. 162, 212–221

Innocentini, M.D.M., Salvini, V.R., Macedo, A., Pandolfelli, V.C., 1999. Prediction of ceramic foams permeability using Ergun's equation. Mater. Res. 2, 283–289.

Innocentini, M.D.M., Sepulveda, P., Salvini, V.R., Pandolfelli, V.C., Coury, J.R., 1998. Permeability and Structure of Cellular Ceramics: A Comparison between Two Preparation Techniques. J. Am. Ceram. Soc. 81, 3349–3352.

Jerauld, G.R., Salter, S.J., 1990. The effect of pore–structure on hysteresis in relative permeability and capillary pressure: Pore–level modeling. Transp. Porous Media 5, 103–151.

Kallman, E., Oyadenel–Craver, V.A., Smith, J.A., 2010. Ceramic Filters Impregnated with Silver Nanoparticles for Point–of–Use Water Treatment in Rural Guatemala. J. Environ. Eng. 137, 407–415.

Kenneth, J.R., Ray, C.G., 2004. Sherris Medical Microbiology (4th ed.). McGraw Hill., Vasa.

Khomutov, G.B., Gubin, S.P., 2002. Interfacial synthesis of noble metal nanoparticles. Mater. Sci. Eng. C 22, 141–146.

Kingery, W.D., Bowen, H.K., Uhlmann, D.R., 1975. Introduction to ceramics, in: Introduction to Ceramics. 3.

Klarman, M., 2009. Investigation of Ceramic Pot Filter Design Variables. J. Electrochem. Soc. 129, 78.

Koh, Y.W., Song, J.H., Lee E.J., Kim, H.E., 2006. Freezing dilute ceramic/camphene slurry for ultra–highporosity ceramics with completely interconnected pore networks. J. Am. Ceram. Soc. 89, 3089–3093.

Koli, D.K., Agnihotri, G., Purohit, R., 2014. A Review on Properties, Behaviour and Processing Methods for Al– Nano Al2O3 Composites. Procedia Mater. Sci. 6, 567–589.

Krieger, I.M., Dougherty, T.J., 1959. A mechanism for non–Newtonian flow in suspensions of rigid spheres. Trans. Soc. Rheol. 3, 137–152.

Krystosiak, P., Tomaszewski, W., Megiel, E., 2017. High–density polystyrene–grafted silver nanoparticles and their use in the preparation of nanocomposites with antibacterial properties. J. Colloid Interface Sci. 498, 9–21.

Kvı, L., Vec, R., 2006. Silver Colloid Nanoparticles : Synthesis , Characterization , and Their Antibacterial Activity. J Phys. Chem. B 110, 16248–16253.

Lantagne, D.S., Environmental, A., 2001. Investigation of the Potters for Peace Colloidal Silver Impregnated Ceramic Filter Report 1 : Intrinsic Effectiveness. 1-79.

Lantagne, D.S., Environmental, A., 2001. Investigation of the Potters for Peace Colloidal Silver Impregnated Ceramic Filter Report 2 : Field Investigations. Methods 1–121.

Lecomte–Nana, G., Mokrani, A., Tessier–Doyen, N., Boussois, K., Goure–Doubi, H., 2013. Texturation of model clay materials using tape casting and freezing. Ceram. Int. 39, 9047–9053.

Lee, S.M., Song, K.C., Lee, B.S., 2010. Antibacterial activity of silver nanoparticles prepared by a chemical reduction method. Korean J. Chem. Eng. 27, 688–692.

Leon–Silva, S., Fernandez–Luqueno, F., Lopez–Valdez, F., 2016. Silver nanoparticles (AgNP) in the environment: a review of potential risks on human and environmental health. Water Air Soil Poll., 227, 306.

Li, D., Li, M., 2012. Preparation of porous alumina ceramic with ultra–high porosity and long straight pores by freeze casting. J. Porous Mater. 19, 345–349.

Li, W.L., Lu, K., Walz, J.Y., 2012. Freeze casting of porous materials: review of critical factors in microstructure evolution. Int. Mater. Rev. 57, 37–60.

Li, Y., Chen, S.M., 2012. The electrochemical properties of acetaminophen on bare glassy carbon electrode. Int. J. Electrochem. Sci. 7, 2175–2187.

Liu, G., Button, T.W., 2013. The effect of particle size in freeze casting of porous alumina–zirconia composite. Ceram. Int. 39, 8507–8512.

Liu, R., Xu, T., Wang, C. an, 2015. A review of fabrication strategies and applications of porous ceramics prepared by freeze–casting method. Ceram. Int. 42, 2907–2925.

Lottermoser, A., 1908. Über das Ausfrieren von Hydrosolen. Ber. Dtsch. Chem. Ges. 41, 3976–3979.

Lu, H., Qu, Z., Zhou, Y., 1998. Preparation and mechanical properties of dense polycrystalline hydroxyapatite through freeze–drying. J. Mater. Sci. Mater. Med. 9, 583–587.

Lummus, J.L., Azar, J.J., 1986. Drilling Fluids Optimization a Practical Field Approach, Penn–Well Publishing Company, Tulsa.

Luz, A.B., Lins, F.A.F., 2008. Rochas & Minerais Industriais: Usos E Especificações. Second Edition. CETEM, Rio de Janeiro.

Lv, Y., Liu, H., Wang, Z., Liu, S., Hao, L., Sang, Y., Liu, D., Wang, J., Boughton, R.I., 2009. Silver nanoparticle–decorated porous ceramic composite for water treatment. J. Memb. Sci. 331, 50–56.

Mackevica, A., Olsson, M. E., Hansen, S. F., 2016. Silver nanoparticle release from commercially available plastic food containers into food simulants. J. Nanopart. Res., 18, 5.

Magriotis, Z.M., Leal, P.V.B., Sales, P.F., Papini, R.M., Viana, P.R.M., 2010. Adsorption of etheramine on kaolinite: A cheap alternative for the treatment of mining effluents. J. Hazard. Mater. 184, 465–471.

Maneerung, T., Tokura, S., Rujiravanit, R., 2008. Impregnation of silver nanoparticles into bacterial cellulose

for antimicrobial wound dressing. Carbohydr. Polym. 72, 43–51.

Mann, A.G., Tam, C.C., Higgins, C.D., Rodrigues, L.C., 2007. The association between drinking water turbidity and gastrointestinal illness: a systematic review. BMC Public Health 7, 256.

Mariotto, C.L., 2005. Areias Aglomeradas com Argilas. Tecnologia Básica.

Mattea, F., Vedelago, J., Malano, F., Gomez, C., Strumia, M.C., Valente, M., 2017. Silver nanoparticles in X–ray biomedical applications. Radiat. Phys. Chem. 130, 442–450.

Maxwell W., Gurnick A.R., Francisco A.C., 1954. Preliminary investigation of the freeze–casting method for forming refractory powders. NACA Research Memorandum, Lewis Flight Propulsion Laboratory.

Medvedovski, E., 2006. Alumina–mullite ceramics for structural applications. Ceram. Int. 32, 369–375.

Mihelcic, J.R., Fry, L.M., Myre, E.A., Phillips, L.D., Barkdoll, B.D., 2009. Field Guide to Environmental Engineering for Development Workers. ASCE, Reston, VA, USA, 550.

Mikelonis, A.M., Lawler, D.F., Passalacqua, P., 2016. Multilevel modeling of retention and disinfection efficacy of silver nanoparticles on ceramic water filters. Sci. Total Environ. 566–567, 368–377.

Miller, S.M., Xiao, X., Faber, K.T., 2015. Freeze–cast alumina pore networks: Effects of freezing conditions and dispersion medium. J. Eur. Ceram. Soc. 35, 3595–3605.

Mohanty, A., 2010. Physiochemical and antimicrobial study of polyherbal. Pharmacie globale., 4, 4, 1–3.

Mokhena, T.C., Luyt, A.S., 2017. Electrospun alginate nanofibres impregnated with silver nanoparticles: Preparation, morphology and antibacterial properties. Carbohydr. Polym. 165, 304–312.

Moreira, E.A., Innocentini, M.D.M., Coury, J.R., 2004. Permeability of ceramic foams to compressible and incompressible flow. J. Eur. Ceram. Soc. 24, 3209–3218.

Moreno, R., 2005. Reología de suspensiones cerâmicas.
Madrid: Consejo Superior de Investigaciones Científicas.
CSIC, Madrid, 1-328.

Moritz, T., Richter, H.J., 2006. Ceramic bodies with complex geometries and ceramic shells by freeze casting using Ice as mold material. J. Am. Ceram. Soc. 89, 2394–2398.

Morones, J.R., Elechiguerra, J.L., Camacho, A., Holt, K., Kouri, J.B., Ramírez, J.T., Yacaman, M.J., 2005. The bactericidal effect of silver nanoparticles. Nanotechnology 16, 2346–2353.

Motshekga, S.C., Ray, S.S., Onyango, M.S, Momba, M.N.B., 2015. Preparation and antibacterial activity of chitosan–based nanocomposites containing bentonite–supported silver and zinc oxide nanoparticles for water disinfection. Appl. Clay Sci. 114, 330–339.

Murray, B.S., 2007. Stabilization of bubbles and foams. Curr. Opin. Colloid Interface Sci. 12, 4-5, 232-241.

Mwabi, J.K., Adeyemo, F.E., Mahlangu, T.O., Mamba, B.B., Brouckaert, B.M., Swartz, C.D., Offringa, G., Mpenyana–Monyatsi, L., Momba, M.N.B., 2011. Household water treatment systems: A solution to the production of safe drinking water by the low–income communities of Southern Africa. Phys. Chem. Earth, Parts A/B/C 36, 1120–1128.

Nam, G., Rangasamy, S., Purushothaman, B., Song, J.M., 2015. The Application of Bactericidal Silver Nanoparticles in Wound Treatment. Nanomater. Nanotechnol. 1, 5, 23.

NCCLS – National Committee for Clinical Laboratory Standards, 2000. Performance standards for antimicrobial disk susceptibility tests, 7rd ed. Approved standard M2–A7. National Committee for Clinical Laboratory Standards, Wayne, Pa.

Neaman, A., Pelletier, M., Villieras, F., 2003. The effects of exchanged cation, compression, heating and hydration on textural properties of bulk bentonite and its corresponding purified montmorillonite. Appl. Clay Sci. 22, 153–168.

Neirinck, B., Fransaer, J., Van der Biest, O., Vleugels, J., 2009. A novel route to produce porous ceramics. J. Eur. Ceram. Soc. 29, 833–836.

Occelli, M.L., Tindwa, R.M., 1983. Physicochemical properties of montmorillonite interlayered with catonic oxyaluminum pillars. Clays Clay Miner. 39, 22–28.

Oliveira, M.M., Ugarte, D., Zanchet, D., Zarbin, A.J.G., 2005. Influence of synthetic parameters on the size, structure, and stability of dodecanethiol–stabilized silver nanoparticles. J. Colloid Interface Sci. 292, 429–435.

Olivier, T., Skurnik, D., Picard, B., Denamur, E., 2010. The population genetics of commensal Escherichia coli. Nat. Rev. Microbiol., 8, 3 207–217.

Ortelli, S., Costa, A.L., 2016. Nanoencapsulation techniques as a ‘‘safer by (molecular) design’’ tool. Nano–Struct. Nano–Objects. doi: 10.1016/j.nanoso.2016.03.006, in press.

Oyanedel–Craver, V.A., Smith, J.A., 2008. Sustainable colloidal–silver–impregnated ceramic filter for point–of–use water treatment. Environ. Sci. Technol. 42, 927–933.

Paiva, L.B., Morales, A.R., Díaz, F.R.V., 2008. Organoclays: Properties, preparation and applications. Appl. Clay Sci. 42, 8–24.

Parolo, M.E., Pettinari, G.R., Musso, T.B., Sánchez–Izquierdo, M.P., Fernández, L.G., 2014. Characterization of organo–modified bentonite sorbents: The effect of modification conditions on adsorption performance. Appl. Surf. Sci. 320, 356–363.

Patnaik, P., 2002. Handbook of Inorganic Chemicals. McGraw–Hill.

Patterson, A.L., 1939. The Scherrer Formula for X–Ray Particle Size Determination. Phys. Rev. 56 (10), 978–982.

Pereira, S., Silva, D., 2001. Caulim. Balanço Miner. Bras. 1–13.

Pokhrel, A., Park, J.G., Jho, G.H., Kim, J.Y., Kim, I.J., 2011. Controlling the porosity of particle stabilized Al_2O_3 based ceramics. J. Korean Ceram. Soc. 48, 600–603.

Prabhu, S., Poulose, E.K., 2012. Silver nanoparticles: mechanism of antimicrobial action, synthesis, medical applications, and toxicity effects. Int. Nano Lett. 2, 32.

Praus, P., Turicová, M., Karlíková, M., Kvítek, L., Dvorský, R., 2013. Nanocomposite of montmorillonite and silver nanoparticles: Characterization and application in catalytic reduction of 4–nitrophenol. Mater. Chem. Phys. 140, 493–498.

Princen, H.M., Kiss, A.D., 1989. Rheology of foams and highly concentrated emulsions. IV. An experimental study of the shear viscosity and yield stress of concentrated emulsions. J. Colloid Interface Sci. 128, 176–187.

Rai, M., Yadav, A., Gade, A., 2009. Silver nanoparticles as a new generation of antimicrobials. Biotechnol. Adv. 27, 1, 76–83.

Ramsden, W., 1903. Separation of solids in the surface–layers of solutions and suspensions. Proc. R. Soc. Lond. 72, 477-486, 156-164.

Rao, C.N.R., Müller, A., Cheetham, A.K. (Eds.), 2007. Nanomaterials Chemistry. Wiley–VCH, Recent Developments and New Directions, Weinheim.

Reed, J.S., 1995. Principles of Ceramics Processing, vol. 2. Wiley–Interscience, Tokyo.

Riedel, R., Chen, I–W., 2010. Ceramics Science and Technology, vol. 2. Materials and Properties, Wiley–VCH.

Rubim, A.M., Laporta, L.V., Bandeira, J., 2012. Validação de metodologia por UV/VIS.

Russell, J.B., Jarvis, G.N., 2001. Practical mechanisms for interrupting the oral–fecal lifecycle of Escherichia coli. J. Mol. Microbiol. Biotechnol. 3, 265–272.

Ryan, K. J., Ray, C. G., 2004. Sherris Medical Microbiology, 4rd ed. McGraw Hill pp 294–95.

Saeb, A.T.M., Alshammari, A.S., Al–Brahim, H., Al–Rubeaan, K.A., 2014. Production of silver nanoparticles with strong and stable antimicrobial activity against highly pathogenic and multidrug resistant bacteria. Sci. World J. 2014, 1-9.

Salvinelli, C., Elmore, A.C., Reidmeyer, M.R., Drake, K.D., Ahmad, K.I., 2016. Characterization of the relationship between ceramic pot filter water production and turbidity in source water. Water Res. 104, 28–33.

Sarkar, N., Park, J.G., Mazumder, S., Pokhrel, A., Aneziris, C.G., Kim, I.J., 2015. Al_2TiO_5–mullite porous ceramics from particle stabilized wet foam. Ceram. Int. 41, 6306–6311.

Sarkar, N., Park, J.G., Mazumder, S., Pokhrel, A., Aneziris, C.G., Kim, I.J., 2015. Effect of amphiphile chain length on wet foam stability of porous ceramics. Ceram. Int. 41, 4021–4027.

Scheffler, M., Colombo, P., 2006. Cellular Ceramics: Structure, Manufacturing, Properties and Applications, Wiley–VCH.

Sepulveda, P., 1997. Gelcasting foams for porous ceramics. Am. Ceram. Soc. Bull. 76, 61–65.

Settle, F. a., 1997. Handbook of Instrumental Techniques for Analytical Chemistry. Prentice Hall PTR.

Seuba, J., Deville, S., Guizard, C., Stevenson, A.J., 2016. The effect of wall thickness distribution on mechanical reliability and strength in unidirectional porous ceramics. Sci. Technol. Adv. Mater. 17, 128–135.

Shahzada, H., Naz, S., Shireen, F., Shehzada, S., Ziaullah, 2014. Epidmological and sensitivity patterns of specified antibiotics inimical to pathogens causing urinary tract infections (UTIs). Int. J. Adv. Res., 2, 3, 586–589.

Sharma, V.K., Yngard, R.A., Lin, Y., 2009. Silver nanoparticles: Green synthesis and their antimicrobial activities. Adv. Colloid Interface Sci. 145, 1–2, 83–96.

Shi, G., Wu, Z., Jiang, C., Peng, S., Yan, J., Wang, Z., 2015. Porous alumina ceramics produced by physical vapor deposition assisted freeze–casting method. Mater. Lett. 161, 580–582.

Silva, a R. V, Ferreira, H.C., 2008. Argilas bentoníticas: conceitos, estruturas, propriedades, usos industriais, reservas, produção e produtores/fornecedores nacionais e internacionais. Rev. Eletrônica Mater. Process. 2, 26–35.

Simão, L., Caldato, R.F., Innocentini, M.D.M., Montedo, O.R.K., 2015. Permeability of porous ceramic based on calcium carbonate as pore generating agent. Ceram. Int. 41, 4782–4788.

Simão, L., Montedo, O.R.K., Paula, M.M.D.S., Silva, L. Da, Caldato, R.F., Innocentini, M.D.M., 2013. Structural and fluid dynamic characterization of calcium carbonate–based porous ceramics. Mater. Res. 16, 1439–1448.

Simonis, J.J., Basson, A.K., 2011. Evaluation of a low–cost ceramic micro–porous filter for elimination of common disease microorganisms. Phys. Chem. Earth 36, 1129–1134.

Simonis, J.J., Basson, A.K., 2012. Manufacturing a low–cost ceramic water filter and filter system for the elimination of common pathogenic bacteria. Phys. Chem. Earth 50–52, 269–276.

Singh, R., Nalwa, H. S., 2011. Medical applications of nanoparticles in biological imaging, cell labeling, antimicrobial agents, and anticancer nanodrugs. J. Biomed. Nanothecnol., 7, 489–503.

Singh, S., Bharti, A., Meena, V.K., 2014. Structural, thermal, zeta potential and electrical properties of disaccharide reduced silver nanoparticles. J. Mater. Sci. Mater. Electron. 25, 3747–3752.

Singleton, P., 1999. Bacteria in Biology, Biotechnology and Medicine. Wiley. pp. 5th ed., 444–454.

Snijkers, F., de Wilde, A., Mullens, S., Luyten, J., 2004. Aqueous tape casting of yttria stabilised zirconia using natural product binder. J. Eur. Ceram. Soc. 24, 1107–1110.

Sofie, S.W., Dogan, F., 2001. Freeze Casting of Aqueous Alumina Slurries with Glycerol. J. Am. Ceram. Soc. 84, 1459–1464.

Sondi, I., Salopek–Sondi, B., 2004. Silver nanoparticles as antimicrobial agent: A case study on E. coli as a model for Gram–negative bacteria. J. Colloid Interface Sci. 275, 177–182.

Soon, Y.M., Shin, K.H., Koh, Y.H., Lee, J.H., Kim, H.E., 2009. Compressive strength and processing of camphene–based freeze cast calcium phosphate scaffolds with aligned pores. Mater. Lett. 63, 1548–1550.

Soriano, G.B., da Silva Oliveira, R., Camilo, F.F., Caseli, L., 2017. Interaction of non–aqueous dispersions of silver nanoparticles with cellular membrane models. J. Colloid Interface Sci. 496, 111–117.

Souza, D.F., Nunes, E.H.M., Pimenta, D.S., Vasconcelos, D.C.L., Nascimento, J.F., Grava, W., Houmard, M., Vasconcelos, W.L., 2014. Synthesis and structural evaluation of freeze–cast porous alumina. Mater. Charact. 96, 183–195.

Stoimenov, P. K., Klinger, R. L., Marchin, G. L., Klabunde, K.J., 2002. Metal oxide nanoparticles as bactericidal agents. Langmuir. 18, 6679–6686.

Studart, A.R., Gonzenbach, U.T., Tervoort, E., Gauckler, L.J., 2006. Processing routes to macroporous ceramics: A review. J. Am. Ceram. Soc. 89, 6, 1771–1789.

Subramaniam, A.B., Mejean, C., Abkarian, M., Stone, H.A., 2006. Microstructure, morphology, and lifetime of armored bubbles exposed to surfactants. Langmuir 22, 5986–5990.

Taglieri, G., Mondelli, C., Daniele, V., Pusceddu, E., Trapananti, A., 2013. Synthesis and X–Ray Diffraction Analyses of Calcium Hydroxide Nanoparticles in Aqueous Suspension. Adv. Mater. Phys. Chem. 3, 108–112.

Tenaillon, O., Skurnik, D., Picard, B., Denamur, E., 2010. The population genetics of commensal Escherichia coli. Nat.Rev.Microbiol. 8, 207–217.

U.S. EPA – United States Environmental Protection Agency, 1999. Silver State. EPA, Integrated Risk Information System, IRIS.

Vakifahmetoglu, C., Zeydanli, D., Innocentini, M.D.M., Ribeiro, F.D.S., Lasso, P.R.O., Soraru, G.D., 2017. Gradient–Hierarchic–Aligned Porosity SiOC Ceramics. Sci. Rep. 7, 41049.

Van der Laan, H., van Halem, D., Smeets, P.W.M.H., Soppe, A.I.A., Kroesbergen, J., Wubbels, G., Nederstigt, J., Gensburger, I., Heijman, S.G.J., 2014. Bacteria and virus removal effectiveness of ceramic pot filters with different silver applications in a long term experiment. Water Res. 51, 47–54.

Van Dong, P., Ha, C., Binh, L., Kasbohm, J., 2012. Chemical synthesis and antibacterial activity of novel–shaped silver nanoparticles. Int. Nano Lett. 2, 9

Van Halem, D., Heijman, S.G.J., Soppe, A.I.A., Van Dijk, J.C., Amy, G.L., 2007. Ceramic silver–impregnated pot filters for household drinking water treatment in developing countries: Material characterization and performance study. Water Sci. Technol. Water Supply 7, 9–17.

Van Halem, D., Van der Laan, H., Heijman, S.G.J., van Dijk, J.C., Amy, G.L., 2009. Assessing the sustainability of the silver–impregnated ceramic pot filter for low–cost household drinking water treatment. Phys. Chem. Earth 34, 36–42.

Vasireddy, R., Paul, R., Mitra, A. K., 2012. Green Synthesis of Silver Nanoparticles and the Study of Optical Properties. Nanomaterials and Nanotechnology, 2, 8, 1-6.

Venkatesan, J., Lee, J.Y., Kang, D.S., Anil, S., Kim, S.K., Shim, M.S., Kim, D.G., 2017. Antimicrobial and anticancer activities of porous chitosan–alginate biosynthesized silver nanoparticles. Int. J. Biol. Macromol. 98, 515–525.

Volkmann, E., 2015. Effects of High–Temperature Exposure on the Mechanical Performance of Polymer–Derived Oxide–Based Ceramic Matrix Composites 56–58, 1-201.

Wang, Z., Feng, P., Wang, X., Geng, P., Akhtar, F., Zhang, H., 2016. Fabrication and properties of freeze–cast mullite foams derived from coal–series kaolin. Ceram. Int. 42, 12414–12421.

Wegst, U.G., Schecter, M., Donius, A.E., Hunger, P.M., 2010. Biomaterials by freeze casting. Philos Trans A Math Phys Eng Sci 368, 2099–2121.

Wegst, U.G.K., Bai, H., Saiz, E., Tomsia, A.P., Ritchie, R.O., Ortiz, C., Boyce, M., 2014. Bioinspired structural materials. Nat. Mater. 14, 23–36.

WHO – World Health Organization, 1996. Silver in Drinking–water. Guidel. Drink. Qual. 2, 1–9.

WHO – World Health Organization, 1997. Guidelines for drinking-water quality. Surveillance and control of community supplies. 3. Geneva.

WHO – World Health Organization, 2006. Joint Monitoring Programme for Water Supply and Sanitation. UNICEF.

WHO – World Health Organization, 2008. Turbidity measurement: the importance of measuring turbidity: Fact sheet 2.33. Geneva.

WHO - World Health Organization, 2011. Guidelines for Drinking–water Quality. 1. Geneva.

WHO – World Health Organization, 2014. Silver in Drinking–water Background document for development of WHO. Guidelines for Drinking–water Quality, WHO, Geneva.

WHO – World Health Organization, 2017a, Guidelines for drinking-water quality, fourth edition incorporating the first addendum. Geneva.

WHO – World Health Organization, 2017b, Water quality and health - Review of turbidity: Information for regulators and water suppliers. 1-10.

Willenbacher, M., Georgieva, K., 2013. Rheology of Disperse Systems. Product Design and Engineering: Formulation of Gels and Pastes, Wiley–VCH.

Wood, S., Harris, A.T., 2008. Porous burners for lean–burn applications. Prog. Energy Combust. Sci. 5, 667–684.

Wu, S.C., Hsu, H.C., Hsiao, S.H., Ho, W.F., 2009. Preparation of porous 45S5 Bioglass®–derived glass–ceramic scaffolds by using rice husk as a porogen additive. J. Mater. Sci. Mater. Med. 20, 1229–1236.

Yadav, A.K., Gautam, C., Singh, P., 2012. Crystallization Kinematics and Dielectric Behavior of (Ba,Sr)TiO3 Borosilicate Glass Ceramics, New J. Glass Ceram. 2, 126–131.

Yakub, I., Du, J., Soboyejo, W.O., 2012. Mechanical properties, modeling and design of porous clay ceramics. Mater. Sci. Eng. A 558, 21–29.

Yeo, S.Y., Lee, H.J., Jeong, S.H., 2003. Preparation of nanocomposite fibers for permanent antibacterial effect, in: J. Mat. Sci. 2143–2147.

Yoon, B.–H., Choi, W.–Y., Kim, H.–E., Kim, J.–H., Koh, Y.–H., 2008. Aligned porous alumina ceramics with high compressive strengths for bone tissue engineering. Scr. Mater. 58, 537–540.

Yoon, B.H., Koh, Y.H., Park, C.S., Kim, H.E., 2007. Generation of large pore channels for bone tissue engineering using camphene–based freeze casting. J. Am. Ceram. Soc. 90, 1744–1752.

Youmoue, M., Fongang, R.T.T., Sofack, J.C., Kamseu, E., Melo, U.C., Tonle, I.K., Leonelli, C., Rossignol, S., 2017. Design of ceramic fi lters using Clay/Sawdust composites : E ff ect of pore network on the hydraulic permeability. Ceram. Int. 43, 4496–4507.

Yuping, Z., Dongliang, J., Greil, P., 2000. Tape casting of aqueous Al2O3 slurries. J. Eur. Ceram. Soc. 20, 1691–1697.

Zamiri, R., Azmi, B.Z., Ahangar, H.A., Zamiri, G., Husin, M.S., Wahab, Z.A., 2012. Preparation and characterization of silver nanoparticles in natural polymers using laser ablation. Bull. Mater. Sci. 35, 727–731.

Zamparas, M., Gianni, A., Stathi, P., Deligiannakis, Y., Zacharias, I., 2012. Removal of phosphate from natural waters using innovative modified bentonites. Appl. Clay Sci. 62–63, 101–106.

Zeng, F., Hou, C., Wu, S., Liu, X., Tong, Z., Yu, S., 2007. Silver nanoparticles directly formed on natural macroporous

matrix and their anti–microbial activities. Nanotechnology 18, 55605.

Zhang, H., Oyanedel–Craver, V., 2013. Comparison of the bacterial removal performance of silver nanoparticles and a polymer based quaternary amine functionalized silsesquioxane coated point–of–use ceramic water filters. J. Hazard. Mater. 260, 272–277.

Zhang, Y., Chen, Y., Yan, M., Chen, F., 2015. New formulas for the tortuosity factor of electrochemically conducting channels. Electrochem. Commun. 60, 52–55.

Zhang, Y., Hu, L., Han, J., Jiang, Z., 2010. Freeze casting of aqueous alumina slurries with glycerol for porous ceramics. Ceram. Int. 36, 617–621.

Zhao, Y., Wang, Z.Q., Zhao, X., Li, W., Liu, S.X., 2013. Antibacterial action of silver–doped activated carbon prepared by vacuum impregnation. Appl. Surf. Sci. 266, 67–72.

Zou, J., Zhang, Y., Li, R., 2011. Effect of suspension state on the pore structure of freeze–cast ceramics. Int. J. Appl. Ceram. Technol. 8, 482–489.